DISSERTATION

Mutierte Phosphodiesterase 3A schützt vor Hypertonie-induzierten Endorganschäden

Mutant phosphodiesterase 3A protects from hypertension-induced end-organ damage

zur Erlangung des akademischen Grades
Doctor of Philosophy (PhD)

vorgelegt der Medizinischen Fakultät
Charité – Universitätsmedizin Berlin

von

Anastasiia Sholokh

Erstbetreuung: PD Dr. Enno Klussmann

Datum der Promotion: 29.11.2024

Table of contents

List of tables iii
List of figures iv
List of abbreviations v
Abstract 1
Zusammenfassung 2
1 Introduction 4
1.1 Hypertension and its complications 4
1.1.1 The definition of hypertension 4
1.1.2 Hypertension is a major risk factor for heart failure and CKD 4
1.1.3 Treatment options for hypertension and its complications are limited 5
1.2 Hypertension with brachydactyly type E (HTNB) 6
1.2.1 Features and cause of HTNB 6
1.2.2 Hypertension without end-organ damage in HTNB patients 7
1.3 Aim of the thesis 8
2 Methods 9
2.1 Evaluation of the patient data 9
2.2 HTNB rat models 9
2.3 Animal handling 9
2.4 Histological staining and immunofluorescence microscopy 10
2.5 Western blotting 11
2.6 Reverse transcription quantitative real-time polymerase chain reaction (RT-qPCR) 12
2.7 RNA sequencing 13
2.8 Enzyme-linked Immunosorbent Assay (ELISA) 13
2.9 Cell transfection and immunoprecipitation 14
2.10 Other methods 14
2.11 Statistical analysis 15
3 Results 16
3.1 Clinical examination of HTNB patient: almost no heart and kidney damage 16
3.2 HTNB rats are protected from hypertension-induced kidney damage 17
3.2.1 HTNB affected kidney vessels but not kidney morphology 17

3.2.2 Mutant PDE3A is not associated with inflammation and fibrosis in rat kidneys upon HTNB....22
3.2.3 AREG is downregulated in kidneys of HTNB rats....25
3.3 HTNB rats are protected from hypertension-induced cardiac damage....30
3.3.1 HTNB affected cardiac vessels but not heart morphology....30
3.3.2 Isoproterenol induced cardiac damage in HTNB rats to the same degree as in WT....32
3.3.3 SERCA2A-SER663 is involved in PDE3A1-SERCA2A interaction....36
4 Discussion....38
4.1 Renoprotection mediated by mutant PDE3A....38
4.2 Potential role of AREG in PDE3A-mediated renoprotection....38
4.3 Potential mechanisms for downregulation of mutant PDE3A....39
4.4 Local effects of mutant PDE3A....40
4.5 Cardioprotection mediated by mutant PDE3A....41
4.6 Further directions for the study and clinical implication....42
5 Conclusions....44
Reference list....45
Statutory Declaration....51
Declaration of your my contribution to the publications....52
Copies of the publications....53
Curriculum Vitae....101
Publications....103
Acknowledgments....106

List of tables

Table 2.1. Protocols for the bright-field and immunofluorescence staining.....10

List of figures

Figure 1.1. *PDE3A* gene, protein isoforms, and the location of HNTB-causing *PDE3A* mutations 7
Figure 3.1. Blood and urine parameters of an HNTB patient are not changed 17
Figure 3.2. Only renal resistance arteries are affected in HTNB rat models 18
Figure 3.3. Kidneys from HTNB rats do not show obvious signs of hypertension-induced damage 20
Figure 3.4. Mutant PDE3A is downregulated in the kidney, but the cAMP and cGMP levels are not affected. 21
Figure 3.5. HTNB is not associated with inflammation in kidneys of rat models 23
Figure 3.6. HTNB is not associated with tissue fibrosis in kidneys of rat models 24
Figure 3.7. RNA sequencing of kidneys from WT, PDE3A-Δ3aa, and Func. DEL rats. . 26
Figure 3.8. The expression levels of cAMP signalling pathway proteins are not affected in HTNB rats 27
Figure 3.9. Downregulation of AREG expression is associated with HTNB in PDE3A-Δ3aa rats. 28
Figure 3.10. The phosphorylation levels of downstream kinases in the EGFR signalling pathway are unchanged in HTNB rats.. 29
Figure 3.11. Hearts from HTNB rats do not show obvious signs of hypertension-induced damage 31
Figure 3.12. RNA sequencing of hearts from untreated WT and PDE3A-Δ3aa rats 32
Figure 3.13. Isoproterenol-induced cardiac damage in HTNB animals is similar to that of WT. 34
Figure 3.14. RNA sequencing of hearts from WT, PDE3A-Δ3aa rats, and Func DEL rats treated with NaCl or Isoproterenol. 35
Figure 3.15. SERCA2A-Ser663 is involved in the interaction between SERCA2A and PDE3A1. 37

List of abbreviations

aa	amino acid
ACTA2	smooth muscle actin alpha 2
AKAP18δ	A-kinase anchoring protein 18δ
ANOVA	analysis of variance
AREG	amphiregulin
cAMP	cyclic adenosine-3',5'-monophosphate
cGMP	cyclic guanosine-3',5'-monophosphate
CKD	chronic kidney disease
CREB	cAMP response element-binding protein
DEL	deletion
EGF	epidermal growth factor
eGFR	estimated glomerular filtration rate
EGFR	epidermal growth factor receptor
ELISA	enzyme-linked immunosorbent assay
GO	gene ontology
HEK293	Human embryonic kidney 293
HRP	horseradish peroxidase
HTNB	hypertension with brachydactyly type E
ICER	inducible cAMP early repressor
Iso	isoproterenol
MDC	Max Delbrück Center for Molecular Medicine
PBS	phosphate-buffered saline
PDE	phosphodiesterase
PDE3A	cGMP-inhibited cAMP phosphodiesterase 3A
PKA	protein kinase A
PLN	phospholamban
RAAS	renin-angiotensin-aldosteron-system
RT-qPCR	polymerase chain reaction
SERCA2A	sarcoplasmic reticulum calcium ATPase 2A
SEM	standard error mean
SR	sarcoplasmic reticulum

TBS	Tris-buffered saline
VSMCs	vascular smooth muscle cells
WT	wild-type

Abstract

Hypertension presents a major risk factor for various secondary complications, including heart failure and chronic kidney disease (CKD). Gain-of-function mutations in the phosphodiesterase 3A (*PDE3A*) gene cause hypertension with brachydactyly (HTNB). HTNB resembles essential hypertension; however, the few examined patients exhibited almost no signs of end-organ damage. The study aimed to validate the hypothesis that HTNB-causing *PDE3A* mutations protect from hypertension-induced end-organ damage and gain insight into the underlying molecular mechanisms.

This study provided a characterization of the heart and kidney phenotypes in patient with HTNB and in two HTNB rat models. Despite hypertension, the morphology of hearts and kidneys of HTNB patient and rats carrying HTNB-causing *PDE3A* mutations remained unchanged, except for hyperplasia of resistance arteries in these organs. Serum and urine parameters in patient and animals were within the normal ranges or only slightly deviated from reference values. Further examination of HTNB rats revealed no signs of inflammation and fibrosis in the heart and kidney, which are typically detected as a consequence of hypertension. Transcriptome analysis revealed only subtle differences between the kidneys and hearts of HTNB and wild-type rats.

In the kidney's inner medulla of HTNB rats, the protein expression of the pro-fibrotic agent amphiregulin (AREG) was decreased. The mRNA expression of renin, a blood pressure-elevating agent, was downregulated in the kidneys of HTNB rats and upregulated in animals with a functional knockout of *Pde3a*, which was available as a control.

HTNB rats responded to a catecholamine challenge with isoproterenol in a manner similar to that of wild-type animals. Previous findings have pointed toward improved heart contractility in HTNB patients and in HTNB rats (Ercu et al., 2022). Sarcoplasmic reticulum calcium ATPase 2A (SERCA2A) is one of the key players in the excitation-contraction coupling machinery because it promotes Ca^{2+} reuptake into the sarcoplasmic reticulum (SR), therefore inducing cardiac relaxation. SERCA2A activity is controlled, among others, by its interaction with PDE3A1. Phosphorylation of SERCA2A at serine residue 663 has been shown to promote this interaction.

In summary, these findings indicate that HTNB-causing *PDE3A* mutations protect against hypertension-induced end-organ damage. The molecular mechanisms of PDE3A-mediated reno- and cardioprotection include the attenuation of tissue fibrosis in the kidney and modulation of cardiac myocyte contractility in the heart.

Zusammenfassung

Hypertonie ist ein wichtiger Risikofaktor für verschiedene sekundäre Komplikationen, darunter Herzversagen und chronische Nierenerkrankungen. *Gain-of-function*-Mutationen im Phosphodiesterase-3A-Gen (PDE3A) verursachen Hypertonie mit Brachydaktylie (HTNB). HTNB ähnelt der essenziellen Hypertonie; die wenigen untersuchten Patienten wiesen jedoch fast keine Anzeichen von Endorganschäden auf. Ziel der Studie war es, die Hypothese zu validieren, dass HTNB-verursachende *PDE3A*-Mutationen vor Hypertonie-induzierten Endorganschäden schützen, und Einblicke in die zugrunde liegenden molekularen Mechanismen zu gewinnen.

Diese Studie lieferte eine Charakterisierung des Herz- und Nierenphänotyps bei HTNB-Patienten und zwei HTNB-Rattenmodellen. Trotz Hypertonie blieb die Morphologie von Herz und Nieren der HTNB-Patienten und der Ratten, die HTNB-verursachende *PDE3A*-Mutationen trugen, unverändert, mit Ausnahme einer Hyperplasie der Widerstandsarterien in diesen Organen. Die Serum- und Urinparameter der Patienten und der Tiere lagen im normalen Bereich oder wichen nur geringfügig von den Referenzwerten ab. Die weitere Untersuchung der HTNB-Ratten ergab keine Anzeichen von Entzündungen und Fibrose in Herz und Niere, die typischerweise als Folge von Bluthochdruck auftreten. Die Untersuchung des Transkriptoms ergab nur subtile Unterschiede zwischen den Nieren und Herzen von HTNB- und Wildtyp-Ratten.

In der inneren Medulla der Niere von HTNB-Ratten war die Proteinexpression des pro-fibrotischen Amphiregulins (AREG) vermindert. Die mRNA-Expression des blutdrucksteigernden Agens Renin war in den Nieren von HTNB-Ratten herunterreguliert und bei Tieren mit funktionellem Knockout von Pde3a, die als Kontrolle zur Verfügung standen, hochreguliert.

HTNB-Ratten reagierten auf eine Katecholaminbelastung mit Isoproterenol in ähnlicher Weise wie Wildtyp-Tiere. Frühere Befunde wiesen auf eine verbesserte Kontraktilität der Herzen von HTNB-Patienten und von HTNB-Ratten hin (Ercu et al., 2022). Die Ca^{2+}-ATPase 2A des sarkoplasmatischen Retikulums (SERCA2A) ist einer der Hauptakteure in der Erregungs-Kontraktions-Kopplungsmaschinerie, da sie die Ca^{2+}-Wiederaufnahme in das sarkoplasmatische Retikulum (SR) fördert und so die kardiale Entspannung induziert. Die Aktivität von SERCA2A wird unter anderem durch seine Interaktion mit PDE3A1 gesteuert. Es hat sich gezeigt, dass die Phosphorylierung von SERCA2A am Serinrest 663 diese Interaktion fördert.

Zusammenfassend deuten diese Ergebnisse darauf hin, dass HTNB-verursachende *PDE3A*-Mutationen vor durch Bluthochdruck verursachten Endorganschäden schützen. Zu den molekularen Mechanismen der PDE3A-vermittelten Nieren- und Kardioprotektion gehören die Abschwächung der Gewebefibrosein der Niere und die Modulation der Kontraktilität der Herzmuskelzellen im Herzen.

1 Introduction

1.1 Hypertension and its complications

1.1.1 The definition of hypertension

The American Heart Association (AHA) defines hypertension as a blood pressure of 130/80 mmHg, and at least 1.3 billion individuals across the globe meet this criterion (Di Palo and Barone, 2020, Ercu et al., 2023). Approximately 90 % of them have primary (essential) hypertension when the initial cause of increased blood pressure cannot be distinguished. The remaining 10 % represent secondary hypertension caused by an identifiable factor, such as gene mutation, renal, endocrine, vascular, and other disorders, or side effects of drug intake (Ercu et al., 2023, Padmanabhan et al., 2015). Hypertension is a leading cause of various secondary complications. Hypertension may induce left ventricular hypertrophy and microalbuminuria, which further progress and frequently result in stroke, heart attack, heart failure, CKD, and hypertensive retinopathy (Messerli et al., 2007, Gargiulo et al., 2015).

1.1.2 Hypertension is a major risk factor for heart failure and CKD

Cardiovascular diseases cause approximately 19 million deaths every year, making them the leading cause of death worldwide (Tsao et al., 2022). Among the various cardiovascular diseases, approximately 50 % of cases account for heart failure (Disease et al., 2017, Ercu et al., 2023), which can be defined as the inability of the heart muscle to pump blood and supply the peripheral tissue with sufficient amount of oxygen (Khera et al., 2018, Mo et al., 2023). A long-term persistent increase in blood pressure impairs the contractility of cardiac myocytes and decreases cardiac output. Furthermore, it leads to the development of oxidative stress, inflammation, mitochondrial dysfunction, and apoptosis, which result in cardiac myocyte loss, myocardial fibrosis, cardiac hypertrophy, and culminate in heart failure (Schirone et al., 2017).

Hypertension is also a major risk factor for CKD (Mennuni et al., 2014, Sholokh and Klussmann, 2021). Currently, more than 800 million people worldwide suffer from CKD, and at least 25 % of them have treatment-resistant hypertension (Kovesdy, 2022, Sholokh and Klussmann, 2021). CKD is characterized by a decreased kidney function with an estimated glomerular filtration rate (eGFR) lower than 60 mL/min/1.73 m² or the

presence of kidney damage or both for at least 3 months (Webster et al., 2017). Hypertension causes CKD by stretching glomerular capillaries, endothelial cell damage, podocyte destruction, and an increase in glomerular protein filtration. Compromised endothelial cells switch to producing an exceeding amount of extracellular matrix molecules. Augmentation of glomerular filtration promotes tubular reabsorption of proteins and mesangial cell proliferation. Mesangial cells, in turn, activate the renin-angiotensin-aldosteron system (RAAS), producing vascular permeability factors, transforming growth factor (TGF-β), and fibronectin. These events culminate in inflammation, fibrosis, and glomerulosclerosis (Mennuni et al., 2014, Folkow et al., 1977, Pavenstadt et al., 2003).

1.1.3 Treatment options for hypertension and its complications are limited

Currently, a conventional protocol for hypertension treatment entails RAAS inhibitors (angiotensin-converting enzyme inhibitors or angiotensin-2 receptor blockers), Ca^{2+}-channel blockers, diuretics, and β-blockers. The overall goal of this treatment is to induce relaxation and widen the blood vessels, decrease the volume of the bloodstream, and reduce the workload on the heart (Al-Makki et al., 2022). However, the treatment at best allows for controlling and slowing disease progression. More specific and effective approaches for the treatment or even prevention of the disease are not yet available.

Comparable scenarios arise in the context of treating hypertension-induced conditions such as heart failure or CKD. The treatment strategy for heart failure is similar and, for example, in the case of heart failure with reduced ejection fraction, may include a combination of drugs to reduce the overactivation of the neurohormonal system; drugs with positive ionotropic effects (β-adrenergic agonists or phosphodiesterase inhibitors) to improve the heart contractility; diuretics to reduce the workload of the heart; and sodium-glucose cotransporter-2 (SGLT-2) inhibitors, blood sugar lowering agents, which were shown to reduce the blood pressure and preserve renal function (Ahmad et al., 2019, Mo et al., 2023).

The management of CKD aims to reduce the level of kidney damage and protect the body from further CKD-mediated events, which can be achieved by a combination of medications to lower blood pressure (RAAS inhibitors and diuretics), prevent or decrease hyperglycemia (SGLT-2 inhibitors) and correct metabolic acidosis (Charles and Ferris, 2020).

These circumstances emphasize the need to develop approaches that increase the efficiency of treatment or are even directed toward preventing hypertension and its secondary complications.

1.2 Hypertension with brachydactyly type E (HTNB)

1.2.1 Features and cause of HTNB

Hypertension with brachydactyly type E (HTNB) is a rare Mendelian disease that has been identified in only approximately 20 families worldwide (Ercu et al., 2022). HTNB patients have progressive hypertension with blood pressure values reaching 190/100 mmHg and hyperplasia of the peripheral arteries. The elevation of blood pressure in HTNB is attributed to the augmented proliferation rate of vascular smooth muscle cells (VSMCs) and increased media-to-lumen ratio in second-order arteries, resulting in increased peripheral vascular resistance. Another feature of HTNB is the short fingers and short stature, which do not compromise the patients. If untreated, HTNB leads to stroke and death by the age of 50 years (Ercu et al., 2020, Ercu et al., 2022, Maass et al., 2015, Sholokh et al., 2023).

HTNB is caused by missense gain-of-function mutations in the gene encoding cyclic guanosine monophosphate (cGMP)-inhibited cyclic adenosine monophosphate (cAMP) phosphodiesterase 3A (*PDE3A*). The gene encodes three PDE3A protein isoforms, PDE3A1-3 (Figure 1.1) (Toka et al., 2015). PDE3A1 is predominantly expressed in cardiac myocytes, PDE3A2 in VSMCs, and PDE3A3 in placenta (Ercu and Klussmann, 2018, Choi et al., 2001). At least 12 different mutations causing HTNB have been identified. The majority of the mutations were found in exon 4. These mutations result in amino acid substitutions within a “hotspot” region located N-terminally of the catalytic domain of both PDE3A1 and PDE3A2 (specifically at amino acid residues 445 - 449) (Ercu et al., 2020, Ercu et al., 2022, Ercu et al., 2023). Another mutation that causes HTNB was mapped to exon 13, which encodes the PDE3A catalytic domain. This mutation affects all three PDE3A isoforms, A1-A3 (Ercu et al., 2020, Ercu et al., 2022).

PDE3A belongs to the superfamily of phosphodiesterases (PDEs), enzymes that hydrolyze cAMP and/or cGMP (Baillie et al., 2019, Ercu and Klussmann, 2018). The PDE superfamily comprises at least 100 different PDEs, divided into 11 families (PDE1-PDE11). The predominant PDEs in the kidney and heart are PDE1-PDE5, PDE8, and PDE9 (Ercu and Klussmann, 2018, Sholokh and Klussmann, 2021). PDE3A hydrolyzes

both cAMP and cGMP (Degerman et al., 1997). However, it has a 4-10-fold higher V_{max} for cAMP than for cGMP, and therefore preferentially utilizes cAMP as a substrate (Degerman et al., 1997). In the context of HTNB, mutant PDE3A enzymes exhibit hyperactivity, hyperphosphorylation, and increased interaction with 14-3-3θ (Ercu et al., 2020, Ercu et al., 2022, Toka et al., 2015).

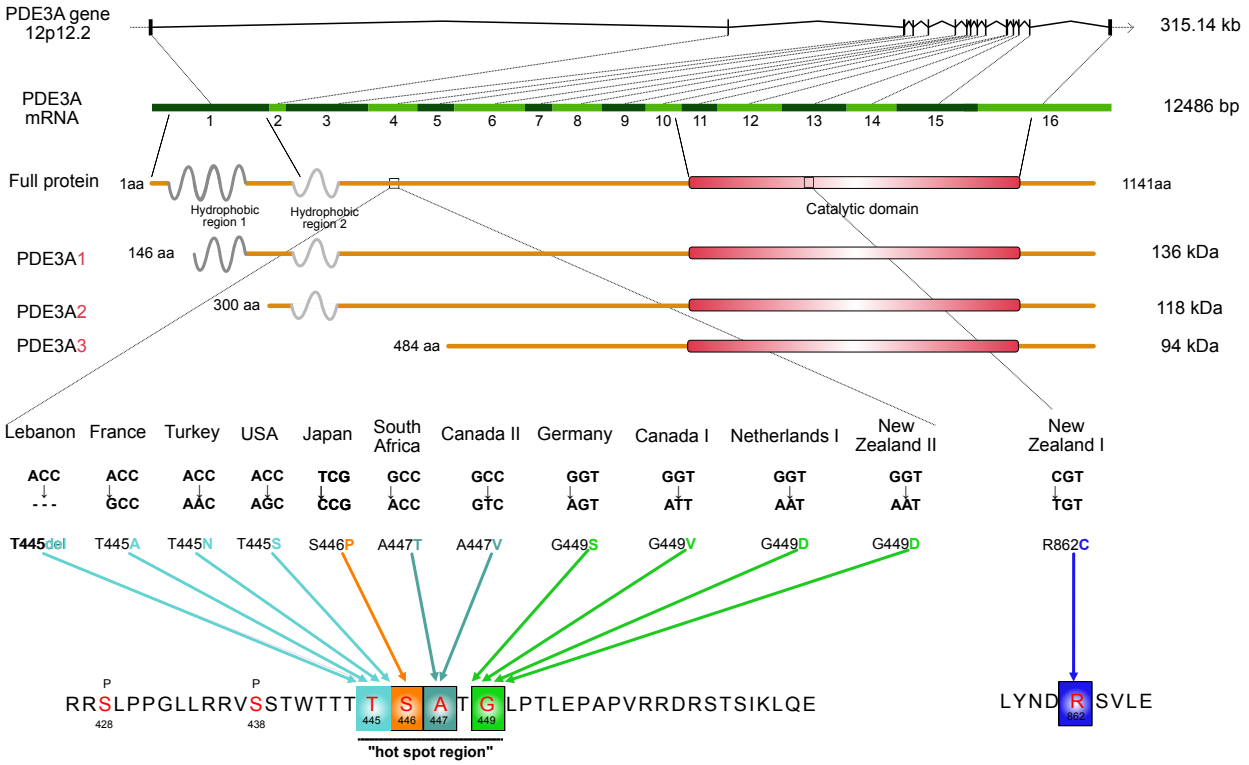

Figure 1.1. *PDE3A* gene, protein isoforms, and the location of HNTB-causing *PDE3A* mutations (adapted from Ercu et al., 2020, Ercu et al., 2022). aa - amino acid, P - phosphorylation.

1.2.2 Hypertension without end-organ damage in HTNB patients

HTNB resembles essential hypertension but, surprisingly, does not cause cardiac and kidney damage (Ercu et al., 2022, Schuster et al., 1996b, Toka et al., 2015). Examination of five family members with HTNB who were not receiving antihypertensive treatment showed that they presented with systolic blood pressure in the range of 170-250 mmHg and diastolic blood pressure in the range of 100-150 mmHg, while the unaffected person had a blood pressure of 120/70 mmHg. The body mass index of the affected individuals did not change. The hearts of all affected individuals were overall normal; only one person had coronary disease associated with increased levels of low-density lipoprotein. Stroke volumes in all patients were normal. The patients had no ab-

dominal abnormalities or edema. The examined HTNB-affected individuals also demonstrated no changes in the levels of serum electrolytes, renin plasma activity, and urine excretion of Na^+, K^+, Ca^{2+}, and phosphate in comparison to unaffected family member. Only one of the five affected family members had small intrarenal calculi and two had microalbuminuria. None of the patients had signs of renal artery stenosis. Complete blood count, sugar levels, and liver function were unaffected in all HTNB individuals. Thus, the data suggested that despite having extremely high blood pressure, HTNB patients demonstrated no or very little cardiac and renal damage (Schuster et al., 1996b).

Studies on rat models that recapitulate HTNB also indicated that serum electrolyte levels, urine levels of albumin, creatinine, urea nitrogen, and fractional excretion of electrolytes remained within the ranges of reference values (Ercu et al., 2020, Ercu et al., 2022).

These data suggested that despite having hypertension, patients with HTNB and rodent models of HTNB were protected from hypertension-induced end-organ damage. Considering the current limitations of treatment approaches for hypertension and its complications, understanding the molecular mechanisms underlying PDE3A-mediated cardio- and renoprotection may help to develop more precise and effective strategies for both the prevention and treatment of hypertension and its associated complications.

1.3 Aim of the thesis

The aim of the thesis was to perform a detailed investigation of the effect of PDE3A-induced hypertension on the heart and kidney using HTNB rat models and, to a limited extent, data from HTNB patient.

Characterization of the HTNB phenotypes of the heart and kidney will help to gain insight into the molecular mechanisms of PDE3A-mediated protection from hypertension-induced end-organ damage. This knowledge also could lay the foundation for the development of more specific and effective approaches for the treatment of hypertension and its associated complications.

2 Methods

2.1 Evaluation of the patient data

An HTNB patient carrying the PDE3A-G449S substitution underwent continuous monitoring at MVZ Nierenzentrum Limburg (Germany) for at least 5 years. The patient confirmed participation in the study and publication of the results by written informed consent. The Ethical Committee of the Charité and local Internal Review Boards approved the studies (Ercu et al., 2022).

2.2 HTNB rat models

Rats carrying HTNB-causing *Pde3a*-mutations were generated using CRISPR/Cas9 technology in a close collaboration with AG Bader (Max Delbrück Center for Molecular Medicine, MDC). The following animal models were established:

1. Rats with a deletion in exon 4 of the *Pde3a* gene, which was achieved by the deletion of 9 base pairs and led to a loss of amino acid residues 441-443 in the rat PDE3A protein (amino acid residues 444-446 in human PDE3A) (Ercu et al., 2020). This deletion is analogous to the human HTNB-causing T445del genotype (Renkema et al., 2018) (PDE3A-Δ3aa rats).
2. Animals with a single base pair substitution in exon 13 (led to an arginine to cysteine substitution at amino acid residue 862, PDE3A-R862C rats) (Ercu et al., 2022).

Heterozygous PDE3A-Δ3aa and homozygous PDE3A-R862C rats displayed all HTNB-phenotype features including hypertension, peripheral vessel hyperplasia, and brachydactyly (Ercu et al., 2020, Ercu et al., 2022).

3. Rats with a deletion of 20 base pairs in the *Pde3a* gene, which caused a frameshift and expression of a truncated protein (functional DEL rats). Functional DEL animals did not display any features of HTNB (Ercu et al., 2020).

Wild-type (WT) Sprague-Dawley rats were used as controls in all the experiments.

2.3 Animal handling

All experiments were performed on 20–30 weeks-old Sprague-Dawley male rats (450–650 g). Approval for obtaining tissues from adult rats was obtained from the local authorities: “Tötungsanzeige”, Landesamt für Gesundheit und Soziales, Berlin, LaGeSo

(license no. Y 9001/19), MDC (license no. Y 9001/19), and conducted in accordance with the guidelines of the American Physiological Society (Ercu et al., 2022, Sholokh et al., 2023).

To investigate the effect of catecholamine stress on the rat heart, animals were treated with isoproterenol (0.13 $mg \cdot kg^{-1} \cdot h^{-1}$) through osmotic minipumps (Alzet 2ML2, Charles River Wiga, Sulzfeld) for 14 days. Control rats received 0.9 % NaCl (with 0.02 % ascorbic acid) (Ercu et al., 2022).

Animals were sacrificed; kidneys and hearts were removed and immediately placed on ice. The kidneys' inner medullas were separated from the residual kidney; the left ventricles were dissected from the rest of the heart. Inner medullas, residual kidneys, and heart left ventricles were snap-frozen in liquid nitrogen and stored at -80°C until further processing unless different is specified.

For the evaluation of urine parameters, animals were placed in metabolic cages and 24-hour urine was collected. Blood was collected from the tail vein. Further analysis of the serum and urine samples was performed using an AU480 Beckman Coulter chemistry analyzer.

2.4 Histological staining and immunofluorescence microscopy

Upon autopsy, rat kidneys and hearts were immediately cut along the coronal and transverse axes, respectively, fixed in 10 % formalin (at least 24 hours) and embedded in paraffin (4 °C, overnight). Sections (5 µm) were cut, mounted on microscope slides, deparaffinized, and further rehydrated by subjecting them to decreasing concentrations of ethanol (100 - 30 % range). The stainings were performed as described in Table 2.1.

Table 2.1: Protocols for the bright-field and immunofluorescence staining (Ercu et al., 2022, Sholokh et al., 2023).

Type of staining	Type of imaging	Steps and incubations
Hematoxylin & Eosin	Bright-field	Staining: Hematoxylin (Sigma-Aldrich, GHS332), 10 min Washing: tap water, 10 min Differentiation: 0.3 % acidic alcohol Washing: tap water, 10 min Staining: Eosin (Sigma-Aldrich, HT110116), 2 min Dehydration: ethanol, 80, 90, 100 %, isopropanol.

Type of staining	Type of imaging	Steps and incubations
Picro-Sirius red	Bright-field	Staining: Picro-Sirius red (Morphisto, 13422), 60 min Washing: 0.005 % vinegar water (2 x 5 min) Dehydration: ethanol (3 x 100 %)
ED1-positive cells	Immuno-fluorescence	Boiling: 1x citrate buffer*, 20 min Blocking of endogenous peroxidases: 3 % H_2O_2,15 min Washing: distilled water, 3x5min Blocking: 10 % normal donkey serum (NDS), 37 °C, 60 min, humidified chamber Staining: primary antibody# in 10 % NDS, 4 °C, overnight, humidified chamber Washing: Phosphate-buffered saline (PBS)**, 3 x 5 min Staining: secondary antibody## in 10 % NDS, DAPI: 2 h Washing: PBS, 3 x 5 min, humidified chamber Mounting: VECTASHIELD® Antifade Mounting Medium with 4', 6-diamidine-2'-phenylindole dihydrochloride (DAPI)

* 10 mM Sodium citrate, pH 6.0; 0.05 % Tween 20

** 137 mM NaCl, 2.7 mM KCl, 1.5 mM KH_2PO_4, 8.1 mM, Na_2HPO_4, pH 7.4

#Anti-ED1, 1:50 (MCA341R, Bio-Rad Laboratories)

##Cy3-conjugated donkey anti-mouse IgG, 1:300 (715-165 Jackson ImmunoResearch Laboratories Inc.)

The last step for Hematoxylin & Eosin and Picro-Sirius red stainings included 30 min incubation in xylene, followed by mounting with Eukitt (Fluka Analytical, 0001448137). All steps were performed at room temperature unless otherwise specified.

Tissue sections were imaged using an All-in-One Light/Fluorescence Microscope BZ-9000 (Keyence) or a Pannoramic MIDI Slide Scanner (3D Histec). At least five non-overlapping images from each sample were analyzed using ImageJ or Case Viewer software. Bowman's capsule and glomerular tuft areas, the media-to-lumen ratio of renal and cardiac arteries, percentage of collagen area, number of ED1-positive cells, and cardiac myocyte area were determined. To calculate the media-to-lumen ratio, the tunica media area was divided by the luminal area (Ercu et al., 2022, Sholokh et al., 2023).

2.5 Western blotting

To isolate proteins from the kidneys, tissue samples were homogenized using a rotor-stator homogenizer in lysis buffer containing 50 mM Tris-HCl, pH 7.4, 150 mM NaCl, 1 mM Ethylenediaminetetraacetic acid (EDTA), 0.5 % sodium deoxycholate, 0.5 % Tri-

ton X-100, 0.1 % sodium dodecyl sulfate, and supplemented with 1mM dithiothreitol (DTT), protease and phosphatase inhibitors (Thermo Fisher Scientific, A32955, A32957) before beginning the lysis procedure. Tissue lysates were centrifuged at 14,000 rpm for 15 min at 4° C. The supernatant was collected and the protein concentration was determined using the Coomassie Plus Bradford protein assay (Thermo Fisher Scientific, 1856210) according to the manufacturer's protocol. The absorbance was measured using a microplate reader Enspire® 2300 (PerkinElmer). Each Western blot sample contained 30 µg of protein lysate, Laemmli sample buffer, and lysis buffer to adjust the sample volume.

Proteins were separated by sodium dodecyl sulfate-polyacrylamide gel electrophoresis and subsequently transferred onto a polyvinylidene fluoride (PVDF) membrane. To prevent non-specific antibody binding, PVDF membranes were incubated in blocking solutions for 1 hour at room temperature (either 5 % bovine serum albumin or 5 % skim milk in Tris-buffered saline (TBS: 10 mM Tris-HCl pH 7.4, 150 mM NaCl), followed by overnight incubation with primary antibodies (the list of primary antibodies, including the blocking buffers, can be found in Sholokh et al. 2023, in the "Supplemental materials"). The following day, the membranes were washed with TBS-T (TBS + 0.05 % Tween-20), 3 x 10 min, incubated with secondary antibodies coupled to horseradish peroxidase (HRP) for 1 hour at room temperature, and washed with TBS-T, 3 x 10 min. To detect the chemiluminescent signal corresponding to the amount of protein in the samples, the membranes were incubated with Immobilon® Western chemiluminescent HRP substrate (Millipore, WBKLS0500) and imaged using an Odyssey Imager (LI-COR Biosciences) (Sholokh et al., 2023).

2.6 Reverse transcription quantitative real-time polymerase chain reaction (RT-qPCR)

The inner medullas and residual kidneys were homogenized using a rotor-stator homogenizer in lysis buffer obtained from the GeneMATRIX Universal RNA Purification Kit (EURx Ltd., E3598). RNA was isolated according to the manufacturer's protocol. To eliminate contamination with genomic DNA, the samples were treated with 1.5 U DNAse I (Roboclon, E1345) for 15 min. RNA concentration and quality were determined using NanoDrop ND-1000 (PeqLab Biotechnologie GmbH). All manipulations were performed at the room temperature. Reverse transcription was performed using the qScript cDNA

Synthesis Kit (Quantabio, 95047-100) according to the manufacturer's protocol with 600 ng of total RNA. The obtained cDNA was mixed with DNA primers and Power SYBR™ Green PCR Master Mix (Thermo Fisher Scientific, 4368706).

Primers were designed using the NCBI primer-BLAST tool and spanned exon-exon junctions. The list of primers is available in Sholokh et al. 2023, in the "Supplemental materials". Gene expression levels were determined using the $2^{-\Delta\Delta Ct}$ method and expressed as fold change relative to the control group (wild-type) (Sholokh et al., 2023).

2.7 RNA sequencing

The inner medullas, residual kidneys, and heart left ventricles were cryopulverized using a Covaris cryoPREP Dry Pulverizer. The cryopulverized tissue was mixed with lysis buffer from the GeneMATRIX Universal RNA Purification Kit. Further steps of the RNA purification process were the same as described in Section 2.6. The RNA concentration was measured using nano-drop and Qubit systems. The RNA integrity number (RIN) was determined using a high sensitivity RNA bioanalyzer (Agilent, 5067-5581). Only RNA samples with RIN values > 8 for the kidney and RIN values > 7 for the heart were used for further experiments.

RNA sequencing libraries were prepared using the TruSeq Stranded mRNA kit (Illumina, 20020595) according to the manufacturer's protocol. Sequencing was performed using a HiSeq 4000 platform (Illumina) in multiplexed dual-indexed mode (1x151 + 8In + 8In) (Ercu et al., 2022, Sholokh et al., 2023).

Library preparation and sequencing were performed at the Genomics Technology Platform (MDC, Berlin). The data were analyzed by Daniele Yumi Sunaga-Franze and Tatiana Borodina (MDC, Berlin); Brandon J McMurray and Philipp G Maass (Genetics and Genome Biology Program, SickKids Research Institute, Toronto, ON). A detailed description of the data analysis pipeline can be found in Ercu et al. 2022, in the "Supplemental materials".

2.8 Enzyme-linked Immunosorbent Assay (ELISA)

Protein lysates from the inner medullas were prepared as described in Section 2.5, except using a different lysis buffer (10 mM K_2HPO_4, pH 7.4, 150 mM NaCl, 5 mM EDTA, 5 mM ethylene glycol tetraacetic acid, 1 % Triton X-100, 0.2 % sodium deoxycholate, supplemented with fresh 1 mM DTT, protease and phosphatase inhibitors).

Blood was collected from the tail vein and serum was separated from the blood and stored at -20 °C. ELISA was performed using the Rat AR (Amphiregulin) ELISA Kit (FineTest, ER0745) according to the manufacturer's protocol (Sholokh et al., 2023).

2.9 Cell transfection and immunoprecipitation

Human embryonic kidney 293 (HEK293) cells were cultured in Dulbecco's Modified Eagle Medium (DMEM)-GlutaMAX^{TM} supplemented with 10 % fetal calf serum and 1 % penicillin/streptomycin. For the experiments, 2x10^6 HEK293 cells were seeded on 10 cm plates. After 24 hours of culturing, cells were co-transfected with 3 µg of HA-PDE3A1 and 3 µg of FLAG-SERCA wild-type, FLAG-SERCA-S663A or FLAG-SERCA-S663D construct (all constructs were cloned by Carolin Schächterle, AG Klussmann, MDC). Transfection was performed in antibiotic-free media, which was changed back to the culturing media 5 hours after transfection. The following day, cells underwent 30 min stimulation with epidermal growth factor (EGF), diluted in the culture media (100 ng/mL). The control cells did not receive any stimulation agent. After the incubation, cells were washed with ice-cold PBS, scraped in lysis buffer (described in Section 2.8), transferred to the reaction tube, lysed by passing through a syringe (20 G x 1.5" needle), and subjected to the lysis procedure described in Section 2.5.
For the immunoprecipitation of FLAG-SERCA, 600 ug of protein lysate was mixed with 15 µl of Anti-FLAG® M2 Magnetic Beads (Sigma-Aldrich, M8823). The total volume of the mix was adjusted to 1 mL by adding the corresponding amount of lysis buffer. Lysate with beads was incubated for 18 hours at 4 °C under constant agitation. The beads suspension was washed with lysis buffer (4 times) and the elution was performed with the FLAG® peptide (Sigma-Aldrich, SLCJ5577), 15 min, 37 °C, 1,000 rpm. The eluate was mixed with Laemmli sample buffer and subjected to the Western blot procedure as described in Section 2.5. PDE3A was detected with anti-HA-HRP antibody (GENETEX, 115044-01), 1:10,000 in 5 % milk; SECA2A with SERCA2 ATPase Monoclonal Antibody (Thermo Fisher Scientific, MA3-919), 1:2,000 in 5 % milk.

2.10 Other methods

Isolation and measurement of *Vasa recta* contractility were performed by Minze Xu from the group of Andreas Patzak (Charité - Universitätsmedizin Berlin) and described in Sholokh et al. 2023, in the "Supplemental materials".

Radioimmunoassays for evaluation of cAMP and cGMP tissue levels were performed by Michael Russwurm (Institut für Pharmakologie und Toxikologie, Bochum) and described in Brooker et al., 1979.

2.11 Statistical analysis

Statistical analysis of all experiments, except for *Vasa recta* contractility measurements and RNA sequencing, was carried out using GraphPad Prism 9.1.0. In the first step, data distribution was evaluated using the Shapiro-Wilk test. Data sets with a normal distribution (P Shapiro-Wilk > 0.05) were analyzed using one-way analysis of variance (ANOVA) with the Tukey multiple-comparisons test, while data sets with non-normal distribution underwent Kruskal-Wallis with Dunn multiple-comparisons test. Data sets comprising only two groups were analyzed using the unpaired t-test (normal distribution) or the Mann-Whitney test (non-normal distribution). Data sets obtained from the experiments with isoproterenol/NaCl treatment were evaluated using two-way ANOVA with the Tukey multiple-comparisons test.

Data are presented as means with a standard error of the mean (SEM). The differences between groups were considered to be significant if the P value was < 0.05. Outliers were removed using the ROUT method (Q = 1%).

3 Results

3.1 Clinical examination of HTNB patient: almost no heart and kidney damage

HTNB is a rare disease and the ability to obtain data from patients with HTNB is limited. We collaborated with Dr. Walter, MVZ Nierenzentrum Limburg (Germany), who has been engaged in the treatment of an HTNB patient for more than five years. Dr. Walter provided the results of a 16-hour blood pressure measurement, echocardiography, ultrasound investigation of the heart and kidney, and data from blood and urine analyses.

The 60-years-old HTNB patient, despite receiving an antihypertensive treatment, still demonstrated an increased mean blood pressure of 160/102 mmHg (Ercu et al., 2022). Echocardiography showed almost no signs of cardiac damage, no left ventricular hypertrophy (septal wall thickness, 8 mm; posterior, 10 mm), preserved ejection fraction (56 %), and no pathological changes in the right ventricle and aortic valve. However, the left ventricular end-diastolic diameter was slightly increased (61 mm). A detailed description of the morphology of HTNB patient's heart can be found at Ercu et al., 2022.

Ultrasound examination of the kidneys of HTNB patient showed that their morphology was not affected despite severe hypertension. The right kidney was 9.82 cm (expected:0.028 x 158 cm height + 5.202 cm = 9.626 cm), and the left kidney was 7.7 cm (expected:0.038 x 158 cm height + 3.948 cm = 9.952 cm) (Abdullah MB, 2014, Sholokh et al., 2023). These values were lower than expected in unaffected individuals. This might be explained by the fact that patients with HTNB are shorter and have lower body weight (Schuster et al., 1996b).

The five-year long-term monitoring of kidney function revealed that the eGFR and serum creatinine levels of the HTNB patient remained within the ranges of reference values for most of the monitoring period (Figure 3.1, A). Urine analysis showed no signs of albuminuria, erythrocytes, and normal levels of Na^+ and K^+ (Figure 3.1, B). In the serum, electrolyte levels remained within or slightly deviated from the reference ranges (Figure 3.1, C). Renin levels were suppressed, which is most likely the result of antihypertensive treatment, whereas aldosterone levels were not altered (Sholokh et al., 2023). Therefore, HTNB, under intensive antihypertensive treatment, had almost no effect on heart and kidney morphology and function.

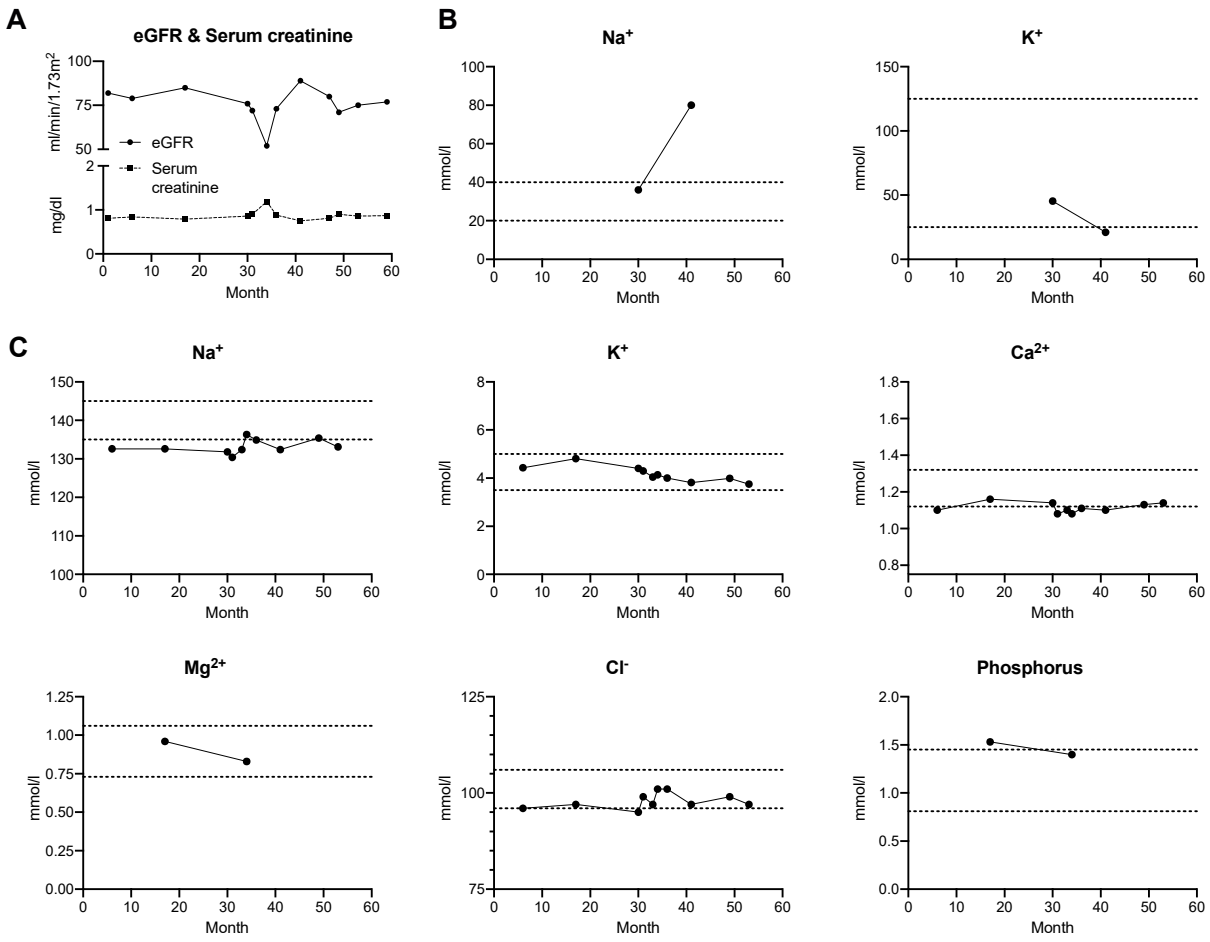

Figure 3.1. Blood and urine parameters of an HNTB patient are not changed.

A. eGFR and serum creatinine levels. **B**. Urine electrolytes. **C**. Serum electrolytes. Dashed lines indicate the ranges of reference values (own figure, modified according to Sholokh et al., 2023).

3.2 HTNB rats are protected from hypertension-induced kidney damage

3.2.1 HTNB affected kidney vessels but not kidney morphology

In response to elevated blood pressure, kidneys develop a protective mechanism that includes an increase in vessel wall thickness and a decrease in the luminal diameter to reduce vascular wall stress (Mennuni et al., 2014). However, in the long term, this leads to ischemic injury of the surrounding tissue and promotes kidney injury. HTNB patients exhibited hyperplasia of the peripheral arteries (Bahring et al., 2008). HTNB rats also showed an increased media-to-lumen ratio in second-order mesenteric arteries (Ercu et al., 2020, Ercu et al., 2022), but not in the aorta (Figure 3.2, A). In the kidneys of PDE3A-Δ3aa and PDE3A-R862C animals, the media-to-lumen ratios of the resistance arteries were higher than those of the wild-type (Figure 3.2, B). Surprisingly,

the contractility of isolated *Vasa recta* was not significantly different between PDE3A-Δ3aa, functional DEL and wild-type rats (Figure 3.2, C). In the second-order mesenteric arteries of PDE3A-Δ3aa rats, vasodilation was compromised (Ercu et al., 2020). Thus, the renal vessel function was apparently unaffected in the HTNB model. The unchanged contractility of functional DEL was consistent with reduced blood pressure.

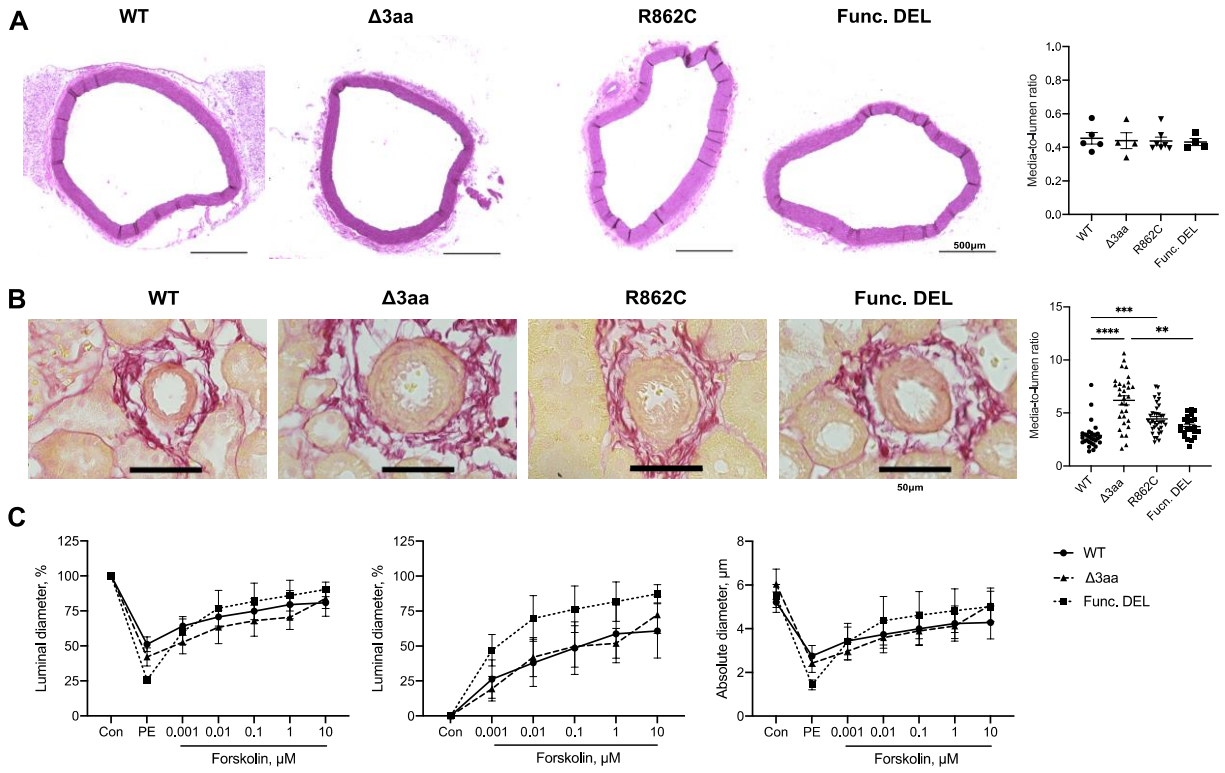

Figure 3.2. Only renal resistance arteries are affected in HTNB rat models. Media-to-lumen ratio of the aorta (**A**) and renal resistance arteries (**B**). For aorta WT, n = 5; PDE3A-Δ3aa, n = 4; PDE3A-R862C, n = 7; Func. DEL, n = 4. Statistical analysis: one-way ANOVA and Tukey multiple-comparisons test. For renal resistance arteries WT, n = 5; PDE3A-Δ3aa, n = 5; PDE3A-R862C, n = 3; Func. DEL, n = 5. Statistical analysis: Kruskal-Wallis and Dunn multiple-comparisons test; **P<0.01; ***P<0.001, ****P<0.0001. **C**. Contractility of isolated *Vasa recta.* WT, n = 5; PDE3A-Δ3aa, n = 6; Func. DEL, n = 3. Statistical analysis: non-parametric Brunner test, no significant differences. Data shown are mean ± SEM. *Vasa recta* isolation and contractility measurements were performed by Minze Xu (Charité – Universitätsmedizin Berlin) (own figure, modified according to Sholokh et al., 2023).

Rats with HTNB were lighter than wild-type animals (Ercu et al., 2022, Ercu et al., 2020). However, their kidney-to-body weight ratios were not different from those of wild-type animals (Figure 3.3, A). PDE3A-Δ3aa and PDE3A-R862C rats displayed no change in kidney morphology. The Bowman's capsule and glomerular tuft areas were

not altered (Figure 3.3, C, D). The evaluation of creatinine clearance, 24-hours excretion levels of $Na^{+,}$ $K^{+,}$ and Cl^{-} showed no difference between HTNB and wild-type rats (Figure 3.3, E). There was no albuminuria. Serum electrolyte levels were also not significantly different from those in wild-type animals (Ercu et al., 2020, Ercu et al., 2022). mRNA expression of renin was downregulated in PDE3A-Δ3aa rats, unchanged in PDE3A-R862C animals, and upregulated in the functional DEL group, all compared to the wild-type rats (Figure 3.3, B). This was in line with previous data, showing trends of decreasing renin levels in the blood of PDE3A-Δ3aa rats and increasing in functional DEL animals (Ercu et al., 2020).

The kidney encompasses several dozens of different cell types (Schumacher et al., 2021). Within the kidney, the inner medulla has a notably lower blood supply and oxygen levels, rendering it more susceptible to injury caused by hypertension compared to the rest of the kidney (Edwards and Kurtcuoglu, 2022). Therefore, in further experiments, the inner medulla and residual kidney were investigated separately.

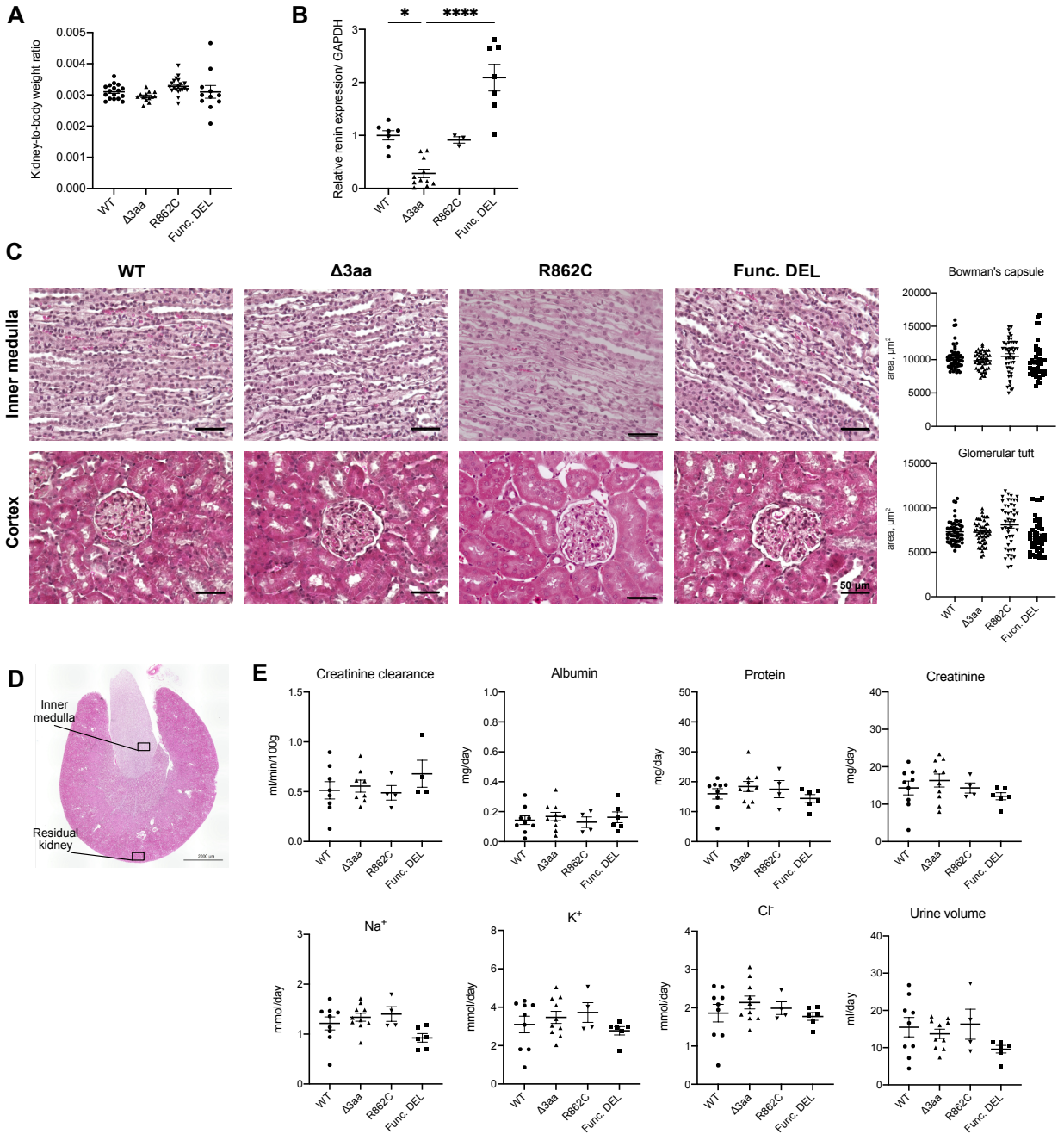

Figure 3.3. Kidneys from HTNB rats do not show obvious signs of hypertension-induced damage. A. Kidney-to-body weight ratio. WT, n = 17; PDE3A-Δ3aa, n = 13; PDE3A-R862C, n = 20; Func. DEL, n = 11. Statistical analysis: one-way ANOVA and Tukey multiple-comparisons test, no significant differences. **B.** mRNA expression levels of renin in the kidney**.** WT, n = 7; PDE3A-Δ3aa, n = 11; PDE3A-R862C, n = 3; Func. DEL, n = 7. Statistical analysis: Kruskal-Wallis and Dunn multiple-comparisons tests. *P<0.05; ***P<0.001. **C**, **D**. Hematoxylin and eosin staining for determining the areas of Bowman's capsule and glomerular tuft. WT, n = 5; PDE3A-Δ3aa, n = 5; PDE3A-R862C, n = 3; Func. DEL, n = 5. Statistical analysis: Kruskal-Wallis and Dunn multiple-comparisons tests, no significant differences. **E.** Analysis of the urine samples collected during 24 hours. WT, n = 9; PDE3A-Δ3aa, n = 10; PDE3A-R862C, n = 4;

Func. DEL, n = 6. Statistical analysis: one-way ANOVA and Tukey multiple-comparisons test or Kruskal-Wallis and Dunn multiple-comparisons tests, no significant differences. Data shown are mean ± SEM (own figure, modified according to Sholokh et al., 2023).

PDE3A protein expression was downregulated in the inner medulla and residual kidney of both HTNB rat models (Figure 3.4, A). Similar downregulation was observed in the heart and aorta. Mutant PDE3A is hyperactive (Ercu et al., 2020, Ercu et al., 2022). Therefore, the decrease of PDE3A expression likely acted as a compensatory mechanism, elucidating why the cAMP levels in the kidneys of HTNB rats did not significantly differ from those in wild-type animals. cGMP levels were not affected in the inner medulla and residual kidney of HTNB rats (Figure 3.4, B). As expected, no PDE3A expression was detected in the kidneys of functional DEL animals. The lack of PDE3A did not affect global cAMP levels in the inner medulla or residual kidney (Figure 3.4, A).

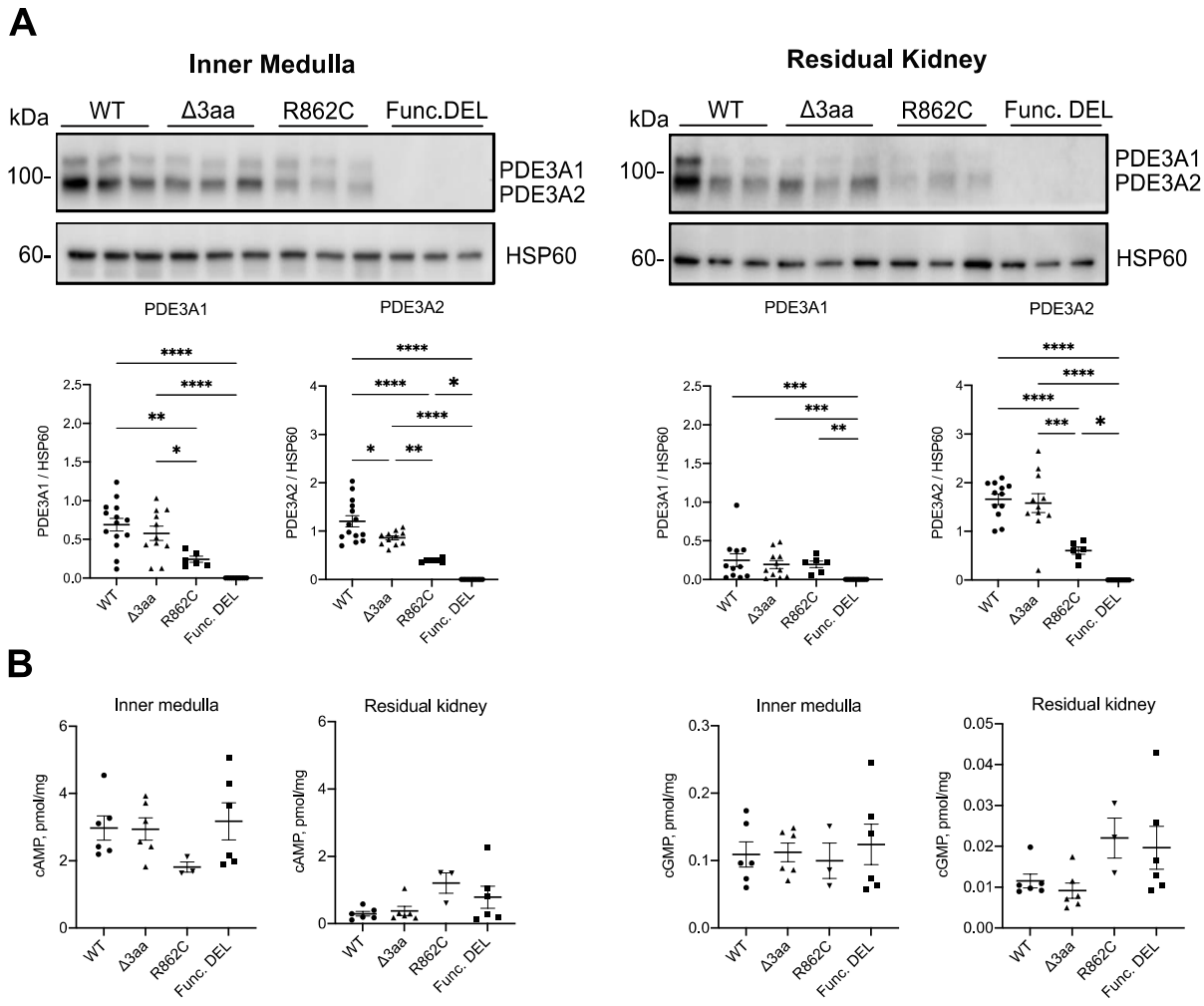

Figure 3.4. Mutant PDE3A is downregulated in the kidney, but the cAMP and cGMP levels are not affected. A. Western blot detection of PDE3A protein expression in

the inner medulla and residual kidney. WT, n = 14; PDE3A-Δ3aa, n = 14; PDE3A-R862C, n = 6; Func. DEL, n = 11. Statistical analysis: Kruskal-Wallis and Dunn multiple-comparisons tests; **P < 0.01, ***P < 0.001, and ****P < 0.0001. **B.** Tissue levels of cAMP and cGMP in the inner medulla and residual kidney. WT, n = 6; PDE3A-Δ3aa, n = 6; PDE3A-R862C, n = 3; Func. DEL, n = 6. Statistical analysis: Kruskal-Wallis and Dunn multiple-comparisons test, no significant differences. Data shown are mean ± SEM. cAMP and cGMP measurements were performed by Michael Russwurm (Institut für Pharmakologie und Toxikologie, Bochum). HSP60 - Heat shock protein 60 (own figure, modified according to Sholokh et al., 2023).

Collectively, these data showed that hypertension-causing *Pde3a* mutations affected renal vessels, but did not have a noticeable effect on kidney structure or function.

3.2.2 Mutant PDE3A is not associated with inflammation and fibrosis in rat kidneys upon HTNB

Inflammation and fibrosis are typical hallmarks of hypertension-induced kidney damage, leading to CKD development (Sholokh and Klussmann, 2021, Son et al., 2021). Investigation of the mRNA expression of genes associated with kidney inflammation, such as tumor necrosis factor-α (TNF-α), C-C motif chemokine 2 (CCL2), C-C motif chemokine 5 (CCL5), and vascular cell adhesion protein 1 (VCAM1), showed no differences between HTNB and wild-type rats in the inner medulla (Figure 3.5, A). A similar analysis in the residual kidney revealed only an increase in TNF-α mRNA in PDE3A-R862C animals compared to that in wild-type and PDE3A-Δ3aa rats (Figure 3.5, B). Immunofluorescence staining with the pan-macrophage marker ED1 did not reveal any differences in the number of tissue macrophages between the groups (Figure 3.5, C).

The mRNA levels of the classical markers of kidney fibrosis, fibronectin, TGF-β1, and smooth muscle actin alpha 2 (ACTA2), were similar in the inner medulla (Figure 3.6, A) and residual kidneys (Figure 3.6, B) in all animal groups. Tissue collagen staining did not reveal signs of extracellular matrix molecule accumulation in any genotype, except for a subtle increase in the percentage of collagen area in the inner medulla of functional DEL rats (Figure 3.6, C). No change in ACTA2 expression was observed at the protein level, confirming the RT-qPCR results (Figure 3.6, D).

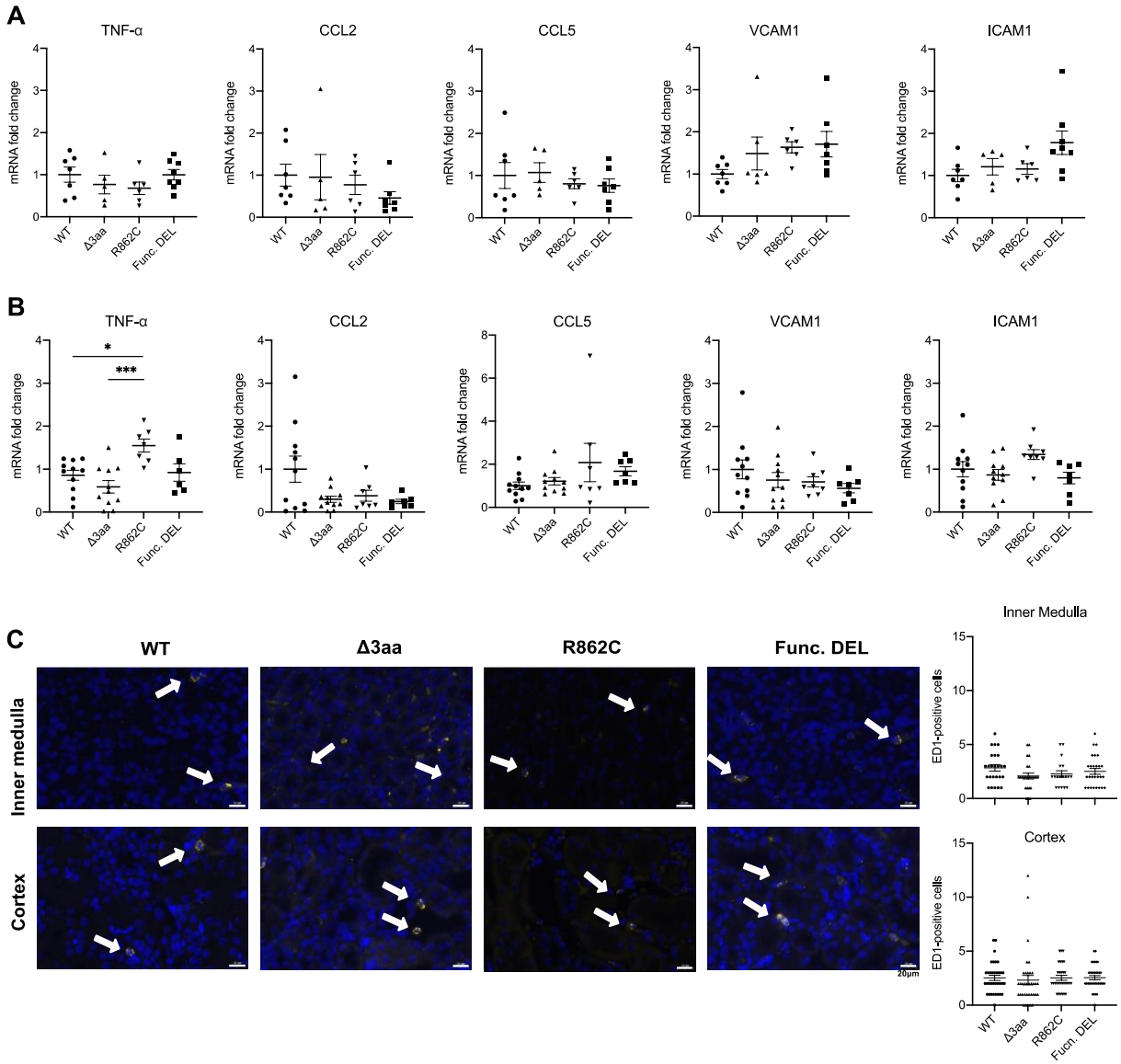

Figure 3.5. HTNB is not associated with inflammation in kidneys of rat models. mRNA expression of inflammation markers in the inner medulla **(A)** and residual kidney **(B).** For the inner medulla WT, n = 7; PDE3A-Δ3aa, n = 6; PDE3A-R862C, n = 6; Func. DEL, n = 8. For the residual kidney WT, n = 11; PDE3A-Δ3aa, n = 11; PDE3A-R862C, n = 8; Func. DEL, n = 7. Statistical analysis: one-way ANOVA and Tukey multiple-comparisons test or Kruskal-Wallis and Dunn multiple-comparisons test; **P* <0.05, ****P* <0.001. **C.** Immunofluorescence staining for ED1-positive macrophages. WT, n = 5; PDE3A-Δ3aa, n = 5; PDE3A-R862C, n = 3; Func. DEL, n = 5. Statistical analysis: Kruskal-Wallis and Dunn multiple-comparisons test, no significant differences. Data shown are mean ± SEM (own figure, modified according to Sholokh et al., 2023).

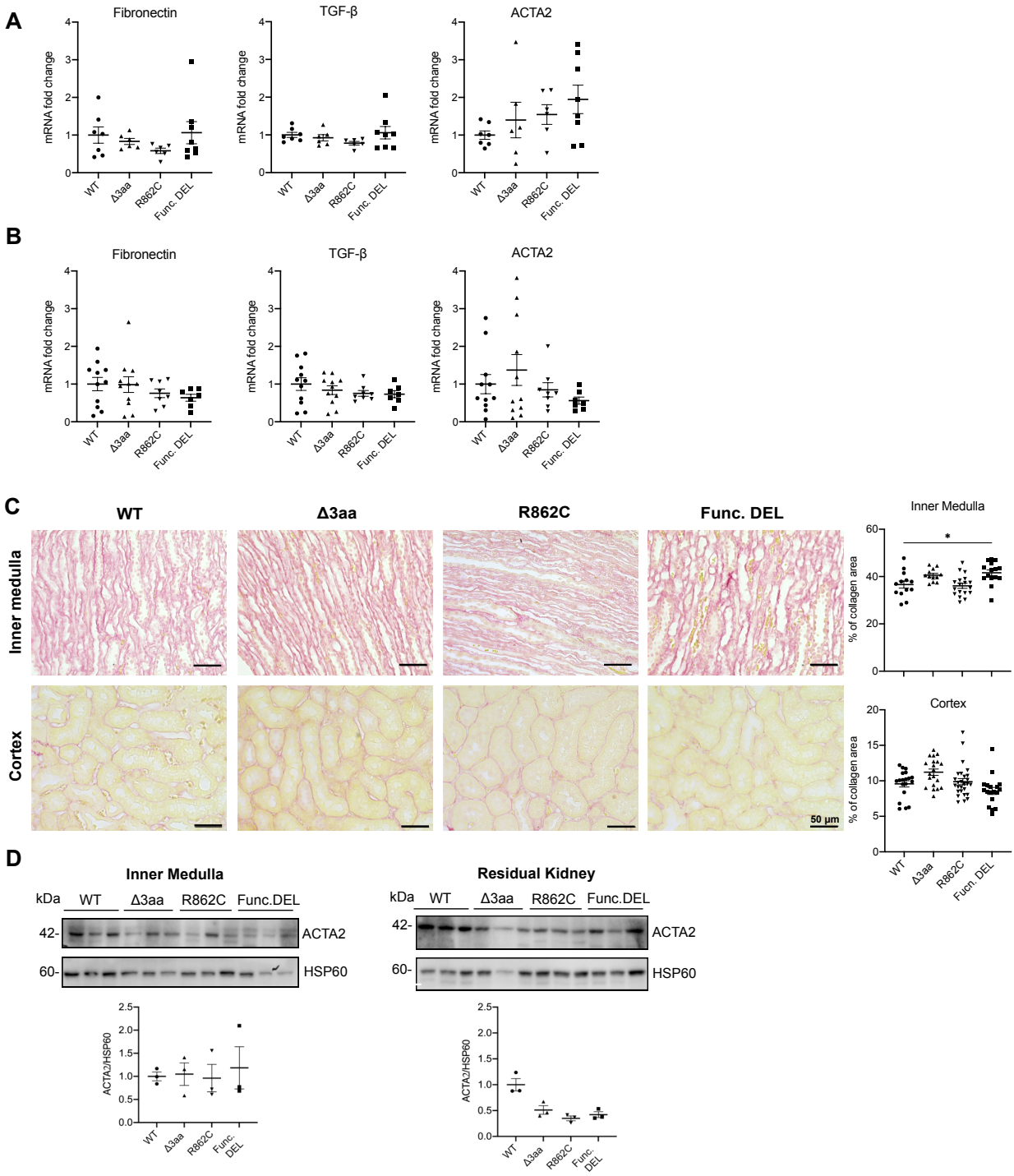

Figure 3.6. HTNB is not associated with tissue fibrosis in kidneys of rat models. mRNA expression of fibrosis markers in the inner medulla **(A)** and residual kidney **(B).** For the inner medulla WT, n = 7; PDE3A-Δ3aa, n = 6; PDE3A-R862C, n = 6; Func. DEL, n = 8. For the residual kidney WT, n = 11; PDE3A-Δ3aa, n = 11; PDE3A-R862C, n = 8; Func. DEL, n = 7. Statistical analysis: one-way ANOVA and Tukey multiple-comparisons test or Kruskal-Wallis and Dunn multiple-comparisons test, no significant differences. **C.** Picro-Sirius red staining of collagen fibers in the kidney. WT, n = 5; PDE3A-Δ3aa, n = 5; PDE3A-R862C, n = 3; Func. DEL, n =

5. Statistical analysis: Kruskal-Wallis and Dunn multiple-comparisons test; *P <0.05. **D.** Western blot detection of ACTA2 expression in the inner medulla and residual kidney. n = 3 per genotype. Statistical analysis: one-way ANOVA and Tukey multiple-comparisons test, no significant differences. Data shown are mean ± SEM (own figure, modified according to Sholokh et al., 2023).

Thus, mutant PDE3A protects kidneys from hypertension-induced damage, which is usually evident in CKD.

3.2.3 AREG is downregulated in kidneys of HTNB rats

To investigate the mechanisms of PDE3A-mediated renoprotection on the molecular levels, mRNA sequencing of the inner medulla and residual kidney of PDE3A-Δ3aa and wild-type rats and the residual kidney of functional DEL animals was performed. The expression of only 83 genes (41 upregulated and 42 downregulated) was affected in the inner medulla and 11 genes (8 upregulated and 3 downregulated) in the residual kidney of PDE3A-Δ3aa rats compared to the wild-type. (Figure 3.7, A, C). In the residual kidney of functional DEL animals, the expression of 123 genes (82 upregulated and 41 downregulated) was affected compared to that in the wild-type. Gene ontology (GO) analysis did not reveal any distinct gene clusters related to the kidney damage or stress responses in PDE3A-Δ3aa rats (Figure 3.7, B). PDE3A is a component of cAMP signalling pathways (Ercu and Klussmann, 2018). However, there were no significant alterations in the mRNA expression levels of cAMP signalling pathway elements, such as stimulatory G protein, G_S (also other G proteins), adenylyl cyclases (AC), protein kinase A (PKA) catalytic (cat), regulatory (R) subunits, various PDEs, and A-kinase anchoring proteins in the inner medulla and residual kidney of PDE3A-Δ3aa and residual kidney of functional DEL rats compared to the wild-type (Figure 3.7, D). The only exception was the decrease in *Pde3a* expression in PDE3A-Δ3aa rats, which corresponded to the Western blotting results shown above (Figure 3.4, A). The residual expression of *Pde3a* in functional DEL rats could be explained by the presence of truncated mRNA molecules.

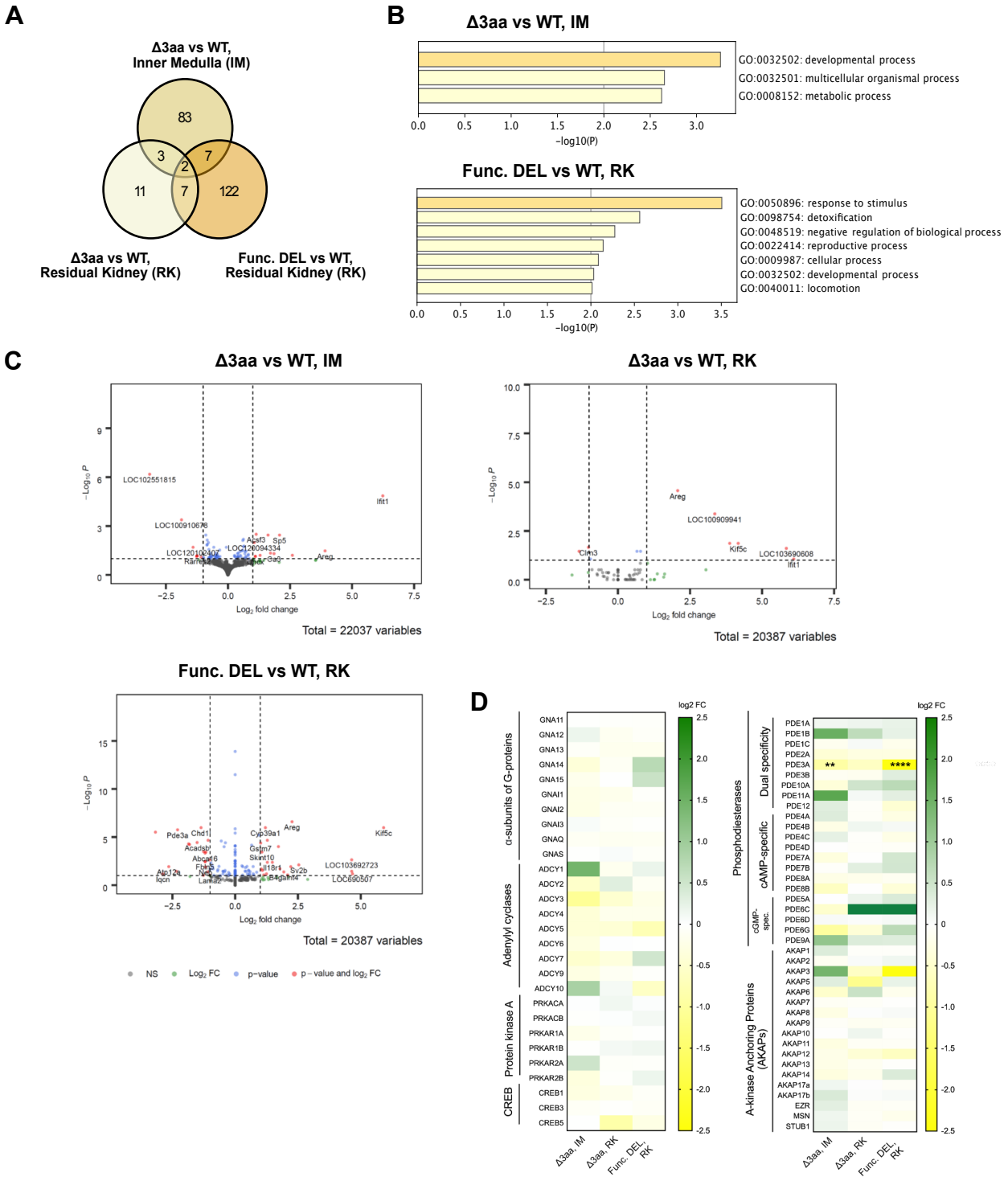

Figure 3.7. RNA sequencing of kidneys from WT, PDE3A-Δ3aa, and Func. DEL rats. A. Venn diagram with the number of differentially expressed genes in the inner medulla and residual kidney. WT, n = 3; PDE3A-Δ3aa, n = 3; Func. DEL, n = 3. **B.** GO analysis of the RNA sequencing data. **C**. Volcano plots depict the distribution of genes that are differentially expressed, with a false discovery rate threshold of 0.1 and a log2 fold change threshold of 1. **D.** Heatmaps representing the expression of cAMP signalling pathway components ***P* <0.01, *****P* <0.0001. RNA sequencing was performed in collaboration with the Genomics Technology

Platform of the MDC, Berlin. Data was analyzed by Daniele Yumi Sunaga-Franze, Tatiana Borodina, Brandon J McMurray, and Philipp G Maass (own figure, modified according to Sholokh et al., 2023).

Analysis of the protein expression of cAMP signalling pathway components confirmed the RNA sequencing results (Figure 3.8). Only an increase in S133 phosphorylation of cAMP response element-binding protein (CREB) was detected in the inner medulla of PDE3A-Δ3aa rats compared to wild-type rats.

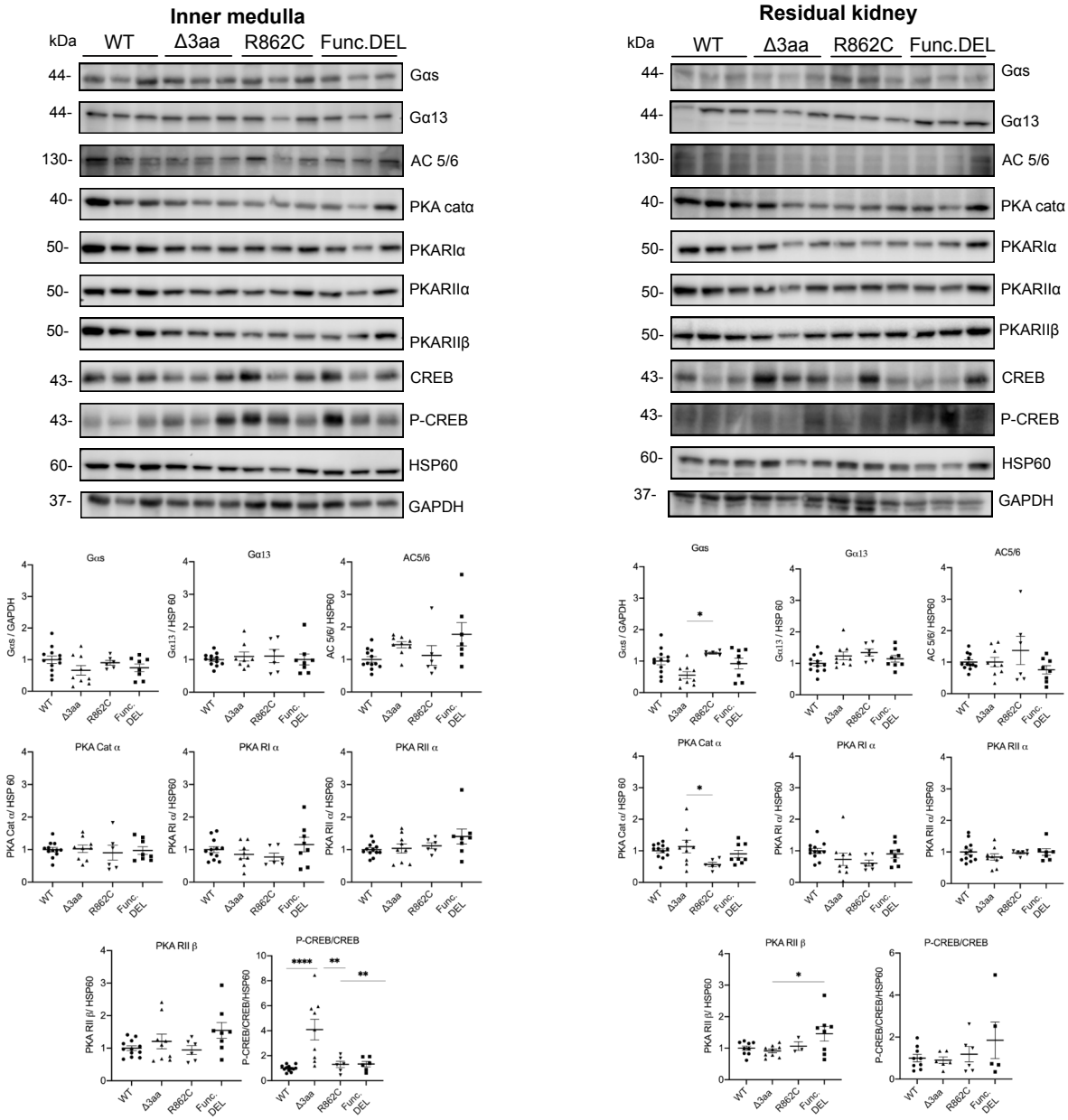

Figure 3.8. The expression levels of cAMP signalling pathway proteins are not affected in HTNB rats. WT, n = 12; PDE3A-Δ3aa, n = 9; PDE3A-R862C, n = 6; Func. DEL, n = 8. Statistical analysis: one-way ANOVA and Tukey multiple-comparisons test or Kruskal-Wallis and Dunn multiple-comparisons test; **P* <0.05, ***P* <0.01, *****P* <0.0001. Data shown are

mean ± SEM. GAPDH - Glyceraldehyde 3-phosphate dehydrogenase (own figure, modified according to Sholokh et al., 2023).

Further analysis of RNA sequencing data showed no changes in the mRNA levels of major inflammation and fibrosis markers (Figure 3.9, A), confirming the results of RT-qPCR experiments (Figures 3.5 A, B and 3.6, A, B). Only an increase in *Areg* expression was observed in PDE3A-Δ3aa and functional DEL rat kidneys. AREG induces the expression of pro-inflammatory and pro-fibrotic cytokines and promotes CKD progression (Kefaloyianni et al., 2016). In contrast, siRNA knockdown of AREG prevented CKD development in the two mouse models (Son et al., 2021). Despite the increase in *Areg* mRNA expression, its protein level was not affected in the residual kidney and decreased in the inner medulla of PDE3A-Δ3aa rats compared to wild-type animals (Figure 3.9, B). The decrease in AREG protein expression in the inner medulla was confirmed by ELISA (Figure 3.9, C). In serum, AREG levels exhibited greater variability within the PDE3A-Δ3aa group compared to the functional DEL or wild-type animals, although these differences did not become statistically significant (Figure 3.9, C). Thus, it appears that a negative feedback mechanism operates, which overcompensates for elevated mRNA expression by decreasing the AREG protein level in the inner medulla.

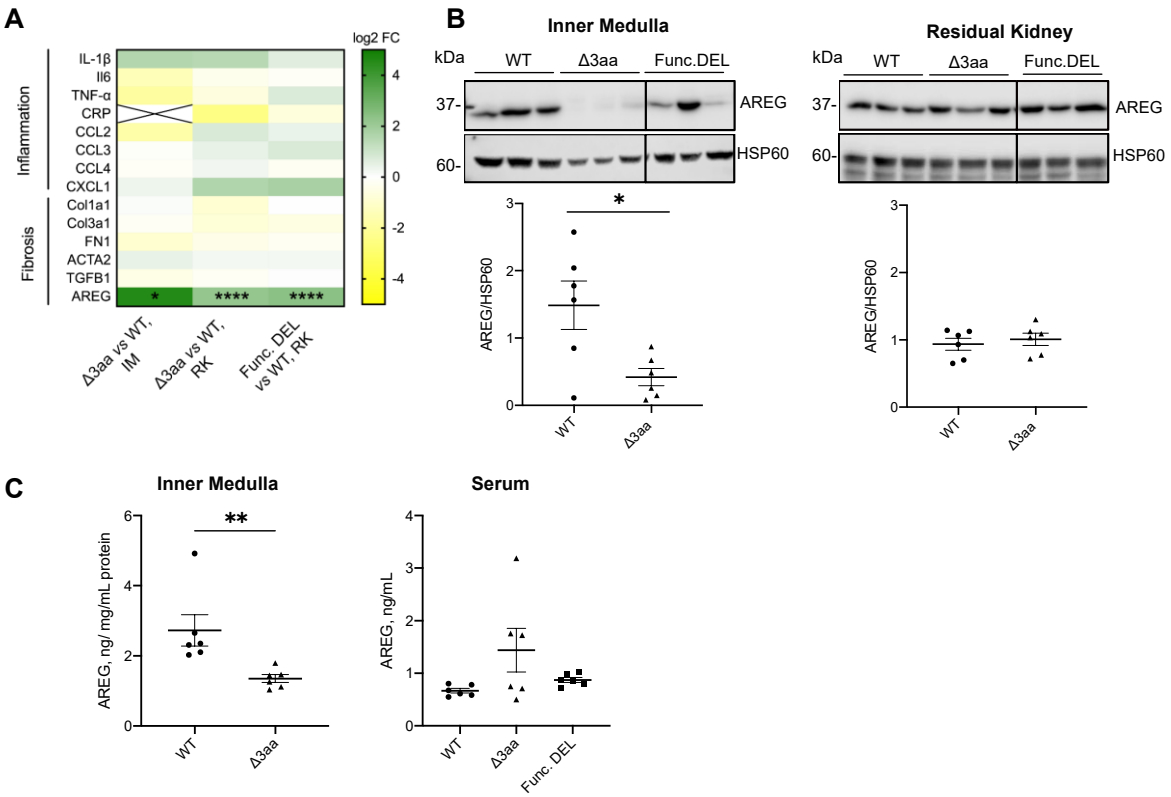

Figure 3.9. Downregulation of AREG expression is associated with HTNB in PDE3A-Δ3aa rats. A. Heatmap representing the expression of selected inflammation and

fibrosis markers (extracted from RNA sequencing). **B.** Western blot detection of AREG expression in the inner medulla and residual kidney. n = 6 per genotype. Statistical analysis: t-test; *P <0.05. **C.** AREG levels in the inner medulla and serum determined by ELISA. N = 6 per genotype. Statistical analysis: Mann-Whitney test for the inner medulla; one-way ANOVA and Tukey multiple-comparisons test for the serum samples. **P <0.01. Data shown are mean ± SEM (own figure, modified according to Sholokh et al., 2023).

AREG is an agonist of the epidermal growth factor receptor (EGFR) (Harskamp et al., 2016). Activation of EGFR leads to the phosphorylation of downstream kinases such as extracellular signal-regulated kinases 1/2 (ERK1/2) and Akt (Harskamp et al., 2016). However, the phosphorylation levels of these kinases were not affected in the inner medulla and residual kidneys of PDE3A-Δ3aa rats (Figure 3.10).

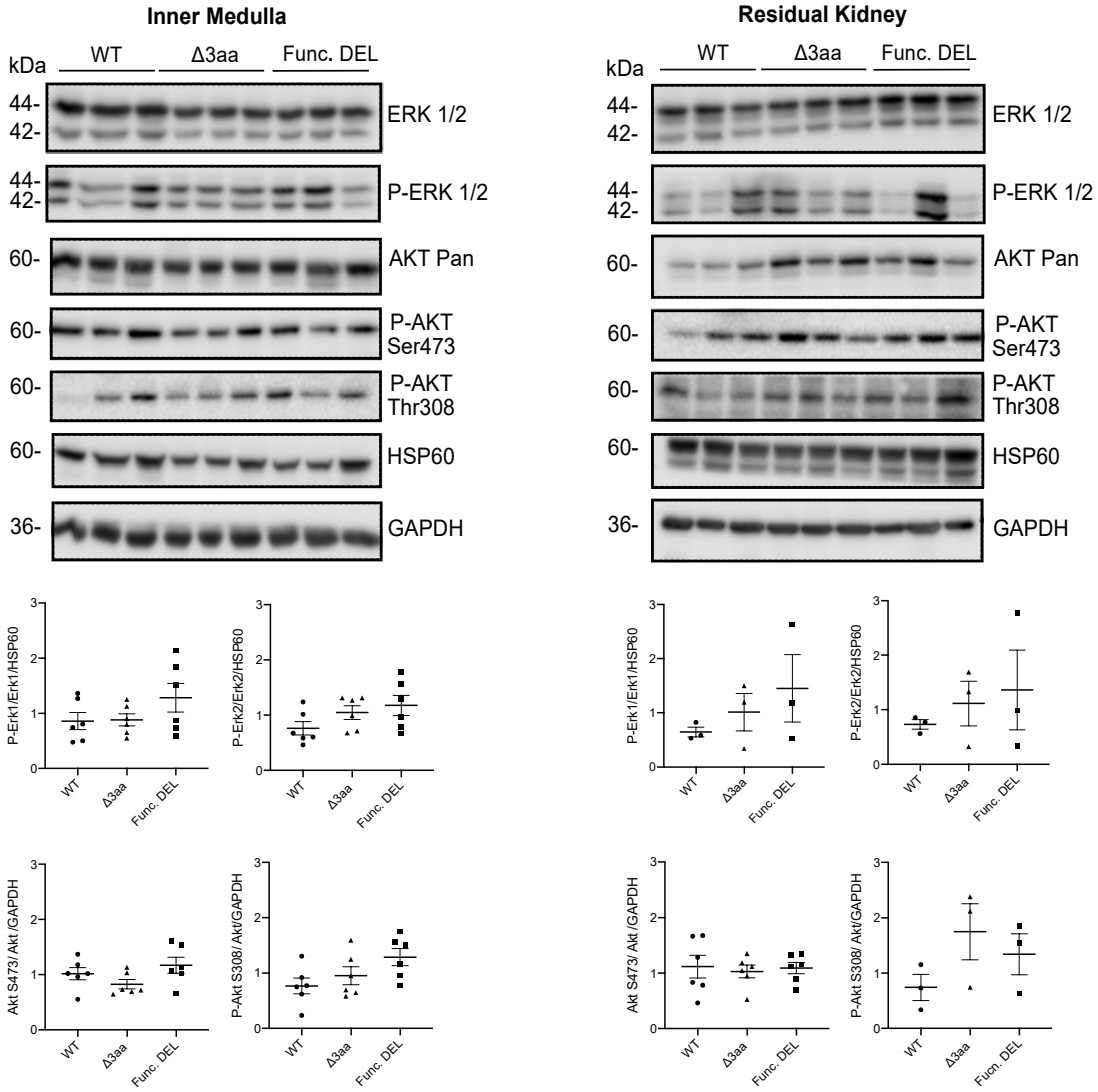

Figure 3.10. The phosphorylation levels of downstream kinases in the EGFR signalling pathway are unchanged in HTNB rats. n = 6 for all genotypes. Statistical analy-

sis: one-way ANOVA and Tukey multiple-comparisons test, no significant differences. Data shown are mean ± SEM (own figure, modified according to Sholokh et al., 2023).

In summary, the low AREG protein level most likely explains the lack of increase in fibrosis markers expression and prevents aberrant EGFR signalling in the kidneys of PDE3A-Δ3aa animals. This finding suggests that AREG contributes to PDE3A-mediated renoprotection.

3.3 HTNB rats are protected from hypertension-induced cardiac damage

3.3.1 HTNB affected cardiac vessels but not heart morphology

Cardiac hypertrophy and fibrosis are common complications of hypertension (Gonzalez et al., 2018). However, histological analysis showed that the area of cardiac myocytes of HTNB rats was comparable to that of wild-type rats, suggesting the absence of cardiac hypertrophy in HTNB animals. Picro-Sirius red staining, utilized to detect collagen fiber deposition, revealed no significant differences among the investigated phenotypes, indicating the absence of tissue fibrosis in HTNB rats. In line with previous findings in second-order mesenteric arteries (Ercu et al., 2020) and kidney resistance arteries (Sholokh et al., 2023), the media-to-lumen ratio of cardiac arteries of PDE3A-Δ3aa and PDE3A-R862C rats was increased compared to wild-type rats. In the functional DEL animals, the vessels remained unaffected, most likely due to their low blood pressure (Figure 3.11).

Investigation of the transcriptome of the left ventricles from PDE3A-Δ3aa and wild-type rats revealed minimal differences between the two genotypes, similar to the findings observed in the kidney. The mRNA expression of only 165 genes was affected in PDE3A-Δ3aa rats compared to wild-type, with 67 genes being upregulated and 98 genes being downregulated. The majority of these genes encode proteins responsible for protein folding, recognition of misfolded proteins, and positive regulation of cardiac muscle contraction (Figure 3.12).

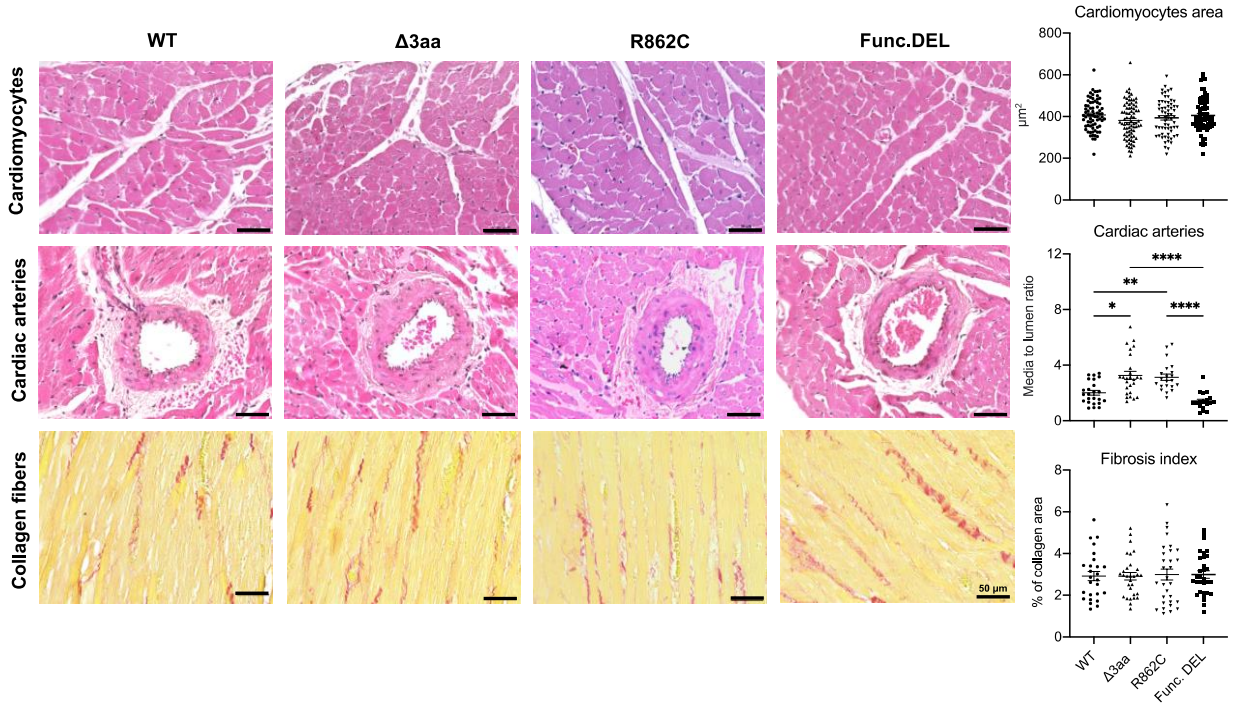

Figure 3.11. **Hearts from HTNB rats do not show obvious signs of hypertension-induced damage.** Picro-Sirius red, hematoxylin and eosin stainings. WT, n = 5; PDE3A-Δ3aa, n = 5; PDE3A-R862C, n = 3; Func. DEL, n = 5. Statistical analysis was performed using a Kruskal-Wallis and Dunn multiple-comparisons test; *P<0.05, **P<0.01, ****P<0.0001. Data shown are mean ± SEM (own figure, modified according to Ercu et al., 2022).

These results suggest that the hearts of HTNB rats were protected from hypertension-induced cardiac damage. Thus, the effects of *PDE3A* mutation extend beyond the kidney and may be defined as protection from hypertension-induced end-organ damage.

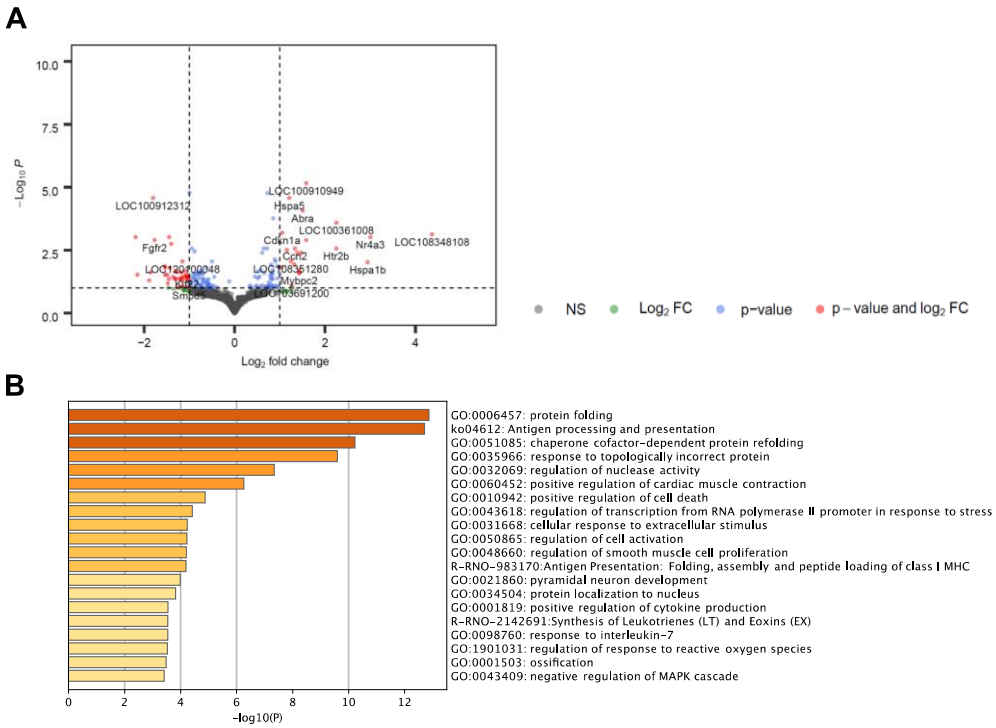

Figure 3.12. RNA sequencing of hearts from untreated WT and PDE3A-Δ3aa rats.

A. Volcano plots depict the distribution of genes that are differentially expressed. False discovery rate threshold is 0.1 and a log2 fold change threshold is 1. **B.** GO analysis of the RNA sequencing data. WT, n = 3; PDE3A-Δ3aa, n = 4. RNA sequencing was performed in collaboration with the Genomics Technology Platform of the MDC, Berlin. Data was analyzed by Daniele Yumi Sunaga-Franze, Tatiana Borodina, Brandon J McMurray, and Philipp G Maass (own figure, modified according to Ercu et al., 2022).

3.3.2 Isoproterenol induced cardiac damage in HTNB rats to the same degree as in WT

Hearts from HTNB rats showed no obvious signs of hypertension-induced cardiac damage. To investigate whether this cardioprotective effect would persist under additional stress conditions, the animals were subjected to two weeks of isoproterenol treatment. Isoproterenol is a β-adrenoreceptor agonist that increases heart rate, lowers blood pressure, and induces cardiac hypertrophy and damage in animal models (Leenen et al., 2001, Ozakca et al., 2013, Ercu et al., 2022).

Isoproterenol treatment induced an increase in heart rate and a decrease in blood pressure across all four investigated genotypes. Moreover, the wild-type and functional DEL animals after two weeks of receiving isoproterenol demonstrated an augmentation of the left ventricular mass and heart weight-to-body weight ratio compared with the val-

ues before the beginning of isoproterenol treatment. In contrast, both HTNB rat models exhibited only a tendency towards an increase in these parameters, but the differences between the values before and after two weeks of isoproterenol treatment did not reach statistical significance. Moreover, HTNB mutants exhibited increased fractional shortening, PDE3A-Δ3aa rats demonstrated an increased cardiac output, and PDE3A-R862C rats had increased ejection fraction (Ercu et al., 2022).

Histological analysis of the hearts revealed that isoproterenol treatment induced an increase in the cardiac myocyte area in all examined genotypes compared to the respective animal groups treated with NaCl. As expected, isoproterenol treatment did not affect the wall thickness of the resistance arteries in rat hearts. The percentage of collagen-positive area was significantly increased in the wild-type, PDE3A-R862C, and functional DEL groups compared to that in rats treated with NaCl. A similar trend was observed in PDE3A-Δ3aa isoproterenol-treated rats. The overall levels of damage caused by isoproterenol were comparable among all genotypes. Notably, no significant differences were observed neither in the area of the cardiac myocytes, nor in the percentage of collagen-positive area when comparing wild-type and the other genotypes treated with isoproterenol, except for a higher percentage of collagen-positive area in PDE3A-R862C compared to the wild-type (Figure 3.13).

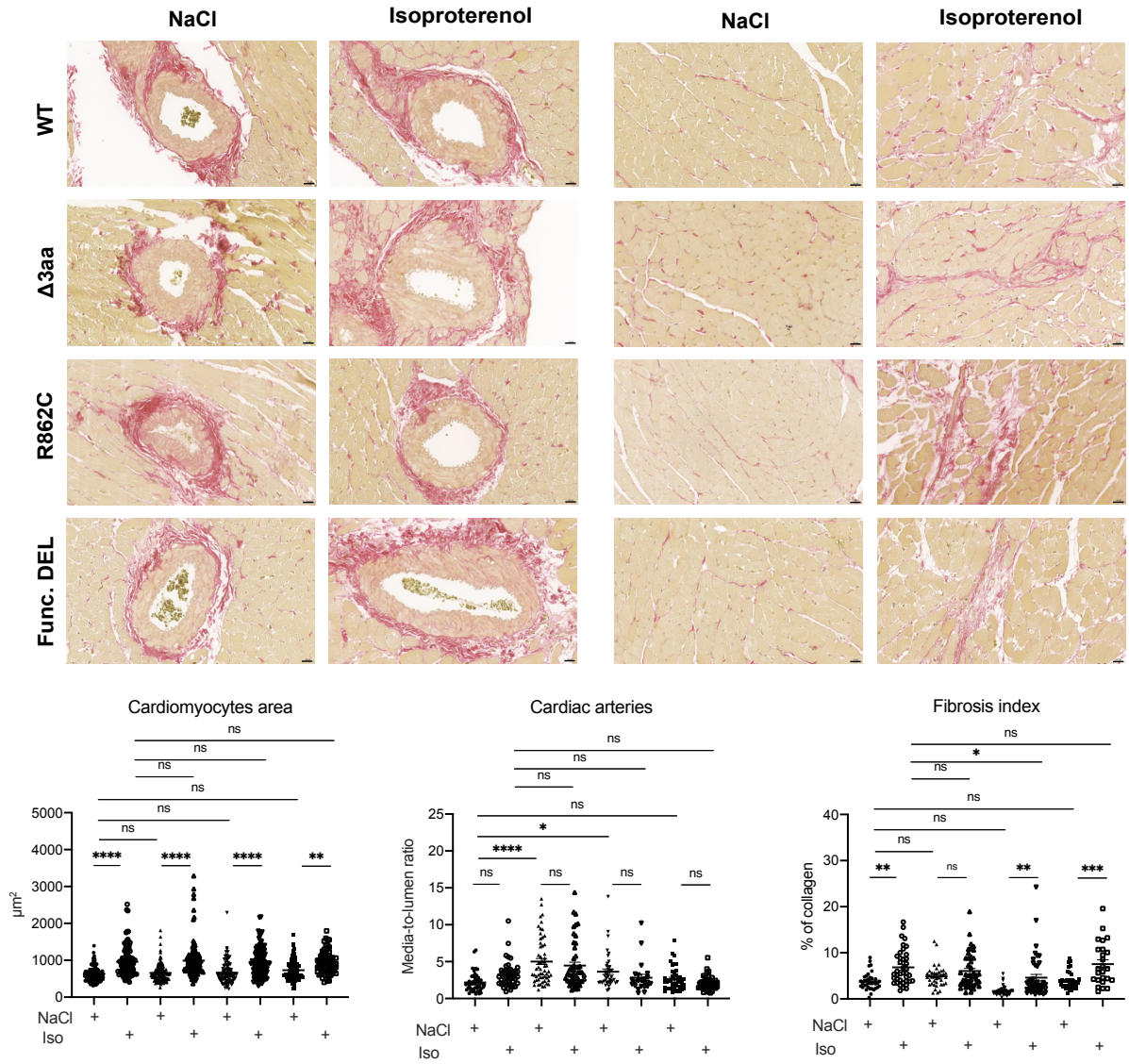

Figure 3.13. Isoproterenol-induced cardiac damage in HTNB animals is similar to that of WT. Picro-Sirius red staining. WT NaCl, n = 6; WT Iso, n = 4; PDE3A-Δ3aa NaCl, n = 6; PDE3A-Δ3aa Iso, n = 5; PDE3A-R862C NaCl, n = 4; PDE3A-R862C Iso, n = 4; Func. DEL NaCl, n = 4; Func. DEL Iso, n = 4. Statistical analysis: 2-way ANOVA with the Tukey multiple-comparisons test.; *P<0.05, **P<0.01, ***P<0.001, ****P<0.0001. Data shown are mean ± SEM. Iso-isoproterenol (own figure, modified according to Subramaniam et al., 2023)

RNA sequencing of the hearts of rats subjected to isoproterenol or NaCl treatment revealed a more pronounced impact of isoproterenol-induced cardiac stress on functional DEL animals than on PDE3A-Δ3aa rats. Isoproterenol treatment affected the expression of 1769 genes in functional DEL animals (465 were upregulated and 1304 were downregulated) and only 25 genes in PDE3A-Δ3aa rats (22 were upregulated and 3 were downregulated) compared to NaCl-treated rats of the same genotype. GO anal-

ysis of the isoproterenol-treated samples from PDE3A-Δ3aa revealed significant enrichment of genes involved in protein and Ca^{2+} regulation (Figure 3.14).

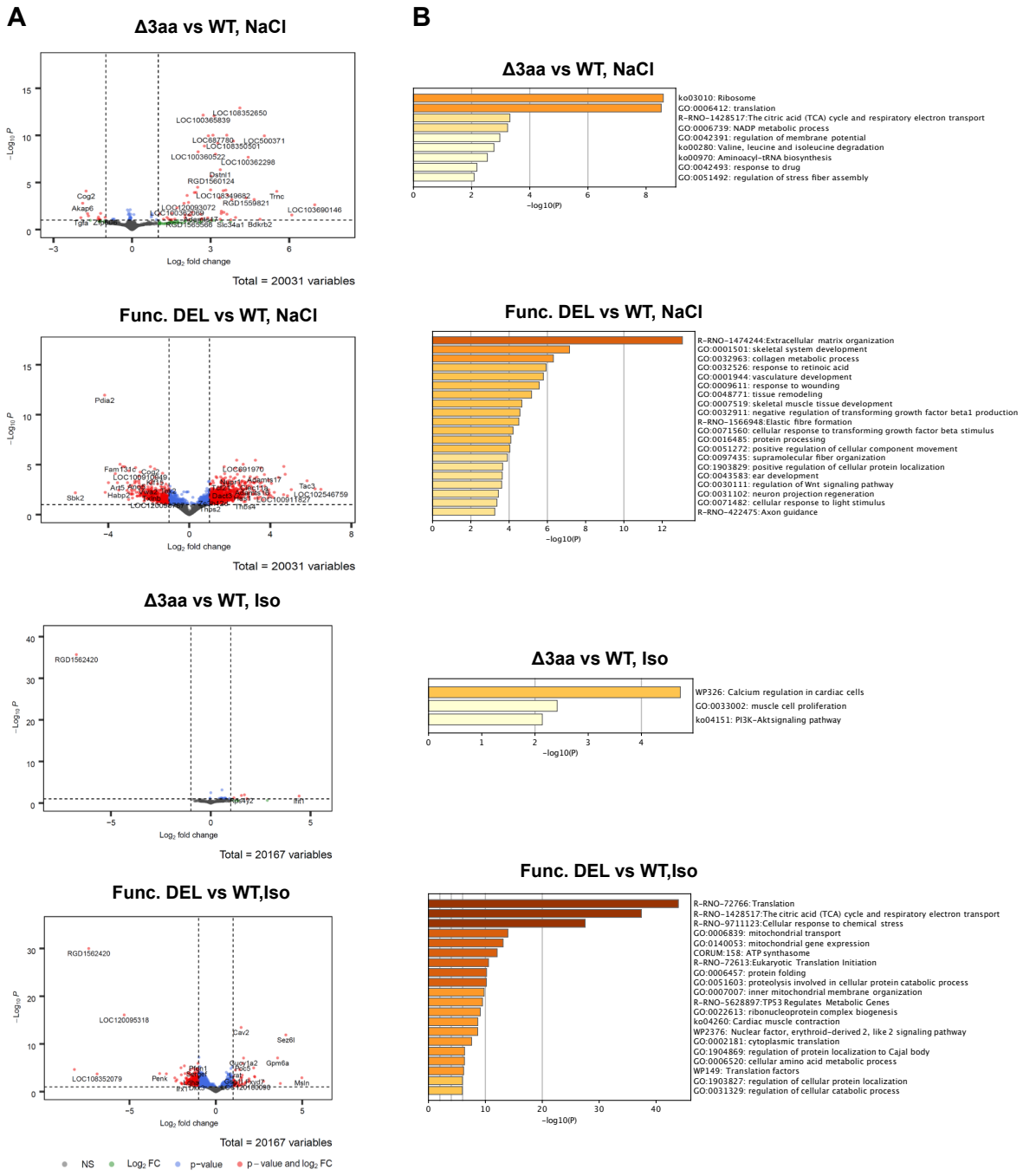

Figure 3.14. RNA sequencing of hearts from WT, PDE3A-Δ3aa rats, and Func DEL rats treated with NaCl or Isoproterenol. A. Volcano plots depict the distribution of genes that are differentially expressed. False discovery rate threshold is 0.1 and a log2 fold change threshold is 1. **B.** GO analysis of the RNA sequencing data. WT NaCl, n = 3; WT Iso, n = 2; PDE3A-Δ3aa NaCl, n = 2; PDE3A-Δ3aa Iso, n = 3; Func. DEL NaCl, n = 2; Func. DEL Iso, n = 2. RNA sequencing was performed in collaboration with the Genomics Technology Platform of

the MDC, Berlin. Data was analyzed by Daniele Yumi Sunaga-Franze, Tatiana Borodina, Brandon J McMurray, and Philipp G Maass (own figure, modified according to Ercu et al., 2022).

These data suggest that despite preexisting hypertension in combination with catecholamine-induced stress, the hearts of HTNB rats exhibited similar levels of cardiac damage compared to wild-type rats. In contrast, functional DEL rats appeared to be more susceptible to isoproterenol-induced cardiac damage than wild-type ones. Therefore, mutant PDE3A not only protects the heart from hypertension-induced cardiac damage but also helps to mitigate the development of cardiac damage caused by additional factors.

3.3.3 SERCA2A-SER663 is involved in PDE3A1-SERCA2A interaction

In cardiac myocytes, PDE3A1 is part of the protein complex responsible for Ca^{2+} reuptake from the cytosol to the SR during diastole (Ahmad et al., 2015). This complex is anchored to the SR via A-kinase anchoring protein 18δ (AKAP18δ) and comprises SERCA2A, phospholamban (PLN), PKA, PDE3A1, and Ca^{2+}/calmodulin-dependent protein kinase II (CaMKII) (Ahmad et al., 2015, Carlson et al., 2022).
PDE3A1 interacts with SERCA2A in the above-mentioned complex and inhibits SERCA2A activity (Skogestad et al., 2023). Peptide spot analysis performed in the group of Dr. Klussmann (MDC) suggested that Ser663 of SERCA2A may be involved in the PDE3A1-SERCA2A interaction. To test this hypothesis, HEK293 cells were co-transfected to transiently express HA-PDE3A1 and different FLAG-SERCA2A constructs: SERCA2A-WT, SERCA2A-S663A (to prevent phosphorylation), or SERCA2A-S663D (to mimic phosphorylation). No changes were observed in the interactions between the two proteins under resting conditions. SERCA2A-Ser663 is a potential site for mitogen-activated protein kinases (MAPK) phosphorylation, which can be induced by stimulation with EGF (Huang et al., 2016). Indeed, there was a tendency for increased interaction between PDE3A1 and SERCA2A-WT and a significant increase in the interaction between SERCA2A-S663D-PDE3A1 upon EGF stimulation, indicating that Ser663 plays a role in this interaction. However, the EGF-mediated increase of this interaction most likely involves not only Ser663.

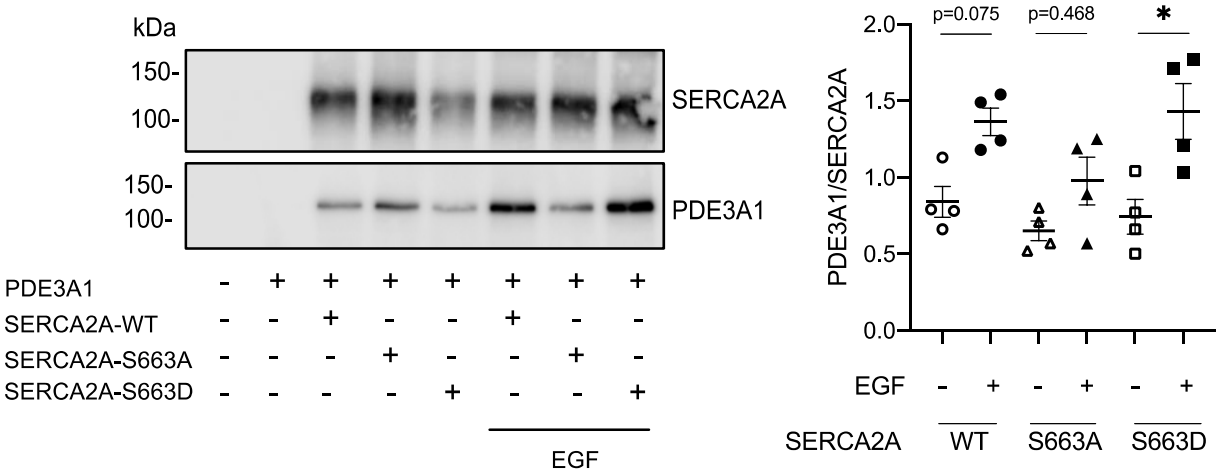

Figure 3.15. SERCA2A-Ser663 is involved in the interaction between SERCA2A and PDE3A1. HA-PDE3A1 and FLAG-SERCA2A were transiently expressed in HEK293 cells. FLAG-SERCA2A was immunoprecipitated from cell lysate and co-precipitation of HA-PDE3A1 was detected. n = 4. Statistical analysis: 2-way ANOVA with the Tukey multiple-comparisons test.; *P<0.05. Data shown are mean ± SEM.

4 Discussion

4.1 Renoprotection mediated by mutant PDE3A

In HTNB, hypertension arises from compromised resistance arteries and VSMCs exhibit an increased proliferation rate. This leads to an elevated media-to-lumen ratio and impaired vessel contractility (Ercu et al., 2020, Ercu et al., 2022). The aorta and third-order mesenteric arteries of PDE3A-Δ3aa rats displayed reduced relaxation in response to the cAMP-elevating agent forskolin (Ercu et al., 2020). Resistance arteries in the kidney and heart were also affected in HTNB rats and exhibited an increased media-to-lumen ratio compared to wild-types (Figure 3.2.B). However, in the kidneys of PDE3A-Δ3aa rats, the hyperplasia of renal arteries did not affect *Vasa recta* contractility (Figure 3.2.C). These observations suggest that hypertension may not always cause kidney damage and *vice versa*, and explain why lowering of the blood pressure alone may not be sufficient to prevent hypertension-induced kidney damage.

Serum and urine parameters in the examined HTNB patient and two HTNB rat models were unaffected (Figures 3.1, 3.3 E). This recapitulated the situation in HTNB mice with transgenic overexpression of the HTNB-causing PDE3A-T445N version in VSMCs (Ercu et al., 2020, Ercu et al., 2022, Maass et al., 2015) and in 6 affected persons in kindred with HTNB caused by PDE3A-T445N substitution (Schuster et al., 1996a, Schuster et al., 1996b, Maass et al., 2015). Single-cell RNA sequencing of mouse kidneys revealed the highest *PDE3A* expression in interstitial cells, moderate expression in podocytes and endothelial cells (mainly in descending *Vasa recta*), and lower expression in various tubular cells (Hinze et al., 2022). This expression pattern along with the consistent levels of electrolytes in both serum and urine in HTNB, suggests that the mutations of PDE3A did not have a noticeable impact on tubular cells or the filtration processes within the nephron.

4.2 Potential role of AREG in PDE3A-mediated renoprotection

Hypertension is typically associated with inflammation and fibrotic damage (Sholokh and Klussmann, 2021). The kidneys of HTNB rats demonstrated no detectable inflammation or tissue fibrosis (Figures 3.5, 3.6). Moreover, *Areg* expression was downregulated in the inner medulla of PDE3A-Δ3aa rats (Figure 3.9 B, C). AREG promotes injury-induced fibrosis (Kefaloyianni et al., 2019) and glomerulonephritis (Melderis et al., 2020)

by stimulating fibroblast proliferation and differentiation into myofibroblasts (Son et al., 2021). Patients with acute kidney injury or CKD displayed increased levels of AREG in urine and fibrosis markers in kidney biopsies (Kefaloyianni et al., 2016). In contrast, siRNA knockdown prevented the development of CKD in mice with unilateral ureteral obstruction (UUO) and if induced by an adenine diet (Son et al., 2021). Consistent with the normal serum levels of AREG in PDE3A-Δ3aa rats (Figure 3.9, C), ERK and Akt signalling downstream of the AREG receptor, EGFR, were unchanged in the kidney (Figure 3.10).

It is unknown how PDE3A controls *Areg* transcription and protein abundance. PGE_2 stimulation of the cAMP pathway activated *AREG* transcription in human colorectal carcinoma cells (Shao et al., 2003). In PDE3A-Δ3aa rat kidneys, *Areg* mRNA was upregulated and cAMP levels remained unchanged. Thus, *Areg* transcription appears to be independent of global cAMP elevation in the kidney. The downregulation of AREG protein expression could overcompensate for the upregulation of *Areg* mRNA.

4.3 Potential mechanisms for downregulation of mutant PDE3A

PDE3A protein expression levels were reduced in the kidneys of HTNB rats (Figure 3.4 A), which is consistent with the findings in the heart, aorta, and human induced pluripotent stem cell-derived cardiac myocytes (hiPSCs-CM) carrying HTNB-causing *PDE3A* mutations (Ercu et al., 2020, Ercu et al., 2022). In all these cases, PDE3A protein levels were lower in homozygous PDE3A-R862C rats than in heterozygous PDE3A-Δ3aa animals, suggesting that PDE3A, carrying HTNB-causing mutations, is more likely to be degraded than wild-type PDE3A.

In the kidney, RNA sequencing showed a significant decrease in *Pde3a* expression in the inner medulla and a tendency towards a decrease in the residual kidney of PDE3A-Δ3aa rats compared to wild-type. In the heart, a tendency towards an increase in *Pde3a* mRNA level in untreated PDE3A-Δ3aa animals, a decrease in the NaCl-treated PDE3A-Δ3aa animals, and a significant increase in isoproterenol-treated PDE3A-Δ3aa rats compared to corresponding wild-type animals were observed (the list with expression levels of all differentially expressed genes identified by RNA sequencing can be found at Sholokh et al. 2023, Supplementary Table S2).

The transcription of *PDE3A* is stimulated by splicing factor proline- and glutamine-rich protein (SFPQ) (Rhee et al., 2017) in HeLa cells; however, RNA sequencing

showed no change in the expression level of SFPQ in the kidneys and hearts. Ding et al. showed that in the heart, inducible cAMP early repressor (ICER) represses *PDE3A* gene transcription, whereas PDE3A downregulation causes upregulation of ICER level (Ding et al., 2005). RNA sequencing data showed an increase in *Icer* expression in the hearts of PDE3A-Δ3aa rats compared to wild-types (adjusted p-value was 0.0003 and log2 fold change was 1.025527). However, this still does not explain the tendency of increased *Pde3a* mRNA levels in the hearts of untreated PDE3A-Δ3aa rats.

4.4 Local effects of mutant PDE3A

Downregulation of mutant PDE3A protein levels possibly compensated for PDE3A hyperactivity and maintained global cAMP levels unchanged in the kidneys and hearts of HTNB rats (Figure 3.4. B). In contrast, cAMP levels in the second-order mesenteric arteries of PDE3A-Δ3aa rats remained significantly lower compared to wild-types (Ercu et al., 2020). This suggests that organs with preserved cAMP levels are protected, whereas those with affected levels are more prone to damage.

cAMP signalling is compartmentalized and occurs in defined cellular microdomains (Sholokh and Klussmann, 2021). Therefore, the effects of PDE3A hyperactivity may be local and distinguishable only at the levels of specific cell populations or intracellular microdomains. For example, renin synthesis and secretion, which rely on cAMP stimulation, occur exclusively in juxtaglomerular cells (Friis et al., 2002, Jackson, 2020). Therefore, the significant downregulation of renin expression in the kidneys of PDE3A-Δ3aa rats could be attributed to lower cAMP levels mediated by hyperactive PDE3A in the juxtaglomerular cells. In contrast, renin upregulation in functional DEL rats could be explained by the absence of active PDE3A and higher cAMP levels (Figure 3.3. B). Plasma renin levels also tend to decrease in PDE3A-Δ3aa rats and increase in functional DEL animals compared to the wild-type (Ercu et al., 2020). The reason behind the unaffected renin levels in PDE3A-R862C rats remains unknown. A potential explanation could be that more profound downregulation of PDE3A protein expression in PDE3A-R862C rats compensated for its hyperactivity in this specific case. Plasma renin levels were not affected in patients with PDE3A-T445N substitution (Schuster et al., 1996b); but were lower in PDE3A-G449S patient.

This was reminiscent of the situation in the hearts of PDE3A-Δ3aa rats. In that case, a decrease of PKA-mediated phosphorylation of PLN at Ser16 was observed, while the

level of cAMP in the hearts of PDE3A-Δ3aa animals remained unchanged (Ercu et al., 2022). In both cases, the decrease of renin expression and PLN phosphorylation can also be explained by locally lowered cAMP levels in the presence of hyperactive mutant PDE3A.

4.5 Cardioprotection mediated by mutant PDE3A

The morphology and function of the heart were not affected in the HTNB animals. However, hyperplasia of cardiac arteries was observed (Figures 3.11 and 3.12). This is in line with previous findings in the kidney (Sholokh et al., 2023) and suggests that mutant PDE3A protects different organs that are usually affected by hypertension. After two weeks of treatment with isoproterenol, the levels of cardiac damage in HNTB rats were comparable to or even lower than in wild-type rats, while animals with PDE3A knockout appeared to be more sensitive to catecholamine stress (Figures 3.13 and 3.14, and Ercu et al. 2022). Therefore, selective activation of PDE3A (which in the case of HTNB is caused by enzyme hyperactivity) seems to be more effective than PDE3A inhibition (induced by *Pde3a* knockout) upon cardiac damage.

Both HTNB patients and HTNB rats demonstrated improved cardiac contractility (Ercu et al., 2022). SERCA2A is one of the key proteins in the excitation-contraction coupling machinery of cardiac myocytes. Its activity is regulated, among the others, by interaction with PDE3A1 in the AKAP18δ-based protein complex on the SR of cardiac myocytes. Disruption of the PDE3A1-SERCA2A interaction increases SERCA2 activity, which has beneficial effects in mice with chronic heart failure (Skogestad et al., 2023). This is in line with the observation that mutant PDE3A1 demonstrated a decrease in the interaction with SERCA2 (Pallien, 2022). Stimulation with EGF promoted the interaction between PDE3A1 and SERCA2A. EGF plays a dual role in cardiovascular system function. It is required for normal development and functioning of the heart (Sanchez-Soria and Camenisch, 2010, Shraim et al., 2021) and can even protect against myocardial ischemia-reperfusion injury (Ma and Jin, 2019, Lee et al., 2020). However, chronic overactivation of EGFR leads to detrimental effects such as cardiac hypertrophy, fibrosis, and myocardial infarction (Mali et al., 2018, Peng et al., 2016, Shraim et al., 2021). The biological effects of EFG-mediated phosphorylation of SERCA2A-Ser663 still need to be identified.

4.6 Further directions for the study and clinical implication

At the current stage, the study showed that the kidneys and hearts of HTNB rats were protected from hypertension-induced damage under basal conditions, and the hearts of HTNB rats responded to the two-week catecholamine challenge in a similar manner to the wild-type animals. However, patients with CKD or heart failure require treatment while exhibiting progressive kidney and heart damage. To investigate whether the protective effect of *PDE3A* mutations will remain upon chronic renal or cardiac damage, CKD (5/6 nephrectomy, UUO, or adenine diet) and heart failure (thoracic aortic banding or myocardial infarction) models can be induced in HTNB rats.

The effects of *PDE3A* mutations become visible mostly at the level of a distinct cell population or macromolecular complexes. In the kidney, it is important to uncover the mechanisms of AREG-mediated renoprotection, namely, to understand the role of mutant PDE3A in the regulation of AREG expression and to identify AREG target receptors in the kidney. In the heart, investigation of local cAMP levels in close proximity to the SERCA2A-PDE3A-PLN complex and the effect of mutant PDE3A on the protein-protein interactions in the AKAP18δ complex are required and can be investigated using fluorescence resonance energy transfer (FRET) technology with sensors targeted to SR and immunoprecipitation approaches.

Finally, the mechanisms underlying PDE3A hyperactivity must be investigated. Ercu et al. showed that the mutant PDE3A-R862C demonstrated enhanced dimerization/self-assembly, potentially by the formation of an additional disulfide bond due to the introduction of an extra cysteine residue. Activation by dimerization has already been shown in PDE4 long isoforms (Omar et al., 2019).

One of the current treatment approaches for heart failure is the inhibition of PDE3. However, it is now only a short-term option due to its severe side effects, such as atrial arrhythmia, hypotension, and headache (Movsesian et al., 2018, Rogers et al., 2015, Tariq and Aronow, 2015). Mice with transgenic overexpression of PDE4B and PDE2 in cardiac myocytes, which led to a significant decrease in local cAMP levels, were protected from isoproterenol-induced cardiac damage (Karam et al., 2020) and exhibited improved contractility upon ischemic injury (Vettel et al., 2017). Omar et al. developed small-molecule activators of PDE4 long form, which prevented cyst formation in animal and human cell models of autosomal dominant polycystic kidney disease (Omar et al., 2019).

Altogether, these data suggest that selective PDE3A activation, rather than non-specific PDE3 inhibition, might be a better option for efficient treatment or even prevention of hypertension-induced diseases, such as heart failure and CKD.

5 Conclusions

This thesis provides evidence that mutations of *PDE3A*, despite causing hypertension, protect against hypertension-induced end-organ damage. Moreover, the hearts of HTNB rats did not acquire a higher sensitivity to cardiac stress, they responded to the catecholamine challenge in a manner similar to that of wild-type animals. This suggests that mutant PDE3A confers cardioprotection even upon a combination of additional cardiac stress and pre-existing hypertension.

The molecular mechanisms underlying PDE3A-mediated reno- and cardioprotection may be based on the regulation of the RAAS system activity and prevention of fibrosis through EGFR signalling in the kidney and modulation of Ca^{2+} cycling in cardiac myocytes in the heart.

Reference list

ABDULLAH MB, G. M., AYAD CE, ABDALLA EA 2014. Establishment of Reference Values for Renal Length and Volume for Normal Adult Sudanese using MRI Disc Summation Method. *Global Journal of Medical Research: D radiology, diagnostic imaging and instrumentation,* 14**,** 29-37.

AHMAD, F., SHEN, W., VANDEPUT, F., SZABO-FRESNAIS, N., KRALL, J., DEGERMAN, E., GOETZ, F., KLUSSMANN, E., MOVSESIAN, M. & MANGANIELLO, V. 2015. Regulation of sarcoplasmic reticulum Ca2+ ATPase 2 (SERCA2) activity by phosphodiesterase 3A (PDE3A) in human myocardium: phosphorylation-dependent interaction of PDE3A1 with SERCA2. *J Biol Chem,* 290**,** 6763-76.

AHMAD, T., MILLER, P. E., MCCULLOUGH, M., DESAI, N. R., RIELLO, R., PSOTKA, M., BOHM, M., ALLEN, L. A., TEERLINK, J. R., ROSANO, G. M. C. & LINDENFELD, J. 2019. Why has positive inotropy failed in chronic heart failure? Lessons from prior inotrope trials. *Eur J Heart Fail,* 21**,** 1064-1078.

AL-MAKKI, A., DIPETTE, D., WHELTON, P. K., MURAD, M. H., MUSTAFA, R. A., ACHARYA, S., BEHEIRY, H. M., CHAMPAGNE, B., CONNELL, K., COONEY, M. T., EZEIGWE, N., GAZIANO, T. A., GIDIO, A., LOPEZ-JARAMILLO, P., KHAN, U. I., KUMARAPELI, V., MORAN, A. E., SILWIMBA, M. M., RAYNER, B., SUKONTHASAN, A., YU, J., SARAFFZADEGAN, N., REDDY, K. S. & KHAN, T. 2022. Hypertension Pharmacological Treatment in Adults: A World Health Organization Guideline Executive Summary. *Hypertension,* 79**,** 293-301.

BAHRING, S., KANN, M., NEUENFELD, Y., GONG, M., CHITAYAT, D., TOKA, H. R., TOKA, O., PLESSIS, G., MAASS, P., RAUCH, A., AYDIN, A. & LUFT, F. C. 2008. Inversion region for hypertension and brachydactyly on chromosome 12p features multiple splicing and noncoding RNA. *Hypertension,* 51**,** 426-31.

BAILLIE, G. S., TEJEDA, G. S. & KELLY, M. P. 2019. Therapeutic targeting of 3',5'-cyclic nucleotide phosphodiesterases: inhibition and beyond. *Nat Rev Drug Discov,* 18**,** 770-796.

CARLSON, C. R., ARONSEN, J. M., BERGAN-DAHL, A., MOUTTY, M. C., LUNDE, M., LUNDE, P. K., JARSTADMARKEN, H., WANICHAWAN, P., PEREIRA, L., KOLSTAD, T. R. S., DALHUS, B., SUBRAMANIAN, H., HILLE, S., CHRISTENSEN, G., MULLER, O. J., NIKOLAEV, V., BERS, D. M., SJAASTAD, I., SHEN, X., LOUCH, W. E., KLUSSMANN, E. & SEJERSTED, O. M. 2022. AKAP18delta Anchors and Regulates CaMKII Activity at Phospholamban-SERCA2 and RYR. *Circ Res,* 130**,** 27-44.

CHARLES, C. & FERRIS, A. H. 2020. Chronic Kidney Disease. *Prim Care,* 47**,** 585-595.

CHOI, Y. H., EKHOLM, D., KRALL, J., AHMAD, F., DEGERMAN, E., MANGANIELLO, V. C. & MOVSESIAN, M. A. 2001. Identification of a novel isoform of the cyclic-nucleotide phosphodiesterase PDE3A expressed in vascular smooth-muscle myocytes. *Biochem J,* 353**,** 41-50.

DEGERMAN, E., BELFRAGE, P. & MANGANIELLO, V. C. 1997. Structure, localization, and regulation of cGMP-inhibited phosphodiesterase (PDE3). *J Biol Chem,* 272**,** 6823-6.

DI PALO, K. E. & BARONE, N. J. 2020. Hypertension and Heart Failure: Prevention, Targets, and Treatment. *Heart Fail Clin,* 16**,** 99-106.

DING, B., ABE, J., WEI, H., XU, H., CHE, W., AIZAWA, T., LIU, W., MOLINA, C. A., SADOSHIMA, J., BLAXALL, B. C., BERK, B. C. & YAN, C. 2005. A positive

feedback loop of phosphodiesterase 3 (PDE3) and inducible cAMP early repressor (ICER) leads to cardiomyocyte apoptosis. *Proc Natl Acad Sci U S A,* 102**,** 14771-6.

DISEASE, G. B. D., INJURY, I. & PREVALENCE, C. 2017. Global, regional, and national incidence, prevalence, and years lived with disability for 328 diseases and injuries for 195 countries, 1990-2016: a systematic analysis for the Global Burden of Disease Study 2016. *Lancet,* 390**,** 1211-1259.

EDWARDS, A. & KURTCUOGLU, V. 2022. Renal blood flow and oxygenation. *Pflugers Arch,* 474**,** 759-770.

ERCU, M. & KLUSSMANN, E. 2018. Roles of A-Kinase Anchoring Proteins and Phosphodiesterases in the Cardiovascular System. *J Cardiovasc Dev Dis,* 5.

ERCU, M., MARKO, L., SCHACHTERLE, C., TSVETKOV, D., CUI, Y., MAGHSODI, S., BARTOLOMAEUS, T. U. P., MAASS, P. G., ZUHLKE, K., GREGERSEN, N., HUBNER, N., HODGE, R., MUHL, A., POHL, B., ILLAS, R. M., GEELHAAR, A., WALTER, S., NAPIECZYNSKA, H., SCHELENZ, S., TAUBE, M., HEUSER, A., ANISTAN, Y. M., QADRI, F., TODIRAS, M., PLEHM, R., POPOVA, E., LANGANKI, R., EICHHORST, J., LEHMANN, M., WIESNER, B., RUSSWURM, M., FORSLUND, S. K., KAMER, I., MULLER, D. N., GOLLASCH, M., AYDIN, A., BAHRING, S., BADER, M., LUFT, F. C. & KLUSSMANN, E. 2020. Phosphodiesterase 3A and Arterial Hypertension. *Circulation,* 142**,** 133-149.

ERCU, M., MUCKE, M. B., PALLIEN, T., MARKO, L., SHOLOKH, A., SCHACHTERLE, C., AYDIN, A., KIDD, A., WALTER, S., ESMATI, Y., MCMURRAY, B. J., LATO, D. F., YUMI SUNAGA-FRANZE, D., DIERKS, P. H., FLORES, B. I. M., WALKER-GRAY, R., GONG, M., MERTICARIU, C., ZUHLKE, K., RUSSWURM, M., LIU, T., BATOLOMAEUS, T. U. P., PAUTZ, S., SCHELENZ, S., TAUBE, M., NAPIECZYNSKA, H., HEUSER, A., EICHHORST, J., LEHMANN, M., MILLER, D. C., DIECKE, S., QADRI, F., POPOVA, E., LANGANKI, R., MOVSESIAN, M. A., HERBERG, F. W., FORSLUND, S. K., MULLER, D. N., BORODINA, T., MAASS, P. G., BAHRING, S., HUBNER, N., BADER, M. & KLUSSMANN, E. 2022. Mutant Phosphodiesterase 3A Protects From Hypertension-Induced Cardiac Damage. *Circulation,* 146**,** 1758-1778.

ERCU, M., WALTER, S. & KLUSSMANN, E. 2023. Mutations in Phosphodiesterase 3A (PDE3A) Cause Hypertension Without Cardiac Damage. *Hypertension,* 80**,** 1171-1179.

FOLKOW, B., GOTHBERG, G., LUNDIN, S. & RICKSTEN, S. E. 1977. Structural "resetting" of the renal vascular bed in spontaneously hypertensive rats (SHR). *Acta Physiol Scand,* 100**,** 270-2.

FRIIS, U. G., JENSEN, B. L., SETHI, S., ANDREASEN, D., HANSEN, P. B. & SKOTT, O. 2002. Control of renin secretion from rat juxtaglomerular cells by cAMP-specific phosphodiesterases. *Circ Res,* 90**,** 996-1003.

GARGIULO, R., SUHAIL, F. & LERMA, E. V. 2015. Hypertension and chronic kidney disease. *Dis Mon,* 61**,** 387-95.

GONZALEZ, A., RAVASSA, S., LOPEZ, B., MORENO, M. U., BEAUMONT, J., SAN JOSE, G., QUEREJETA, R., BAYES-GENIS, A. & DIEZ, J. 2018. Myocardial Remodeling in Hypertension. *Hypertension,* 72**,** 549-558.

HARSKAMP, L. R., GANSEVOORT, R. T., VAN GOOR, H. & MEIJER, E. 2016. The epidermal growth factor receptor pathway in chronic kidney diseases. *Nat Rev Nephrol,* 12**,** 496-506.

HINZE, C., KOCKS, C., LEIZ, J., KARAISKOS, N., BOLTENGAGEN, A., CAO, S., SKOPNIK, C. M., KLOCKE, J., HARDENBERG, J. H., STOCKMANN, H.,

GOTTHARDT, I., OBERMAYER, B., HAGHVERDI, L., WYLER, E., LANDTHALER, M., BACHMANN, S., HOCKE, A. C., CORMAN, V., BUSCH, J., SCHNEIDER, W., HIMMERKUS, N., BLEICH, M., ECKARDT, K. U., ENGHARD, P., RAJEWSKY, N. & SCHMIDT-OTT, K. M. 2022. Single-cell transcriptomics reveals common epithelial response patterns in human acute kidney injury. *Genome Med,* 14**,** 103.

HUANG, H., HAAR PETERSEN, M., IBANEZ-VEA, M., LASSEN, P. S., LARSEN, M. R. & PALMISANO, G. 2016. Simultaneous Enrichment of Cysteine-containing Peptides and Phosphopeptides Using a Cysteine-specific Phosphonate Adaptable Tag (CysPAT) in Combination with titanium dioxide (TiO2) Chromatography. *Mol Cell Proteomics,* 15**,** 3282-3296.

JACKSON, P. K. 2020. cAMP Signaling in Nanodomains. *Cell,* 182**,** 1379-1381.

KARAM, S., MARGARIA, J. P., BOURCIER, A., MIKA, D., VARIN, A., BEDIOUNE, I., LINDNER, M., BOUADJEL, K., DESSILLONS, M., GAUDIN, F., LEFEBVRE, F., MATEO, P., LECHENE, P., GOMEZ, S., DOMERGUE, V., ROBERT, P., COQUARD, C., ALGALARRONDO, V., SAMUEL, J. L., MICHEL, J. B., CHARPENTIER, F., GHIGO, A., HIRSCH, E., FISCHMEISTER, R., LEROY, J. & VANDECASTEELE, G. 2020. Cardiac Overexpression of PDE4B Blunts beta-Adrenergic Response and Maladaptive Remodeling in Heart Failure. *Circulation,* 142**,** 161-174.

KEFALOYIANNI, E., KEERTHI RAJA, M. R., SCHUMACHER, J., MUTHU, M. L., KRISHNADOSS, V., WAIKAR, S. S. & HERRLICH, A. 2019. Proximal Tubule-Derived Amphiregulin Amplifies and Integrates Profibrotic EGF Receptor Signals in Kidney Fibrosis. *J Am Soc Nephrol,* 30**,** 2370-2383.

KEFALOYIANNI, E., MUTHU, M. L., KAEPPLER, J., SUN, X., SABBISETTI, V., CHALARIS, A., ROSE-JOHN, S., WONG, E., SAGI, I., WAIKAR, S. S., RENNKE, H., HUMPHREYS, B. D., BONVENTRE, J. V. & HERRLICH, A. 2016. ADAM17 substrate release in proximal tubule drives kidney fibrosis. *JCI Insight,* 1.

KHERA, R., LU, Y., LU, J., SAXENA, A., NASIR, K., JIANG, L. & KRUMHOLZ, H. M. 2018. Impact of 2017 ACC/AHA guidelines on prevalence of hypertension and eligibility for antihypertensive treatment in United States and China: nationally representative cross sectional study. *BMJ,* 362**,** k2357.

KOVESDY, C. P. 2022. Epidemiology of chronic kidney disease: an update 2022. *Kidney Int Suppl (2011),* 12**,** 7-11.

LEE, J. W., KOEPPEN, M., SEO, S. W., BOWSER, J. L., YUAN, X., LI, J., SIBILIA, M., AMBARDEKAR, A. V., ZHANG, X., ECKLE, T., YOO, S. H. & ELTZSCHIG, H. K. 2020. Transcription-independent Induction of ERBB1 through Hypoxia-inducible Factor 2A Provides Cardioprotection during Ischemia and Reperfusion. *Anesthesiology,* 132**,** 763-780.

LEENEN, F. H., WHITE, R. & YUAN, B. 2001. Isoproterenol-induced cardiac hypertrophy: role of circulatory versus cardiac renin-angiotensin system. *Am J Physiol Heart Circ Physiol,* 281**,** H2410-6.

MA, J. & JIN, G. 2019. Epidermal growth factor protects against myocardial ischaemia reperfusion injury through activating Nrf2 signalling pathway. *Free Radic Res,* 53**,** 313-323.

MAASS, P. G., AYDIN, A., LUFT, F. C., SCHACHTERLE, C., WEISE, A., STRICKER, S., LINDSCHAU, C., VAEGLER, M., QADRI, F., TOKA, H. R., SCHULZ, H., KRAWITZ, P. M., PARKHOMCHUK, D., HECHT, J., HOLLFINGER, I., WEFELD-NEUENFELD, Y., BARTELS-KLEIN, E., MUHL, A., KANN, M., SCHUSTER, H.,

CHITAYAT, D., BIALER, M. G., WIENKER, T. F., OTT, J., RITTSCHER, K., LIEHR, T., JORDAN, J., PLESSIS, G., TANK, J., MAI, K., NARAGHI, R., HODGE, R., HOPP, M., HATTENBACH, L. O., BUSJAHN, A., RAUCH, A., VANDEPUT, F., GONG, M., RUSCHENDORF, F., HUBNER, N., HALLER, H., MUNDLOS, S., BILGINTURAN, N., MOVSESIAN, M. A., KLUSSMANN, E., TOKA, O. & BAHRING, S. 2015. PDE3A mutations cause autosomal dominant hypertension with brachydactyly. *Nat Genet,* 47**,** 647-53.

MALI, V., HADDOX, S., HORNERSMITH, C., MATROUGUI, K. & BELMADANI, S. 2018. Essential role for EGFR tyrosine kinase and ER stress in myocardial infarction in type 2 diabetes. *Pflugers Arch,* 470**,** 471-480.

MELDERIS, S., HAGENSTEIN, J., WARKOTSCH, M. T., DANG, J., HERRNSTADT, G. R., NIEHUS, C. B., NEUMANN, K., PANZER, U., BERASAIN, C., AVILA, M. A., THARAUX, P. L., TIEGS, G. & STEINMETZ, O. M. 2020. Amphiregulin Aggravates Glomerulonephritis via Recruitment and Activation of Myeloid Cells. *J Am Soc Nephrol,* 31**,** 1996-2012.

MENNUNI, S., RUBATTU, S., PIERELLI, G., TOCCI, G., FOFI, C. & VOLPE, M. 2014. Hypertension and kidneys: unraveling complex molecular mechanisms underlying hypertensive renal damage. *J Hum Hypertens,* 28**,** 74-9.

MESSERLI, F. H., WILLIAMS, B. & RITZ, E. 2007. Essential hypertension. *Lancet,* 370**,** 591-603.

MO, X., LU, P. & YANG, X. 2023. Efficacy of sacubitril-valsartan and SGLT2 inhibitors in heart failure with reduced ejection fraction: A systematic review and meta-analysis. *Clin Cardiol*.

MOVSESIAN, M., AHMAD, F. & HIRSCH, E. 2018. Functions of PDE3 Isoforms in Cardiac Muscle. *J Cardiovasc Dev Dis,* 5.

OMAR, F., FINDLAY, J. E., CARFRAY, G., ALLCOCK, R. W., JIANG, Z., MOORE, C., MUIR, A. L., LANNOY, M., FERTIG, B. A., MAI, D., DAY, J. P., BOLGER, G., BAILLIE, G. S., SCHWIEBERT, E., KLUSSMANN, E., PYNE, N. J., ONG, A. C. M., BOWERS, K., ADAM, J. M., ADAMS, D. R., HOUSLAY, M. D. & HENDERSON, D. J. P. 2019. Small-molecule allosteric activators of PDE4 long form cyclic AMP phosphodiesterases. *Proc Natl Acad Sci U S A,* 116**,** 13320-13329.

OZAKCA, I., ARIOGLU-INAN, E., ESFAHANI, H., ALTAN, V. M., BALLIGAND, J. L., KAYKI-MUTLU, G. & OZCELIKAY, A. T. 2013. Nebivolol prevents desensitization of beta-adrenoceptor signaling and induction of cardiac hypertrophy in response to isoprenaline beyond beta1-adrenoceptor blockage. *Am J Physiol Heart Circ Physiol,* 304**,** H1267-76.

PADMANABHAN, S., CAULFIELD, M. & DOMINICZAK, A. F. 2015. Genetic and molecular aspects of hypertension. *Circ Res,* 116**,** 937-59.

PALLIEN, T. 2022. *Identification of a direct interaction of protein kinase A with the L-type Ca^{2+} channel and characterization of effects of PDE3A mutations on cardiac myocytes.* Dr. rer. nat., Freie Universität Berlin.

PAVENSTADT, H., KRIZ, W. & KRETZLER, M. 2003. Cell biology of the glomerular podocyte. *Physiol Rev,* 83**,** 253-307.

PENG, K., TIAN, X., QIAN, Y., SKIBBA, M., ZOU, C., LIU, Z., WANG, J., XU, Z., LI, X. & LIANG, G. 2016. Novel EGFR inhibitors attenuate cardiac hypertrophy induced by angiotensin II. *J Cell Mol Med,* 20**,** 482-94.

RENKEMA, K. Y., WESTERMANN, J. M., NIEVELSTEIN, R. A. J., LO, A. N. S. M., VAN DER ZWAAG, B., MANSHANDE, M. E. & VAN HAELST, M. M. 2018. PDE3A

gene screening improves diagnostics for patients with Bilginturan syndrome (hypertension and brachydactyly syndrome). *Hypertens Res,* 41**,** 981-988.

RHEE, D. K., HOCKMAN, S. C., CHOI, S. K., KIM, Y. E., PARK, C., MANGANIELLO, V. C. & KIM, K. K. 2017. SFPQ, a multifunctional nuclear protein, regulates the transcription of PDE3A. *Biosci Rep,* 37.

ROGERS, K. C., OLIPHANT, C. S. & FINKS, S. W. 2015. Clinical efficacy and safety of cilostazol: a critical review of the literature. *Drugs,* 75**,** 377-95.

SANCHEZ-SORIA, P. & CAMENISCH, T. D. 2010. ErbB signaling in cardiac development and disease. *Semin Cell Dev Biol,* 21**,** 929-35.

SCHIRONE, L., FORTE, M., PALMERIO, S., YEE, D., NOCELLA, C., ANGELINI, F., PAGANO, F., SCHIAVON, S., BORDIN, A., CARRIZZO, A., VECCHIONE, C., VALENTI, V., CHIMENTI, I., DE FALCO, E., SCIARRETTA, S. & FRATI, G. 2017. A Review of the Molecular Mechanisms Underlying the Development and Progression of Cardiac Remodeling. *Oxid Med Cell Longev,* 2017**,** 3920195.

SCHUMACHER, A., ROOKMAAKER, M. B., JOLES, J. A., KRAMANN, R., NGUYEN, T. Q., VAN GRIENSVEN, M. & LAPOINTE, V. L. S. 2021. Defining the variety of cell types in developing and adult human kidneys by single-cell RNA sequencing. *NPJ Regen Med,* 6**,** 45.

SCHUSTER, H., WIENKER, T. E., BAHRING, S., BILGINTURAN, N., TOKA, H. R., NEITZEL, H., JESCHKE, E., TOKA, O., GILBERT, D., LOWE, A., OTT, J., HALLER, H. & LUFT, F. C. 1996a. Severe autosomal dominant hypertension and brachydactyly in a unique Turkish kindred maps to human chromosome 12. *Nat Genet,* 13**,** 98-100.

SCHUSTER, H., WIENKER, T. F., TOKA, H. R., BAHRING, S., JESCHKE, E., TOKA, O., BUSJAHN, A., HEMPEL, A., TAHLHAMMER, C., OELKERS, W., KUNZE, J., BILGINTURAN, N., HALLER, H. & LUFT, F. C. 1996b. Autosomal dominant hypertension and brachydactyly in a Turkish kindred resembles essential hypertension. *Hypertension,* 28**,** 1085-92.

SHAO, J., LEE, S. B., GUO, H., EVERS, B. M. & SHENG, H. 2003. Prostaglandin E2 stimulates the growth of colon cancer cells via induction of amphiregulin. *Cancer Res,* 63**,** 5218-23.

SHOLOKH, A. & KLUSSMANN, E. 2021. Local cyclic adenosine monophosphate signalling cascades-Roles and targets in chronic kidney disease. *Acta Physiol (Oxf),* 232**,** e13641.

SHOLOKH, A., WALTER, S., MARKO, L., MCMURRAY, B. J., SUNAGA-FRANZE, D. Y., XU, M., ZUHLKE, K., RUSSWURM, M., BARTOLOMAEUS, T. U. P., LANGANKI, R., QADRI, F., HEUSER, A., PATZAK, A., FORSLUND, S. K., BAHRING, S., BORODINA, T., PERSSON, P. B., MAASS, P. G., BADER, M. & KLUSSMANN, E. 2023. Mutant phosphodiesterase 3A protects the kidney from hypertension-induced damage. *Kidney Int*.

SHRAIM, B. A., MOURSI, M. O., BENTER, I. F., HABIB, A. M. & AKHTAR, S. 2021. The Role of Epidermal Growth Factor Receptor Family of Receptor Tyrosine Kinases in Mediating Diabetes-Induced Cardiovascular Complications. *Front Pharmacol,* 12**,** 701390.

SKOGESTAD, J., ALBERT, I., HOUGEN, K., LOTHE, G. B., LUNDE, M., EKEN, O. S., VERAS, I., HUYNH, N. T. T., BORSTAD, M., MARSHALL, S., SHEN, X., LOUCH, W. E., ROBINSON, E. L., CLEVELAND, J. C., JR., AMBARDEKAR, A. V., SCHWISOW, J. A., JONAS, E., CALEJO, A. I., MORTH, J. P., TASKEN, K., MELLEBY, A. O., LUNDE, P. K., SJAASTAD, I., CARLSON, C. R. & ARONSEN, J. M. 2023. Disruption of Phosphodiesterase 3A Binding to SERCA2 Increases

SERCA2 Activity and Reduces Mortality in Mice With Chronic Heart Failure. *Circulation,* 147**,** 1221-1236.

SON, S. S., HWANG, S., PARK, J. H., KO, Y., YUN, S. I., LEE, J. H., SON, B., KIM, T. R., PARK, H. O. & LEE, E. Y. 2021. In vivo silencing of amphiregulin by a novel effective Self-Assembled-Micelle inhibitory RNA ameliorates renal fibrosis via inhibition of EGFR signals. *Sci Rep,* 11**,** 2191.

SUBRAMANIAM, G., SCHLEICHER, K., KOVANICH, D., ZERIO, A., FOLKMANAITE, M., CHAO, Y. C., SURDO, N. C., KOSCHINSKI, A., HU, J., SCHOLTEN, A., HECK, A. J. R., ERCU, M., SHOLOKH, A., PARK, K. C., KLUSSMANN, E., MERAVIGLIA, V., BELLIN, M., ZANIVAN, S., HESTER, S., MOHAMMED, S. & ZACCOLO, M. 2023. Integrated Proteomics Unveils Nuclear PDE3A2 as a Regulator of Cardiac Myocyte Hypertrophy. *Circ Res,* 132**,** 828-848.

TARIQ, S. & ARONOW, W. S. 2015. Use of Inotropic Agents in Treatment of Systolic Heart Failure. *Int J Mol Sci,* 16**,** 29060-8.

TOKA, O., TANK, J., SCHACHTERLE, C., AYDIN, A., MAASS, P. G., ELITOK, S., BARTELS-KLEIN, E., HOLLFINGER, I., LINDSCHAU, C., MAI, K., BOSCHMANN, M., RAHN, G., MOVSESIAN, M. A., MULLER, T., DOESCHER, A., GNOTH, S., MUHL, A., TOKA, H. R., WEFELD-NEUENFELD, Y., UTZ, W., TOPPER, A., JORDAN, J., SCHULZ-MENGER, J., KLUSSMANN, E., BAHRING, S. & LUFT, F. C. 2015. Clinical effects of phosphodiesterase 3A mutations in inherited hypertension with brachydactyly. *Hypertension,* 66**,** 800-8.

TSAO, C. W., ADAY, A. W., ALMARZOOQ, Z. I., ALONSO, A., BEATON, A. Z., BITTENCOURT, M. S., BOEHME, A. K., BUXTON, A. E., CARSON, A. P., COMMODORE-MENSAH, Y., ELKIND, M. S. V., EVENSON, K. R., EZE-NLIAM, C., FERGUSON, J. F., GENEROSO, G., HO, J. E., KALANI, R., KHAN, S. S., KISSELA, B. M., KNUTSON, K. L., LEVINE, D. A., LEWIS, T. T., LIU, J., LOOP, M. S., MA, J., MUSSOLINO, M. E., NAVANEETHAN, S. D., PERAK, A. M., POUDEL, R., REZK-HANNA, M., ROTH, G. A., SCHROEDER, E. B., SHAH, S. H., THACKER, E. L., VANWAGNER, L. B., VIRANI, S. S., VOECKS, J. H., WANG, N. Y., YAFFE, K. & MARTIN, S. S. 2022. Heart Disease and Stroke Statistics-2022 Update: A Report From the American Heart Association. *Circulation,* 145**,** e153-e639.

VETTEL, C., LINDNER, M., DEWENTER, M., LORENZ, K., SCHANBACHER, C., RIEDEL, M., LAMMLE, S., MEINECKE, S., MASON, F. E., SOSSALLA, S., GEERTS, A., HOFFMANN, M., WUNDER, F., BRUNNER, F. J., WIELAND, T., MEHEL, H., KARAM, S., LECHENE, P., LEROY, J., VANDECASTEELE, G., WAGNER, M., FISCHMEISTER, R. & EL-ARMOUCHE, A. 2017. Phosphodiesterase 2 Protects Against Catecholamine-Induced Arrhythmia and Preserves Contractile Function After Myocardial Infarction. *Circ Res,* 120**,** 120-132.

WEBSTER, A. C., NAGLER, E. V., MORTON, R. L. & MASSON, P. 2017. Chronic Kidney Disease. *Lancet,* 389**,** 1238-1252.

Statutory Declaration

Statutory Declaration

"I, Anastasiia Sholokh, by personally signing this document in lieu of an oath, hereby affirm that I prepared the submitted dissertation on the topic Mutant phosphodiesterase 3A protects from hypertension- induced end-organ damage / Mutierte Phosphodiesterase 3A schützt vor Hypertonie-induzierten Endorganschäden, independently and without the support of third parties, and that I used no other sources and aids than those stated.

All parts which are based on the publications or presentations of other authors, either in letter or in spirit, are specified as such in accordance with the citing guidelines. The sections on methodology (in particular regarding practical work, laboratory regulations, statistical processing) and results (in particular regarding figures, charts and tables) are exclusively my responsibility.

Furthermore, I declare that I have correctly marked all of the data, the analyses, and the conclusions generated from data obtained in collaboration with other persons, and that I have correctly marked my own contribution and the contributions of other persons (cf. declaration of contribution). I have correctly marked all texts or parts of texts that were generated in collaboration with other persons.

My contributions to any publications to this dissertation correspond to those stated in the below joint declaration made together with the supervisor. All publications created within the scope of the dissertation comply with the guidelines of the ICMJE (International Committee of Medical Journal Editors; http://www.icmje.org) on authorship. In addition, I declare that I shall comply with the regulations of Charité – Universitätsmedizin Berlin on ensuring good scientific practice.

I declare that I have not yet submitted this dissertation in identical or similar form to another Faculty.

The significance of this statutory declaration and the consequences of a false statutory declaration under criminal law (Sections 156, 161 of the German Criminal Code) are known to me."

Declaration of my own contribution to the publications

Anastasiia Sholokh contributed the following to the below listed publications:

Publication 1:

Sholokh, A., Walter, S., Marko, L., McMurray, B. J., Sunaga-Franze, D. Y., Xu, M., . . . Klussmann, E. (2023). Mutant phosphodiesterase 3A protects the kidney from hypertension-induced damage. Kidney Int. doi:10.1016/j.kint.2023.04.026]

Contribution:

Anastasiia planned and performed the experiments, analyzed the data and took care of the visual representation of the data presented in Figure 1 (b-e), Figure 2 (c-g), Supplementary Figure S2 (a, b, d), Supplementary Figure S3 (c-h), Supplementary Figure S4 (b-e) and Supplementary Figure S5.

Anastasiia prepared the samples, took care of analysis and the visual representation of data presented in Figure 2 (a-b), Supplementary Figure S3 (a-b), Supplementary Figure S4 (a) and Supplementary Table S2. Anastasiia analyzed and took care of the visual representation of the data presented in Figure 1 (a), Supplementary Figure S1, Supplementary Figure S2 (c), Supplementary Table S1.

Anastasiia has prepared the manuscript together with Enno Klussmann.

Publication 2:

Ercu, M., Mucke, M. B., Pallien, T., Marko, L., **Sholokh, A.,** Schachterle, C., . . . Klussmann, E. (2022). Mutant Phosphodiesterase 3A Protects From Hypertension-Induced Cardiac Damage. Circulation, 146(23), 1758-1778. doi:10.1161/CIRCULATIONAHA.122.060210

Contribution:

Anastasiia planned and performed the experiments, analyzed the data and took care of the visual representation of the data presented in Figure 2 (B), Figure 3 (B) and Supplementary Figure 2S (A, G).

Anastasiia was involved in preparation of the samples for the experiments represented in Figure 7; took care of analysis and the visual representation of data presented in Supplementary Figure S4 (a). Anastasiia prepared Figure 1 (A).

Publication 3:

Subramaniam, G., Schleicher, K., Kovanich, D., Zerio, A., Folkmanaite, M., Chao, Y. C., . . . **Sholokh, A.**,. . . . Zaccolo, M. (2023). Integrated Proteomics Unveils Nuclear PDE3A2 as a Regulator of Cardiac Myocyte Hypertrophy. Circ Res, 132(7), 828-848. doi:10.1161/CIRCRESAHA.122.321448

Contribution:

Anastasiia planned and performed the experiments, analyzed the data and took care of the visual representation of data presented in Supplementary Figure 15.

Copies of the publications

https://doi.org/10.1016/j.kint.2023.04.026

https://doi.org/10.1161/CIRCULATIONAHA.122.060210

Circulation Research

ORIGINAL RESEARCH

Integrated Proteomics Unveils Nuclear PDE3A2 as a Regulator of Cardiac Myocyte Hypertrophy

Gunasekaran Subramaniam,* Katharina Schleicher,* Duangnapa Kovanich,* Anna Zerio, Milda Folkmanaite, Ying-Chi Chao, Nicoletta C. Surdo, Andreas Koschinski, Jianshu Hu, Arjen Scholten, Albert J.R. Heck, Maria Ercu, Anastasiia Sholokh, Kyung Chan Park, Enno Klussmann, Viviana Meraviglia, Milena Bellin, Sara Zanivan, Svenja Hester, Shabaz Mohammed, Manuela Zaccolo

BACKGROUND: Signaling by cAMP is organized in multiple distinct subcellular nanodomains regulated by cAMP-hydrolyzing PDEs (phosphodiesterases). Cardiac β-adrenergic signaling has served as the prototypical system to elucidate cAMP compartmentalization. Although studies in cardiac myocytes have provided an understanding of the location and properties of a handful of cAMP subcellular compartments, an overall view of the cellular landscape of cAMP nanodomains is missing.

METHODS: Here, we combined an integrated phosphoproteomics approach that takes advantage of the unique role that individual PDEs play in the control of local cAMP, with network analysis to identify previously unrecognized cAMP nanodomains associated with β-adrenergic stimulation. We then validated the composition and function of one of these nanodomains using biochemical, pharmacological, and genetic approaches and cardiac myocytes from both rodents and humans.

RESULTS: We demonstrate the validity of the integrated phosphoproteomic strategy to pinpoint the location and provide critical cues to determine the function of previously unknown cAMP nanodomains. We characterize in detail one such compartment and demonstrate that the PDE3A2 isoform operates in a nuclear nanodomain that involves SMAD4 (SMAD family member 4) and HDAC-1 (histone deacetylase 1). Inhibition of PDE3 results in increased HDAC-1 phosphorylation, leading to inhibition of its deacetylase activity, derepression of gene transcription, and cardiac myocyte hypertrophic growth.

CONCLUSIONS: We developed a strategy for detailed mapping of subcellular PDE-specific cAMP nanodomains. Our findings reveal a mechanism that explains the negative long-term clinical outcome observed in patients with heart failure treated with PDE3 inhibitors.

GRAPHIC ABSTRACT: A graphic abstract is available for this article.

Key Words: adrenergic agents ■ hypertrophy ■ phosphoric diester hydrolases ■ protein isoforms ■ rodentia

In This Issue, see p 791 | Meet the First Author, see p 792

The intracellular second messenger 3′, 5′-cAMP regulates multiple cellular functions in all organ systems. In the heart, cAMP mediates the cardiac flight-or-fight response to sympathetic activation of β-ARs (β-adrenergic receptors), leading to modulation of rate and strength of contraction. cAMP is synthesized by adenylyl cyclases and is degraded by cyclic nucleotide-hydrolyzing PDEs (phosphodiesterases). PDEs are a superfamily of enzymes that includes 11 gene families (PDE1–11) and >100 protein isoforms, each presenting with a unique combination of substrate specificity, kinetics, regulatory mechanisms, expression profile, and

Correspondence to: Manuela Zaccolo, MD, PhD, Department of Physiology Anatomy and Genetics, University of Oxford, Parks Rd, OX1 3PT Oxford, United Kingdom. Email manuela.zaccolo@dpag.ox.ac.uk
*G. Subramaniam, K. Schleicher, and D. Kovanich contributed equally.
Supplemental Material is available at https://www.ahajournals.org/doi/suppl/10.1161/CIRCRESAHA.122.321448.
For Sources of Funding and Disclosures, see page 846.
© 2023 The Authors. *Circulation Research* is published on behalf of the American Heart Association, Inc., by Wolters Kluwer Health, Inc. This is an open access article under the terms of the Creative Commons Attribution License, which permits use, distribution, and reproduction in any medium, provided that the original work is properly cited.
Circulation Research is available at www.ahajournals.org/journal/res

Novelty and Significance

What Is Known?

- cAMP signaling operates through multiple distinct nanodomains that control different functional effects.
- Phosphodiesterases play a key role in determining which cAMP nanodomain is operative.
- Disruption of cAMP compartmentalization is associated with cardiac disease.
- Only a small number of obvious cAMP nanodomains have been characterized in cardiac myocytes.

What New Information Does This Article Contribute?

- We have identified multiple novel, nonobvious cAMP nanodomains under the selective regulation of PDE2A2 (phosphodiesterase2A2), PDE3A1, and PDE3A2.
- We have characterized a nuclear domain that involves PDE3A2, Smad4 (SMAD family member 4), and HDAC-1 (histone deacetylase 1) that controls cardiac myocyte hypertrophy via PKA (protein kinase A)-dependent regulation of HDAC-1 activity.

The compartmentalized nature of cAMP signaling is now well established; however, the full picture of how this system is organized within the cardiac myocyte is missing and only a handful of obvious cAMP nanodomains have been characterized so far. Here, using an integrated phosphointeractomics approach, we discovered multiple novel and nonobvious cAMP nanodomains that are under the regulation of specific phosphodiesterase isoforms. When applied at scale, this method has the potential to uncover the full landscape of subcellular cAMP compartments. We validated, both in rat and human cardiac myocytes, one of the newly identified nanodomains that is located in the nucleus. We demonstrated that, by degrading cAMP at this location, PDE3A2 protects the cardiac myocyte from hypertrophic growth, whereas PDE3A2 inhibition triggers hypertrophy. This cAMP nanodomain can explain the increased mortality observed when PDE3 inhibitors are used to treat heart failure. Defective cAMP signaling through the β-adrenergic system is a key determinant of exercise intolerance and reduced quality of life in cardiac patients. The exhaustive mapping of subcellular cAMP nanodomains and a detailed understanding of their regulation and functional role will provide an invaluable framework for the development of targeted therapeutics with reduced side effects.

Nonstandard Abbreviations and Acronyms

β-AR	β-adrenergic receptor
ARVM	adult rat ventricular myocyte
BAY	BAY 60-7550
CUTie	cAMP universal tag for imaging experiments
FRET	Förster resonance energy transfer
GATA4	GATA4 binding protein 4
GOCC	gene ontology cellular component
HDAC-1	histone deacetylase 1
HF	heart failure
hiPSC	human induced pluripotent stem cell
IBMX	3-isobutyl-1-methylxanthine
NRVM	neonatal rat ventricular myocyte
PDE	phosphodiesterase
PKA	protein kinase A
SMAD4	SMAD family member 4
TFA	trifluoroacetic acid

subcellular localization.[1] Cardiac myocytes express several isoforms belonging to the PDE1, PDE2A, PDE3, PDE4, and PDE8 cAMP-hydrolyzing PDE families.[2]

PDEs play a key role in cAMP subcellular compartmentalization by spatiotemporal regulation of cAMP signals, underpinning specificity of response.[3] The signaling pathway is organized in subcellular domains[4] where multiple components involved in cAMP signal transduction are organized in signalosomes. In these multiprotein complexes, the cAMP effector PKA (protein kinase A) is anchored, often via interaction with an AKAP (A kinase anchoring protein), in close proximity to a specific phosphorylation target, and the local level of cAMP is regulated by ≥1 PDE isoforms.[5] PDEs control the concentration of cAMP within a radius of a few tens of nanometers,[4,6,7] thus generating submicroscopic subcellular compartments with distinct cAMP levels (nanodomains). By locally degrading cAMP at specific signalosomes, the PDEs contribute to trigger a specific cellular response to a specific stimulus.[4,8–10] The subcellular distribution and activity of PDE isoforms ultimately defines the topography of active subcellular cAMP nanodomains.

cAMP signaling is disrupted in cardiac disease,[2] and drugs that target this pathway, such as β-AR antagonists, are a mainstay of current therapeutic regimens. However, available medications remain associated with serious side effects and are ineffective in a significant number of patients,[11] highlighting

the need for a better understanding of the signaling events involved. PDE3 inhibitors are approved for the treatment of heart failure (HF), but despite immediate positive inotropic effects, chronic use is associated with increased long-term mortality,[12] largely limiting their indication to short-term support of refractory, end-stage HF. The molecular mechanisms responsible for the long-term detrimental effects of PDE3 inhibition remain unclear.

The compartmentalized nature of cAMP signaling provides an opportunity for targeted therapeutic intervention[13–15] with potential benefit in terms of efficacy and reduced side effects. However, developing targeted interventions requires a detailed understanding of the subcellular organization of the cAMP signaling landscape. A comprehensive map of cAMP nanodomains generated by β-adrenergic stimulation and insight into their regulation and function would provide a valuable asset to dissect physiology, identify disease mechanisms, understand interactions with current medications, and provide a rational basis for the development of targeted therapeutics.[1]

Here, we used an integrated proteomics approach that combines the analysis of PDE family-specific phosphoproteomes with the analysis of PDE isoform-specific interactomes to infer the subcellular localization and function of so far unidentified cAMP nanodomains elicited by β-AR stimulation of cardiac myocytes. Given their clinical relevance, we focused on nanodomains under the control of PDE3A1 and PDE3A2—the most prevalent PDE isoforms in human myocardium.[16] Our results demonstrate that the integrated proteomics approach used here is a valid strategy to identify previously unknown subcellular cAMP nanodomains. In depth characterization of one of these domains demonstrates that PDE3A isoforms selectively control cAMP in the immediate vicinity of a nuclear PDE3A/SMAD4 (SMAD family member 4)/HDAC-1 (histone deacetylase 1) complex, resulting in modulation of gene transcription and control of cardiac myocytes hypertrophic growth.

METHODS

Data Availability

All data generated or analyzed during this study are included in this published article (and its Supplemental Material). The mass spectrometry proteomics data have been deposited to the ProteomeXchange Consortium via the Proteomics Identification Database (PRIDE) partner repository with the data set identifier PXD033773.

Chemicals

Cilostamide, forskolin, 3-isobutyl-1-methylxanthine (IBMX), isoproterenol, and norepinephrine were from Sigma-Aldrich; myristoylated PKA inhibitor was from Calbiochem; BAY 60-7550 (BAY) was from Cayman Chemicals; collagenase A was from Roche; pancreatin was from Sigma; laminin (mouse) was from BD Biosciences; PBS, DMEM high glucose, MEM199, horse serum, newborn calf serum, penicillin/streptomycin (10 000 units of penicillin [base] and 10 000 µg of streptomycin [base]/mL), and L-glutamine were from Invitrogen.

Antibodies and Fluorescent Reagents

PDE3A (catalog number A302-740A, 1:1000 [Bethyl Laboratory]; catalog number Sc-293446, 1:20 [Santa Cruz Biotechnology]), Flag (catalog number F7425, 1:2000; Sigma), GAPDH (catalog number 60004-1-1g, 1:5000; ProteinTech), Anti-phospho-PKA substrate antibody (catalog number 9621S or 9624, 1:1000; Cell Signaling), SMAD4 (catalog number 46535, GTX01674; Cell Signaling) GATA4 (GATA4 binding protein 4; catalog number 36966, 1:1000; Cell Signaling), HDAC-1 (catalog number 34589, 1:1000; Cell Signaling), lamin B (catalog number 12586, 1:1000; Cell Signaling), lamin A/C (catalog number 4777S, 1:1000; Cell Signaling), actin-1 alpha (catalog number 17521-1-AP; Proteintech), RFP (catalog number ab62341, 1:2000; Abcam), GFP (catalog number ab6556, 1:1000; Abcam), horseradish peroxidase–conjugated goat anti-mouse (catalog number sc2005, 1:5000 [SCBT]; catalog number 705-035-151 [Jackson ImmunoResearch Labs]) or anti-rabbit secondary antibodies (catalog number sc2030, 1:5000 [Santa Cruz Biotechnology]; catalog number 705-035-152 [Jackson ImmunoResearch Labs]), antibodies conjugated with Alexa-Fluor 647 (catalog number A-21235, 1:250; Thermo Fisher Scientific), Alexa-Fluor 488 (catalog number A-11008, 1:250; Thermo Fisher Scientific), and wheat germ agglutinin conjugated with Alexa 488 (catalog number W11261; Invitrogen).

Plasmids

Flag SMAD4 (clone Id Ora42717) and Flag HDAC-1 (clone Id Ora13308) were obtained from Genscript. The SMAD4–cAMP universal tag for imaging experiments (CUTie) sensor was generated by cloning SMAD4 in a pEYFPc1-CUTie vector[4] by using the NheI restriction site. Flag HDAC-1 alanine and aspartate mutants were generated by Genscript using the clone ID Ora13308 as a template.

Isolation and Culture of Cardiomyocytes

All animal procedures performed conform to the guidelines from directive 2010/63/EU of the European Parliament on the protection of animals used for scientific purposes. Adult rat ventricular myocytes (ARVMs) from 350 to 375 g both male and female Sprague-Dawley rats were isolated as described previously.[4,17] For phosphoproteomics and immunoblot analysis, fresh cells in tyrode buffer (130 mmol/L NaCl, 5 mmol/L HEPES, 0.4 mmol/L NaH_2PO_4, 5.6 mmol/L KCl, 3.5 mmol/L $MgCl_2$, 20 mmol/L taurine, 10 mmol/L glucose) containing 1.4 mmol/L $CaCl_2$ were used. Cells were treated with 10× working dilutions that would give final concentrations of 0.5 nM isoproterenol, 1 µmol/L BAY, 10 µmol/L cilostamide, or 100 µmol/L IBMX. After a treatment period of 10 minutes at room temperature, during which the cardiomyocytes were allowed to settle by gravity, the supernatant was taken off and cells were snap frozen in liquid nitrogen and stored at −80 °C until further processing. For viral infection, isolated ARVMs were plated on dishes

precoated with 1 µg/cm^2 laminin in culture medium (MEM 199, 5% fetal bovine serum [FBS], 5 mmol/L creatine, 2 mmol/L L-carnitine, 5 mmol/L taurine, 0.1× insulin-transferrin-selenium-X, 2 mmol/L L-glutamine, 100 units/mL penicillin, and 100 µg/mL streptomycin). Cells were washed with serum-free medium 2 hours after plating and subjected to adenoviral infection with vectors PDE3A1-mCherry, PDE3A2-mCherry, or mCherry only (Vector Biolabs).

Neonatal rat ventricular myocytes (NRVMs) from 2-days-old Sprague-Dawley pups were isolated as described before.[18] For viral transduction, 2.5 million cells were plated on laminin-coated 6 cm plates or on laminin-coated coverslips in M1 medium (4.5 g D-glucose/L DMEM [Invitrogen] with 17% M199 [Invitrogen], 10% horse serum, 5% newborn calf serum, 2 mmol/L L-glutamine, 100 units/mL penicillin and 100 µg/mL streptomycin). After 18 hours, medium was changed to M2 medium (4.5 g D-glucose/L DMEM [Invitrogen] with 17% M199 [Invitrogen], 5% horse serum, 0.5% newborn calf serum, 2 mmol/L L-glutamine and 100 units/mL penicillin, and 100 µg/mL streptomycin) and cells were allowed to adjust for 2 hours in a 37 °C humidified incubator with 5% CO_2. The cardiomyocytes were infected with adenoviral vectors encoding PDE2A2-mCherry, PDE3A1-mCherry, PDE3A2-mCherry, or mCherry only (Vector Biolabs). After 4 hours of infection, medium was replaced with fresh M2 medium. For plasmid transfection, the transfectin lipid reagent (Bio-Rad) was used following the manufacturer's instructions. The following day, cells were used for coimmunoprecipitations, immunofluorescence staining, label-free quantification shotgun proteomics, or cells were treated with norepinephrine (10 µmol/L) and other stimuli, as indicated.

Human Induced Pluripotent Stem Cell–Derived Cardiomyocytes

Human induced pluripotent stem cells (hiPSCs; LUMCi027-A-1 line,[19] LUMC0099iCTRL04 line,[20] M180 line,[21] and M398 line[21]) were cultured as described previously. Briefly, the LUMC lines were seeded on vitronectin recombinant human protein and cultured in E8 medium; cells were passaged twice a week using PBS containing EDTA 0.5 mmol/L. RevitaCell supplement (1:200) was added during passaging (all from Thermo Fisher Scientific). The M lines were cultured in mTeSR Plus medium (Stemcell Technologies) on human embryonic stem cell (hESC)-qualified Matrigel (8 µg/cm^2; Corning)-coated surfaces; cells were passaged twice a week using DPBS (Gibco) for rinsing and accutase (Sigma-Aldrich) for dissociation. The ROCK (Rho Kinase) inhibitor (StemMACS Y27632, 10 µmol/L; Miltenyi Biotech) was added for the first 24 hours after seeding. Differentiation into cardiomyocytes was induced in monolayer as described previously.[22] Differentiated human inducible pluripotent stem cell-derived cardiac myocytes (hiPSC-CM) were maintained in RPMI 1640 medium with Glutamax and 25 mM HEPES (Gibco) plus B27 supplement (Gibco). PDE3A2 overexpression experiments were performed at day 21 of differentiation by transducing hiPSC-CMs with PDE3A2-mCherry adenovirus. The medium was refreshed 24 hours post-transduction, and the cells were harvested after an additional 24 hours (48 hours post-transduction). Untransduced hiPSC-CMs were used as control.

Phosphoproteomics

For quantitative phosphoproteomic analysis, NRVMs, which survive in culture better than ARVMs, were transduced with adenoviral vectors encoding PDE2A2-mCherry, PDE3A1-mCherry, PDE3A2-mCherry, or mCherry only, as described above. Stable-isotope dimethyl labeling[23] was combined with titanium dioxide–mediated phospho-enrichment[24] and data-driven decision tree–dependent mass spectrometry.[25] Paired control and treatment samples from at least 3 different animals were analyzed. In brief, frozen cardiomyocyte pellets were thawed in AmBic/urea lysis buffer (8 mol/L urea, 50 mmol/L ammonium bicarbonate, PhosSTOP phosphatase inhibitor cocktail [Roche], and complete protease inhibitor cocktail [Roche]). Cell lysis was allowed to complete for 30 minutes at 4 °C under constant agitation, and cells were subsequently disrupted using a 21G needle. Tryptic digest of a total of 2 mg cardiomyocyte protein was performed using a 10-kD molecular weight cut off Filter Aided Sample Prep protocol. Disulfide bonds in aliquots of 400 mg protein per filter were reduced with 10 mmol/L tris(2-carboxyethyl)phosphine for 30 minutes and then alkylated with 50 mmol/L chloroacetamide for another 30 minutes in the dark. Proteins were washed twice with 6 mol/L urea in 50 mmol/L triethylammonium bicarbonate. Proteins were then digested; first with 1 µg MS grade Lys-C protease (Pierce) per 40 µg protein dissolved in 6 mol/L urea/50 mmol/L triethylammonium bicarbonate for 8 hours at 37 °C, followed by 1 µg MS grade trypsin per 40 µg protein dissolved in 50 mM triethylammonium bicarbonate for 4 hours at 37 °C. Tryptic peptides were eluted by spinning through the 10-kD molecular weight cut off filter. Filters were washed with 0.1% trifluoroacetic acid (TFA) and then with 50% acetonitrile in 0.1% TFA. The eluate was directly used for on-column stable-isotope dimethyl labeling using SepPak C18 cartridges (Waters) as described previously.[23] Titanium dioxide–packed tips (Thermo Fisher Scientific) were activated with 5% ammonium hydroxide and preequilibrated with loading buffer (2 mol/L glycolic acid, 10% TFA, and 80% acetonitrile). Samples were acidified by adding loading buffer 1:1, bringing glycolic acid to a final concentration of 1M and TFA to a final concentration of 5%. Samples were loaded onto the titanium dioxide columns at a low flow rate (20 µL/min). After all samples were loaded on the columns, they were washed sequentially with loading buffer, 0.2% TFA in 80% acetonitrile and 20% acetonitrile. The phosphopeptides were eluted twice with 5% ammonium hydroxide and immediately acidified with an equal volume of 20% formic acid. Phosphopeptides were analyzed on Orbitrap Elite (Thermo Fisher Scientific) coupled to an EASY-nano-LC 1000 system (Thermo Fisher Scientific) in which phosphopeptides were initially trapped on a 75-µm internal diameter guard column packed with Reprosil-Gold 120 C18, 3 µm, 120Å pores (Dr. Maisch GmbH) in solvent A (0.1% [vol/vol] formic acid in water) using a constant pressure of 500 bar. Peptides were then separated on a 45 °C heated EASY-Spray column (50 cm×75 µm ID, PepMap RSLC C18, 2 µm; Thermo Fisher Scientific) using a 3-hour linear 8% to 30% (vol/vol) acetonitrile gradient and constant 200 nL/min flow rate. Peptides were introduced via an EASY-Spray nanoelectrospray ion source into an Orbitrap Elite mass spectrometer (Thermo Fisher Scientific). Spectra were acquired with resolution 30 000 m/z; range, 350 to 1500; AGC target, 1×10^6; and maximum injection time, 250 ms. The 20 most abundant peaks were fragmented using collision

induced dissociation (automatic gain control target, 5×10^3; maximum injection time, 100 ms) or electron-transfer dissociation (automatic gain control cation and anion target, 5×10^3 and 2×10^5, respectively; maximum injection time, 100 ms; normalized collision energy, 35%) in a data-dependent decision tree method. Peptide identification and quantitation of heavy-to-light ratios was then performed using MaxQuant (v1.6.1.0).[26] Groups were analyzed with a multiplicity of 2, accounting for the light and heavy dimethyl labels, and phospho (STY) was specified as a variable modification along with protein oxidation and N-terminal acetylation. Trypsin/P was selected as specific digestion mode with a maximum of 2 missed cleavages. Carbamidomethyl groups were accounted for as fixed modifications, and the match between runs function was enabled with a match time window of 0.7 minutes and an alignment time window of 20 minutes. Downstream data processing was performed using the Perseus software package (v1.6.1.1).[27]

Label-Free Quantification Shotgun Proteomics

Following affinity purifications of PDE2A2-mCherry, PDE3A1-mCherry, PDE3A2-mCherry, or mCherry from NRVM lysates using RFP-Trap beads, bound proteins were eluted with urea (8 mol/L) under denaturing conditions. Proteins were digested to peptides for interactome analysis with MS grade Lys-C protease (Pierce) for 4 hours at 37 °C, followed by reduction with 2 µmol/L dithiothreitol for 15 minutes at 65 °C and alkylation with iodoacetamide for 30 minutes at room temperature and in the dark. After dilution of the buffer to 2 mol/L urea, further digest with MS grade trypsin was performed for 16 hours at 37 °C. LC-MS/MS was performed using a Q Exactive Hybrid Quadrupole-Orbitrap Mass Spectrometer (Thermo Fisher Scientific). Mass spectra were searched against the Uniprot *Rattus norvegicus* reference proteome (downloaded on July 6, 2014) and quantified using MaxQuant (v1.5.0.0).[23] Settings were as follows: 2 missed cleavages, carbamidomethylation on cysteine residues as fixed modification, protein oxidation, and N-terminal acetylation as variable modification. The search space was limited to a peptide mass tolerance of 20 ppm and an MS/MS mass tolerance of 0.5 Da. The match between runs function was enabled with a match time window of 0.5 minutes and an alignment time window of 20 minutes. Downstream data processing was performed using the Perseus software package (v1.5.5.3).[24]

Network Analysis

Area-proportional Venn diagrams were created using BioVenn.[25] Gene ontology term analysis for phosphoproteome and interactome target lists was performed using the ClueGO Cytoscape plug-in (v2.5.8).[26] Category enrichment analysis of PDE3A2, PDE3A1, and PDE2A2 interactors and PDE3 and PDE2A upregulated phosphoproteins was performed with STRING,[27] using gene ontology cellular component (GOCC) and default parameters. Next, proteins annotated to the GOCC term nucleus were extracted from the list of PDE3A2, PDE3A1 interactors, and PDE3A upregulated phosphoproteins. Common nucleus-annotated PDEA1 and PDEA3 interactors and nucleus-annotated PDE3A upregulated phosphoproteins were used to query STRING for functional and physical interactions. The following settings were used: network type: full STRING network; active interaction sources: experiments and databases; minimum required interaction score: 0.900.

Immunofluorescence

NRVMs plated on coverslips were treated with dimethyl sulfoxide (DMSO) or leptomycin B (100 nmol/L) for 3 hours, washed 3× with PBS, and fixed with 4% PFA in PBS at room temperature for 15 minutes. After permeabilization with PBS+0.1% Triton-X-100 (PBST) for 30 minutes, the coverslips were blocked in PBST+10% FBS for 1 hour at room temperature. Primary antibody incubations were performed overnight at 4 °C, followed by 3 washes at room temperature with PBS+0.025% Tween 20 and detection with Alexa-Fluor conjugated secondary antibodies for 1 hour before staining with DAPI (1 µg/mL) for 10 minutes. Coverslips were mounted in Ibidi mounting media and sealed with nail polish. Sequential confocal images were acquired on a confocal laser scanning microscope (TCS SP5 II; Leica, Germany). Nuclear and cytoplasmic fluorescence intensity was calculated by drawing a region of interest with ImageJ V1.53K.[28]

Immunoprecipitation and Immunoblotting

For immunoprecipitations from ARVMs or hiPSCs-CM, cells were infected with adenovirus Ad-HDAC-1 virus (catalog number 1498; Vector Biolabs) including an mCherry reporter or PDE3A2-mCherry or mCherry alone (Vector Biolabs). When using hiPSC-CMs, 21-day-old cells were transduced with adenoviral vector. After 24 hours post-transduction, the medium was refreshed, and the cells were treated with cilostamide (10 µmol/L), cilostamide (10 µmol/L) in combination with the PKA inhibitory peptide PKA inhibitor (20 µmol/L), isoproterenol (0.5 nmol/L), a saturating stimulus (25 µmol/L forskolin and 100 µmol/L IBMX), or control medium (DMSO) for 30 minutes and immediately harvested. hiPSC-CMs were dissociated using the multitissue dissociation kit 3 (Miltenyi Biotec) following the manufacturer's instructions. The cell pellet was washed 3× using ice-cold PBS and then stored at −80 °C after snap freezing in liquid nitrogen to preserve protein integrity. NRVM and HEK293 (Human Embryonic Kidney 293) cells were transfected with plasmid carrying FLAG-HDAC-1. Twenty-four hours post-transfection, the cells were treated with cilostamide (10 µmol/L), a saturating stimulus (25 µmol/L forskolin and 100 µmol/L IBMX), cilostamide 10 µmol/L+PKA inhibitor (10 µmol/L), isoproterenol (0.5 nM), or control medium (DMSO) for 45 minutes and immediately harvested. For immunoprecipitation of the transfected or infected cells, lysates were prepared using an IP buffer (50 mM HEPES pH7.4, 150 mM NaCl, 2 mM EDTA, 10% glycerol, 0.5% Triton-X-100 or 50 mM Tris pH7.4, 150 mM NaCl, 1 mM EDTA, and 1% nonyl phenoxypolyethoxylethanol [NP40]), supplemented with PhosSTOP phosphatase inhibitor cocktail (Roche) and complete protease inhibitor cocktail (Roche). For tissue lysis, isolated left ventricles from rats were homogenized with a tissue homogenizer (Miccra D-4; ART Prozess- & Labortechnik GmbH & Co. KG; Müllheim, Germany) in lysis buffer (10 mM K_2HPO_4, 150 mM NaCl, 5 mM EDTA, 5 mM EGTA, 0.5% Triton-X-100, pH7.4, and 0.2% sodium deoxycholate) supplemented with protease and phosphatase inhibitors. Affinity purifications were performed for 2.5 hours using 25 µL RFP-Trap beads (Chromotech) or Flag M2 agarose beads (Sigma) per biological replicate. For immunoprecipitation of endogenous proteins, lysates were incubated overnight at 4 °C with anti-PDE3A or anti-SMAD4 antibodies and protein A sepharose beads (Sigma-Aldrich) or protein A agarose (Thermoscientific) for 6 to 8 hours at 4 °C. For immunoblotting, ARVMs were lysed in AmBic/urea lysis buffer (8 M urea and 50 mM ammonium bicarbonate) supplemented

with protease and phosphatase inhibitor cocktails (Roche). Cell debris was removed by centrifugation at 4 °C for 20 minutes at 16000*g*. Protein concentrations were determined using the Bradford assay (Bio-Rad). Accordingly, 10 to 30 µg of protein per sample was resolved on 4% to 12% Bis-Tris polyacrylamide gels (Invitrogen) or 8% SDS-PAGE gel and transferred to nitrocellulose membranes using the XCell II Blot Module (Thermo Fisher Scientific). To prevent nonspecific binding of the primary antibody, membranes were blocked in 5% milk (Millipore) or phosphoblocker (Cell Biolabs) made in TBST for 1 hour at room temperature. Incubation with the appropriate dilution of primary antibody was performed at 4 °C overnight with gentle agitation. Horseradish peroxidase–conjugated secondary antibodies were used at a dilution of 1:5000. The amount of peroxidase activity remaining on the membrane after washes with TBST was determined using X-Ray Film (GE Healthcare), in combination with Clarity ECL developing solution (Bio-Rad) or Supersignal West Atto (Thermo Scientific). Chemiluminescent signal was also detected by using a ChemiDoc XRS+ (Bio-Rad) imaging system. Quantification of the obtained signal was performed using densitometry analysis with ImageJ V1.53K.[28]

RNA Isolation and Analysis

After isolation, NRVMs were washed with PBS, and RNA was isolated using the QIAGEN RNeasy kit, following the manufacturer's protocol. One microgram of total RNA was used to synthesize cDNA using QuantiTect Reverse Transcription Kit (Qiagen) according to the manufacturer's instructions. For the quantitative real-time polymerase chain reaction for GATA4, the TaqMan Gene Expression assay primer Rn01530459_m1 and for GAPDH, the TaqMan Gene Expression assay primer Rn01775763_g1 from Applied Biosystems were used. Quantitative real-time polymerase chain reactions were performed in a 7300 Real-Time PCR System (Applied Biosystems). The relative level of GATA4 mRNA was normalized to the DMSO control and respective GAPDH levels. Fold change was calculated using the 2(−ΔΔCt) method.[29] Total RNA from hiPSC-CMs was extracted using the RNeasy Micro Kit (Qiagen), and 500 ng of RNA was reverse transcribed using the iScript cDNA synthesis kit, following the manufacturer's instruction. iTaq Universal SYBR Green Supermix was used for cDNA amplification on CFX96 Real-Time PCR Detection System (all from Bio-Rad) using the following conditions: 95 °C 3 minutes/95 °C 30 s; 60 °C 1 minute for 39 cycles/95 °C 10 s; melt curve 60 °C to 95 °C with increment of 0.5 °C. All quantitative PCR (qPCR) reactions were performed in triplicate. Gene expression levels for *GATA4* (forward primer GGCCTGTCATCTCACTACGG; reverse primer ATGGCCAGACATCGCACT), *NPPA* (forward primer CCGTGAGCTTCCTCCTTTTA; reverse primer CCAAATGGTCCAGCAAATTC), and *NPPB* (forward primer CTCCAGAGACATGGATCCCC; reverse primer GTTGCGCTGCTCCTGTAAC) were normalized to DMSO and the correspondent *RPL37A* housekeeping gene (forward primer GTGGTTCCTGCATGAAGACAGTG; reverse primer TTCTGATGGCGGACTTTACCG).

Förster Resonance Energy Transfer Imaging

For Förster resonance energy transfer (FRET) measurements, NRVMs were plated on laminin-coated glass coverslips (0.5 µg/cm^2) and allowed to adhere for 2 hours in a 37 °C humidified incubator with 5% CO_2. Adenoviral vector encoding the cyclic AMP FRET reporter CUTie was added to the cardiomyocyte medium, and infection was allowed for 3 hours in a 37 °C humidified incubator with 5% CO_2. The medium was then replaced with fresh FBS-free medium. For SMAD4-CUTie imaging, HEK293 cells or NRVMs were transfected with TransFectin lipid reagent (Bio-Rad), JetPrime (PolyPlus), or FuGENE HD (Promega), following the manufacturer's instructions. FRET experiments were performed 24 to 48 hours after adenoviral transduction or transfection. Before the experiments, cells were treated with leptomycine B (100 nmol/L) for 3 hours in a 37 °C humidified incubator with 5% CO_2. For imaging, cells were kept in a modified Ringer saline solution (NaCl 125 mmol/L, KCl 5 mmol/L, Na_3PO_4 1 mmol/L, $MgSO_4$ 1 mmol/L, HEPES 20 mmol/L, glucose 5.5 mmol/L, CaCl2 1 mmol/L, and pH7.4) and imaged on an Olympus IX71 inverted microscope using a PlanApoN, ×60, oil immersion objective (numerical aperture 1.4, 0.17/field number 26.5, Olympus, United Kingdom). The microscope was equipped with a CoolSNAP HQ^2 monochrome camera (Photometrics) and a DV2 Dual-View beam splitter (Photometrics; MAG Biosystems). The FRET filter settings used throughout were CFP excitation filter ET436/20, dichroic mirror 455DCLP (Chroma Technology) in the microscope filter cube, a 505DCLP dichroic mirror, 535/40 YFP (yellow fluorescent protein) and 480/30 CFP (cyan fluorescent protein) emission filters (Chroma Technology) in the beam splitter. Images were acquired and analyzed using MetaFluor 7.1 (Molecular Devices). FRET changes were measured as changes in the background-subtracted 480/535 nm (Epac-S^{H187}) or 535/480nm (CUTie and SMAD4 CUTie) fluorescence emission intensity on excitation at 430 nm and expressed as percent FRET ratio change of R/R0, where R is the fluorescence emission ratio at time t and R0 is the average baseline ratio (5–10 samples) short before the first stimulus is added.

HDAC Activity

Histone deacetylase activity of HDACs was measured using a fluorometric histone deacetylase kit (CS1010; Sigma-Aldrich) following the manufacturer's instructions. Equal volumes of purified HDAC-1 beads obtained from immunoprecipitates from cells expressing HDAC-1-Flag as described above were used. For the HDAC assay, 30 µL of assay buffer were added to 100 µmol/L HDAC substrate and 20 µL of washed HDAC-1 beads. After 30 minutes of incubation at 30 °C, 10 µL of the developer solution was added, allowing the fluorescent reporter to be released from the deacetylated substrate. Fluorescence was detected using a Cytation image plate reader (BioTeK) with excitation at 355 nm and emission at 460 nm. Measurements were taken from 4 different biological replicates and normalized to the amount of HDAC-Flag present in each sample, as determined by quantification of a 30-µL sample subjected to Western blotting.

In Vitro Hypertrophy and Cell Size Measurements

For NRVM, cells were prepared as described above. Twenty-four hours after isolation, the cells were treated with cilostamide (10 µmol/L), norepinephrine (10 µmol/L), or control medium (DMSO) for 48 hours before cell size determination. For ARVM, cells were suspended in ARVM serum-free medium (MEM 199, 100 units/mL penicillin, 100 µg/mL streptomycin, 5 mmol/L creatine, 2 mmol/L L-carnitine, 5 mmol/L taurine, insulin-transferrin-selenium-X 1X, and 2 mmol/L L-glutamine) and plated on dishes precoated with 1 µg/cm^2 laminin. Cells were washed with serum-free medium 2 hours after plating and subjected to adenoviral infection with the vectors PDE3A1-mCherry, PDE3A2-mCherry, or mCherry only (Vector Biolabs). After 24 hours, the cells were

treated with norepinephrine (10 µmol/L) or other stimuli as indicated for 24 hours, followed by cell size measurement. hiPSC-CMs were dissociated and seeded at a cell density of 5×10^5 cells per well in a Matrigel-coated 12-well plate for RNA extraction or at a cell density of 1×10^4 cells per well on Matrigel-coated black 96-well plate for immunofluorescence. hiPSC-CMs were cultured for 48 hours to allow their recovery after dissociation; then the medium was refreshed and the cells were treated with cilostamide (10 µmol/L), norepinephrine (10 µmol/L), or control medium (DMSO) for 7 days, refreshing the medium every 48 hours. At day 4, cells were then transduced for 24 hours with adenoviral vector encoding mCherry alone or PDEA3A2 DN-mCherry. For determination of cell size, cells were imaged in bright-field mode on an Olympus IX71 inverted microscope, equipped with Olympus 40× UPlanFLN and 60× PlanApoN oil immersion objectives (NA 1.3 and 1.42, respectively) using MetaFluor 7.1 (Molecular Devices). Cell membranes were decorated using 5.0 µg/mL wheat germ agglutinin (Invitrogen) in PBS incubated for 10 minutes at room temperature. When required, epifluorescence images were taken using either a YFP illumination set (excitation filter ET500/30, dichroic mirror T515LP, emission filter ET535/30; Chroma Technology) or an RFP set (excitation filter 559/34, dichroic mirror 585LP, emission filter 630/69; Semrock). Cell surface area was calculated with ImageJ by drawing a region of interest including the cell area and by analyzing the number of pixels within the region of interest.

Hypertrophy experiments with dominant negative PDE3 isoforms were conducted at days 30 to 37 after differentiation start. Cells were seeded at a density of 15 000 cells/cm^2 on Matrigel-coated glass coverslips and grown for 3 to 5 days before the treatment. Cells were then transduced with adenoviral vector encoding dominant negative PDE3A1 and 3A2-mCherry and mCherry alone as control. Treatment with and without norepinephrin (10 µmol/L) was started at the same time. After 48 hours, cells were imaged in differential interference contrast and area was measured using Metafluor 7.1 (Molecular Devices) for acquisition and analysis. All measured cells were also controlled for effective transduction by detecting the red fluorescence of the cells. Measurements were taken on Nikon Eclipse FN-1, equipped with an Opto-LED fluorescent light source (Cairn-Research) and a CoolSnap HQ^2 camera (Photometrix). All images were acquired with a 40×/0.8 numerical aperture, long distance water dipping objective (Nikon).

In Vivo Adrenergic Challenge and Cardiac Tissue Analysis

Male rats (circa 6–8 months) were used and phenotyped as described.[10] Osmotic minipumps (Alzet 2ml2; Charles River Wiga, Sulzfeld, Germany) were implanted for administration of saline (0.9% NaCl+0.02% ascorbic acid) or isoproterenol (0.13 mg/kg per hour). On day 14 after the implantation, the hearts were collected, cut along the transverse axis, immediately fixed in 10% formalin, and stored at least for 24 hours. The samples were embedded in the paraffin and cooled overnight at 4 °C. Sections (2 or 5 µm thick) were prepared from paraffin blocks using a microtome and mounted on microscope slides. The samples were rehydrated by deparaffinizing twice in xylene (2×5 minutes) and running through a decreasing ethanol series (100%, 96%, 80%, and 70% for 5 minutes each). For further processing, the slides were washed 3× in 1× PBS. Visualization of cardiac myocytes was performed immediately after rehydration of the samples. After blocking nonspecific binding (60 minutes with 10% nanodomains in 1× PBS at room temperature in a humidified chamber), the directly coupled WGA was applied (1:100 in 10% normal donkey serum, 4 °C, in a humidified chamber). A secondary antibody was not required. After incubation, samples could be covered with Vectashield/DAPI. For picrosirius staining (Morphisto; 13422), the sections were incubated for 60 minutes in the dark, washed 2×5 minutes with 0.005% vinegar water, dehydrated in ethanol series (3×99.8%), and immersed in xylene (2×5 minutes). Finally, the sections were covered with Eukitt.

Statistical Analysis

Statistical significance tests for proteomics data were performed within the Perseus proteomics software package (v1.6.1.1). Other statistical tests were performed using Sigma Plot v13.0 (Systat Software, Inc) and Prism 5 or Prism 9 (GraphPadPrism). Data are presented as mean±SEM. For $n > 10$, normal distribution of the experimental data was tested with the Anderson-Darling normality test. For comparisons between 2 groups, Student *t* test was used for normally distributed data, For non-normally distributed data or $n \leq 10$, a Mann-Whitney *U* test (unpaired data) or a Wilcoxon signed-rank test (paired data) was used. For comparison between >2 groups, Kruskal-Wallis test followed by a Dunn multiple comparison (non-normal distribution with nonpaired groups or $n \leq 10$) or Friedman test followed by a Dunn multiple comparison (non-normal distribution or $n \leq 10$ with paired groups) was performed. To account for dependency, a hierarchical analysis model in R using the lme4 package with clustering for individual cells followed by Bonferroni correction for multiple comparisons was applied (as previously described in the study by Sikkel et al[30]). Non-normally distributed data were log transformed before hierarchical statistical testing. *P* values of <0.05 were considered statistically significant. Number of experimental animals and cells per group were chosen based on our experience in previous experiments. Representative images were chosen to closely match the average values of the respective groups. Additional information on statistical analysis is provided in Appendix S4.

RESULTS

PDE Family-Specific Phosphoproteomes

Application of a PDE family-selective inhibitor is expected to result in a cAMP increase only at the subcellular sites where isoforms belonging to that family localize, leading to confined activation of PKA and local substrate phosphorylation. From the analysis of the phosphoproteome upregulated on inhibition of a specific PDE family, it should be possible to gain information on the location of cAMP nanodomains under the control of that particular PDE family. To test the validity of this approach for uncovering novel PDE-specific cAMP nanodomains, we analyzed the phosphoproteome associated with inhibition of PDE3 and compared it to the phosphoproteome associated with inhibition of PDE2A. As our aim was to reveal previously unappreciated cAMP nanodomains elicited by sympathetic stimulation, we applied the PDE family-selective inhibitors in combination with the β-AR agonist isoproterenol. Using the cytosolic

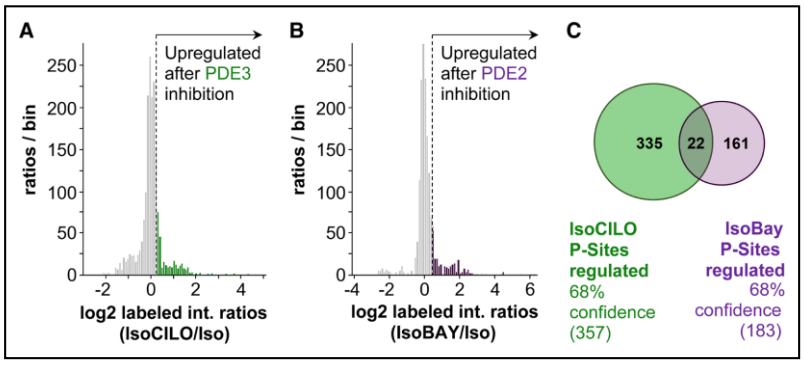

Figure 1. Analysis of the β-adrenergic phosphoproteome selectively elicited by inhibition of PDE3 (phosphodiesterase 3) or PDE2A.

A, Frequency distributions of log2 intensity ratios to illustrate thresholding of PDE3-dependent and PDE2A-dependent (**B**) phosphoproteomics data for pathway analysis. The top 16% quantified phosphopeptides (highlighted in green and purple for PDE3A and PDE2A, respectively) were carried forward for further analysis. **C**, Venn diagram comparing the 16% upregulated phosphorylation sites in samples treated with the PDE3 inhibitor (green) or the PDE2A inhibitor (purple). The CI (68%) derives from the selected peptides lying outside 1 SD of the mean distribution of peptides, as shown in **A** and **B**, respectively. BAY indicates BAY 60-7550; Cilo, cilostamide; and Iso, isoproterenol.

FRET biosensor EPAC-S^{H187} to measure cAMP,[31] we optimized the concentration of isoproterenol so that, on subsequent addition of the PDE inhibitor, the following criteria would be satisfied: (1) generation of a relatively contained increase in cAMP, sufficient to engage the relevant PDE hydrolytic activity but with minimal overspill and disruption of compartmentalization; (2) generation of a comparable overall cellular amount of cAMP on application of the PDE inhibitors, to avoid that differences in target phosphorylation may result from grossly unequal global cAMP levels; (3) generation of a functionally relevant signal, as determined by detectable activation of PKA. Treatment of ARVMs with 0.5 nmol/L isoproterenol satisfies all 3 criteria (Figure S1).

Cell lysates from ARVMs treated with 0.5 nmol/L isoproterenol alone or in combination with the PDE3 inhibitor cilostamide (10 µmol/L) or the PDE2A inhibitor BAY (1 µmol/L) were prepared for quantitative LC-MS/MS, as shown in Figure S2. For ARVMs treated with cilostamide, proteins were identified after titanium dioxide enrichment, 264 of which were quantified (Figure S3A). For ARVMs treated with BAY, 776 proteins were identified, 270 of which were quantified (Figure S3B). This corresponds to 2231 and 1146 detected phosphorylation sites in cardiomyocytes treated with a combination of isoproterenol+cilostamide or isoproterenol+BAY, respectively (Figure S3C). As prestimulation with isoproterenol lead to considerable baseline phosphorylation, the dynamic range of the observed ratios between PDE inhibitor and control was narrow, with many substrates showing little or no change. For data analysis, we, therefore, applied an intensity-based thresholding approach,[32,33] considering all phosphorylation sites within the top 16% intensity ratios as differentially regulated (Figure 1A and 1B). A full list of the differentially regulated phosphopeptides is shown in Appendix S1. In line with what is expected, of the quantified upregulated phosphorylation sites, 42% and 41% were annotated as containing a PKA motif in the sample treated with cilostamide and BAY, respectively (Figure S4A and S4B). This enrichment for PKA sites was conserved in the top 16% sites differentially regulated upon inhibitor treatment (35% of the 357 PDE3-regulated sites and 43% of all 183 PDE2A-dependent phosphorylation sites were annotated as PKA sites; Figure S4C and S4D). Of the differentially regulated sites, only 22 sites in 22 different proteins were found in both the PDE3- and the PDE2A-dependent phosphoproteomes (Figure 1C; Table S1), 32% of which contain a PKA motif. These 22 phosphopeptides correspond to only 6% of the differentially regulated phosphorylation sites, supporting the notion that PDE3 and PDE2A enzymes operate largely independently in distinct subcellular compartments and indicating that the analysis of PDE family-dependent phosphoproteomes is a valid approach to identify targets under the control of individual PDE families.

PDE Isoform-Specific Interactomes

Available PDE inhibitors are family-selective but do not discriminate between different PDE isoforms within a family. To increase the resolution of our investigation and gain information on where specific PDE isoforms operate, we analyzed the interactomes of the PDE3 family isoforms PDE3A1 and PDE3A2 and compared them to the interactome of the PDE2A2 isoform. Individual PDE isoforms tagged with mCherry or mCherry alone were expressed in isolated NRVMs. Confocal imaging confirmed that the 3 selected PDE isoforms show largely distinct subcellular localization, with PDE3A1 showing a predominant pattern compatible with internal membranes,

PDE3A2 showing a somewhat more homogeneous distribution within the cell, and PDE2A2 showing a distribution in line with the predominantly mitochondrial localization described previously[34] (Figure S5). After immunoprecipitation and tryptic digest of the coprecipitated proteins, the samples were separately analyzed by mass spectrometry (Figure S6). We identified 1979, 1900, and 1871 proteins for the PDE3A1, PDE3A2, and PDE2A2 interactomes, respectively (Figure S7). *t* test analysis using mCherry alone as control yielded 464 potential interaction partners for PDE3A1, 139 interaction partners for PDE3A2, and 210 interaction partners for PDE2A2 (significance thresholds are false discovery rate [FDR], 0.03 and S-zero is the fold-change threshold [S0], 1.3 for the PDE3A1 interactome; FDR, 0.5 and S0, 0.8 for the PDE3A2 interactome; and FDR, 0.05 and S0, 1.3 for the PDE2A2 interactome; Figure 2). Overall, the data show that, at least for PDE3A1 and PDE2A2, a considerable proportion of the interactors is unique for the specific PDE isoform (Figure 2E). The presence of shared interactors between isoforms is in line with the observation that multiple PDEs can impinge on the same subcellular compartment, where they may have synergistic effect.[35] A full list of the proteins significantly enriched in the PDE3A1, PDE3A2, and PDE2A2 interactomes is shown in Appendix S2.

Integrated Analysis of Interactomes and Phosphoproteomes Reveals Potential Novel cAMP Nanodomains

Analysis of the interactome and phosphoproteome data for a specific PDE revealed a number of proteins significantly enriched in both data sets (Table 1). If a protein features in the interactome of a specific PDE isoform and the phosphorylation of the same protein is selectively enhanced by treatment with the relevant family-selective inhibitor, it is likely that such protein pinpoints the site of a cAMP nanodomain under the specific control of that particular PDE. In support of this notion, we found that the SERCA2 (sarco-endoplasmic reticulum calcium ATPase 2; *Atp2a2*) appears only in the PDE3A-dependent phosphoproteome and in the PDE3A1 interactome (Table 1), in agreement with previous work reporting interaction of PDE3A with SERCA[36] and involvement of PDE3A in the regulation of SERCA activity.[37] Similarly, the NHE1 (Na^+/H^+ exchanger 1; *Slc9a1*) appeared selectively in the PDE3A phosphoproteome and in the PDE3A1 interactome, in line with evidence linking cardiac PDE3 and regulation of NHE1.[38] The PMCA (plasma membrane Ca^{2+}-ATPase; *Atp2b1*) appeared in the PDE2A2 interactome and the PDE2A-associated phosphoproteome exclusively, consistent with a role of PDE2A in the regulation of PMCA in cardiac myocytes.[39] Thus, we suggest that the presence in both the phosphoproteome and interactome data sets can be used as a criterion to prioritize proteins for further validation. Application of a less stringent selection criterion may, however, be equally valuable, as cAMP signalosomes often involve complex multiprotein assemblies and the protein phosphorylated on inhibition of a local PDE may not necessarily interact with the PDE itself. To identify these signalosomes, we performed gene

Table 1. List of Gene Names Encoding for Proteins Identified as Significantly Enriched in Both the Phosphoproteome and Interactomes Data Sets

PDE3A1	PDE3A2	PDE2A2
Actn2	*Chchd3*	*Atp2b1*
Atp1a1	*Dusp27*	*Banf1*
Atp2a2	*Fry*	*Canx*
Atp5a1	*Hsp90aa1*	*Hsp90aa1*
Canx	*Map7d1*	*Igf2r*
Chchd3	*Mtdh*	*Myh7*
Des	*Myo18a*	*Txlnb*
Dusp27	*Pbxip1*	
Eif3c	*Plec*	
Fam134c	*Ppp2r5a*	
Flnc	*Speg*	
Fry	*Strn*	
Hnrnpa1	*Ubap2l*	
Hnrnpc	*Ybx1*	
Hsp90aa1		
Igf2r		
Map7d1		
Matr3		
Myh6		
Myo18a		
Npm1		
Pbxip1		
Plec		
Ppp2r5a		
Rbm39		
RGD1561609		
Rplp0		
Rplp2		
Sgca		
Slc9a1		
Speg		
Strn		
Stx4		
Tbc1d4		
Tmem55a		
Ttn		
Ubap2l		
Vdac1		
Xirp1		
Ybx1		

PDE indicates phosphodiesterase.

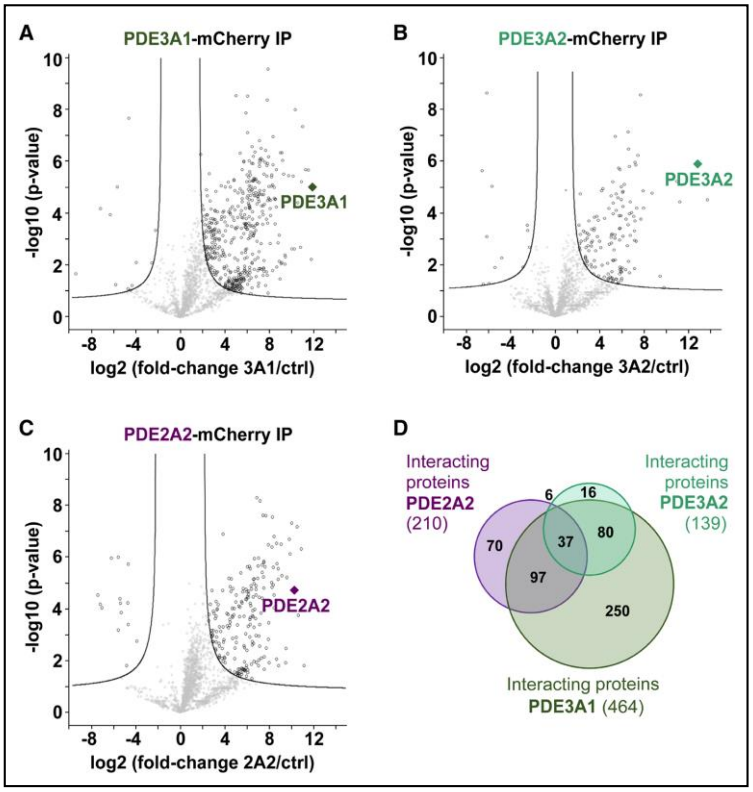

Figure 2. Analysis of the PDE3A1 (phosphodiesterase 3A1), PDE3A2, and PDE2A2 interactomes.
A, Volcano plot of the PDE3A1-mCherry interactome (false discovery rate [FDR], 0.03; S-zero is the fold-change threshold [S0], 1.3). **B**, PDE3A2-mCherry interactome (FDR, 0.05; S0, 0.8). **C**, PDE2A2-mCherry interactome (FDR, 0.03; S0, 1.3). **D**, Area-proportional Venn diagram to compare significant interactors in PDE3A1, PDE3A2, and PDE2A2 affinity purifications.

ontology cellular component (GOCC) term enrichment analysis to find terms enriched simultaneously in a PDE isoform interactome and the relevant phosphoproteome to generate functional networks that may reveal nonobvious cAMP nanodomains under the control of specific PDE isoforms. GOCC analysis of our data sets showed a highly significant enrichment for the term nucleus for PDE3 (for the PDE3A1 interactome: 107/6630 genes and FDR, 9.91×10^{-43}; for the PDE3A2 interactome: 68/6630 genes and FDR, 7.32×10^{-6}; for the PDE3 phosphoproteome: 107/6630 genes and FDR, 4.4×10^{-10}; Appendix S3). Next, we used the nucleus-annotated interactors shared by PDE3A1 and PDE3A2 and nucleus-annotated phosphoproteins upregulated on cilostamide treatment as input to generate a functional and physical interaction network using STRING software with stringent settings to pinpoint likely interactions (Figure 3). Among the interactions identified, we focused on the CtBP2 (C-terminal Binding Protein 2)/phospho-HDAC-1/SMAD4 transcription regulatory complex for further validation and tested the hypothesis that PDE3A isoforms selectively regulate a nuclear cAMP nanodomain that involves SMAD4 and HDAC-1 to control gene transcription and hypertrophy.

PDE3A Isoforms Localize to the Nucleus and Form a Complex With SMAD4 and HDAC-1

We first sought to confirm the interaction between SMAD4 and PDE3A isoforms. Western blot analysis of RFP pulldowns obtained from NRVMs expressing RFP-tagged PDE3A1 or PDE3A2 showed endogenous SMAD4 in the RFP immunoprecipitate (Figure S8A). HDAC-1 was also detected in the same immunoprecipitate (Figure S8A), indicating that PDE3A isoforms, SMAD4 and HDAC-1 can be part of the same complex. To further confirm the interaction between SMAD4 and PDE3A, Flag-tagged SMAD4 was expressed in NRVMs and the Flag immunoprecipitate probed with anti-PDE3A antibody. As shown in Figure S8B, reactivity was detected for endogenous PDE3A2 but not PDE3A1. Interaction

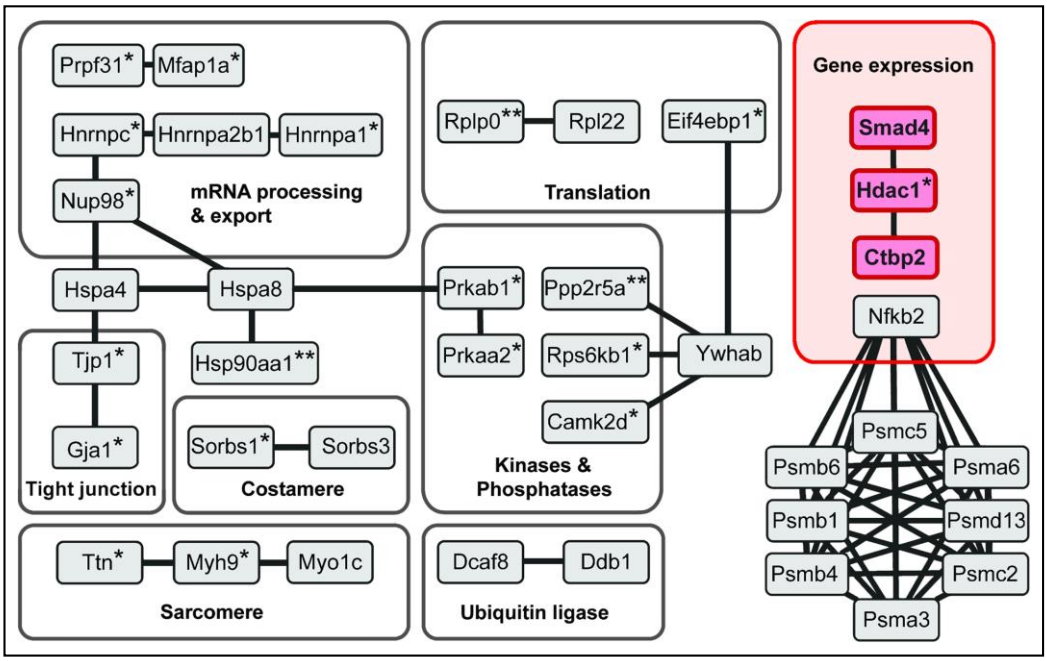

Figure 3. Nuclear protein interaction network shared by PDE3A1 (phosphodiesterase 3A1) and PDE3A2.
Functional and physical interaction network of PDE3A1/A2 interactors and phosphorylated downstream proteins generated with the STRING software. All proteins shown have been identified experimentally either in the cilostamide-dependent phosphoproteome or in the interactome shared by PDE3A1 and PDE3A2. *Proteins found in the cilostamide-dependent PDE3A phosphoproteome. **Proteins that are both in the cilostamide-dependent phosphoproteome and in the PDE3A isoform interactomes.

of PDE3A isoforms with SMAD4 and HDAC-1 was further confirmed for proteins expressed at endogenous level in NRVM, as shown inFigure 4A and 4B. At the endogenous level, only PDE3A2 appears to be part of the PDE3A/SMAD4/HDAC-1 complex (Figure 4A). Interaction between endogenous PDE3A and SMAD4 is also detectable in rat tissue immunoprecipitates (Figure S8C). Further, we confirmed the interaction between PDE3A2-RFP, endogenous SMAD4, and endogenous HDAC-1 in ARVMs (Figure S8D) and the interaction between PDE3A2-RFP and endogenous SMAD4 in human cardiac myocytes differentiated from hiPSC-CMs (Figure S8E).

Studies in other cell types have shown that while SMAD4 is distributed both in the cytoplasm and in the nucleus,[40] HDAC-1 is exclusively found in the nucleus,[41] as we confirmed in NRVM (Figure S9A). Our finding that PDE3A isoforms coimmunoprecipitate with HDAC-1 (Figure 4A and 4B) suggests that at least a fraction of PDE3A enzymes must localize to the nucleus. Analysis of the PDE3A1 and PDE3A2 amino acid sequences using the eukaryotic linear motif prediction tool (http://elm.eu.org/) indeed identified several nuclear localization sequence motifs and a nuclear export sequence known as CRM1 (chromosomal maintenance 1) binding sequence (Figure S9B). Immunostaining of NRVM using anti-PDE3A–specific antibodies confirmed localization of PDE3A to the nucleus that was significantly enhanced upon treatment with leptomycin B—an inhibitor of CRM1-mediated nuclear export (Figure 4C; Figure S9C). Consistently, Western blot analysis of NRVM cytosolic and nuclear fractions showed that, on average, about 30% of total PDE3A2 and 15% of total PDE3A1 localize to the nucleus (Figure 4D)—a fraction that increases to 50% and 19%, respectively, upon leptomycin B treatment (Figure 4D).

PDE3A Inhibition Affects HDAC-1 Phosphorylation and Activity in a PKA-Dependent Manner

To test whether PDE3A isoforms control cAMP levels in a nuclear nanodomain involving SMAD4 and HDAC-1, we genetically fused the cAMP FRET reporter CUTie[4] (Figure S10A) to the carboxyl terminus of SMAD4 to generate SMAD4-CUTie (Figure S10B). SMAD4-CUTie showed the expected nuclear localization when expressed in HEK293 cells (Figure S10B) and NRVMs (Figure 5A) and showed kinetics of FRET change comparable to cytosolic CUTie (Figure S10C).

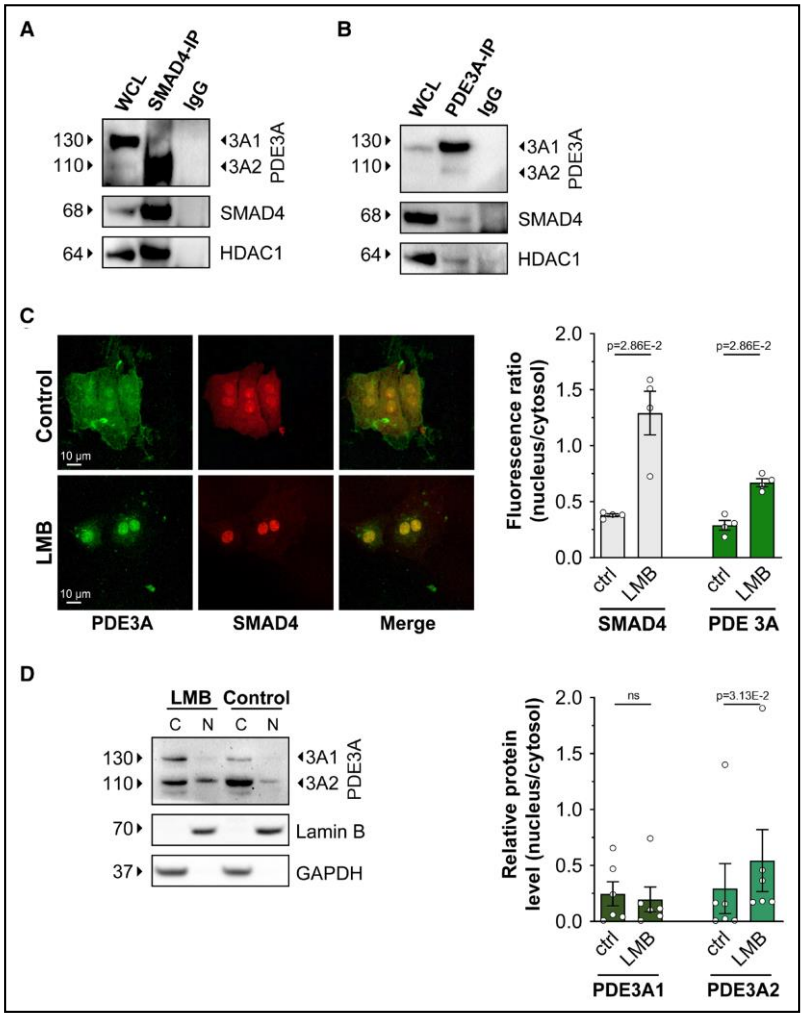

Figure 4. PDE3A (phosphodiesterase 3A) isoforms are in a nuclear complex involving SMAD4 (SMAD family member 4) and HDAC-1 (histone deacetylase 1).
A, Western blot analysis showing PDE3A2 and HDAC-1 in the pull down of endogenous SMAD4 obtained from neonatal rat ventricular myocyte (NRVM) cell lysates. Representative of n=3 independent cultures. **B**, Detection of endogenous SMAD4 and HDAC-1 in the immunoprecipitate obtained by pulling down endogenous PDE3A from NRVM lysates. n=3. **C**, Immunostaining of endogenous PDE3A and SMAD4 in NRVM cells treated either with DMSO (control) or with leptomycin B (LMB; 100 nmol/L) for 3 hours. Quantification of fluorescence intensity is shown on the **right**. n=4 independent experiments (at least 15 cells per experiment). Mann-Whitney *U* test. **D**, Western blot analysis showing endogenous PDE3A1 and PDE3A2 in the nuclear (N) and cytoplasmic (C) fractions obtained from NRVM treated with 100 nmol/L LMB or dimethyl sulfoxide (DMSO) (control) for 3 hours. Densitometric quantification is shown on the **right**. Values are shown as relative to the cytosolic content and are presented as mean±SEM. n=6 biological replicates. Wilcoxon matched pairs signed-rank test. WCL indicates whole-cell lysate.

FRET imaging of NRVM expressing SMAD4-CUTie showed that, in the presence of isoproterenol, inhibition of PDE3 significantly increased cAMP in the immediate proximity of nuclear SMAD4, whereas inhibition of PDE2A had no effect (Figure 5A); this is in contrast to the bulk cytosol, where PDE2A inhibition led to a significantly larger increase in cAMP than inhibition of PDE3 (Figure 5A).

PKA is known to phosphorylate HDAC-1,[41] but the functional effect has not been investigated. To examine whether inhibition of PDE3 results in increased phosphorylation of HDAC-1, NRVMs expressing Flag-tagged

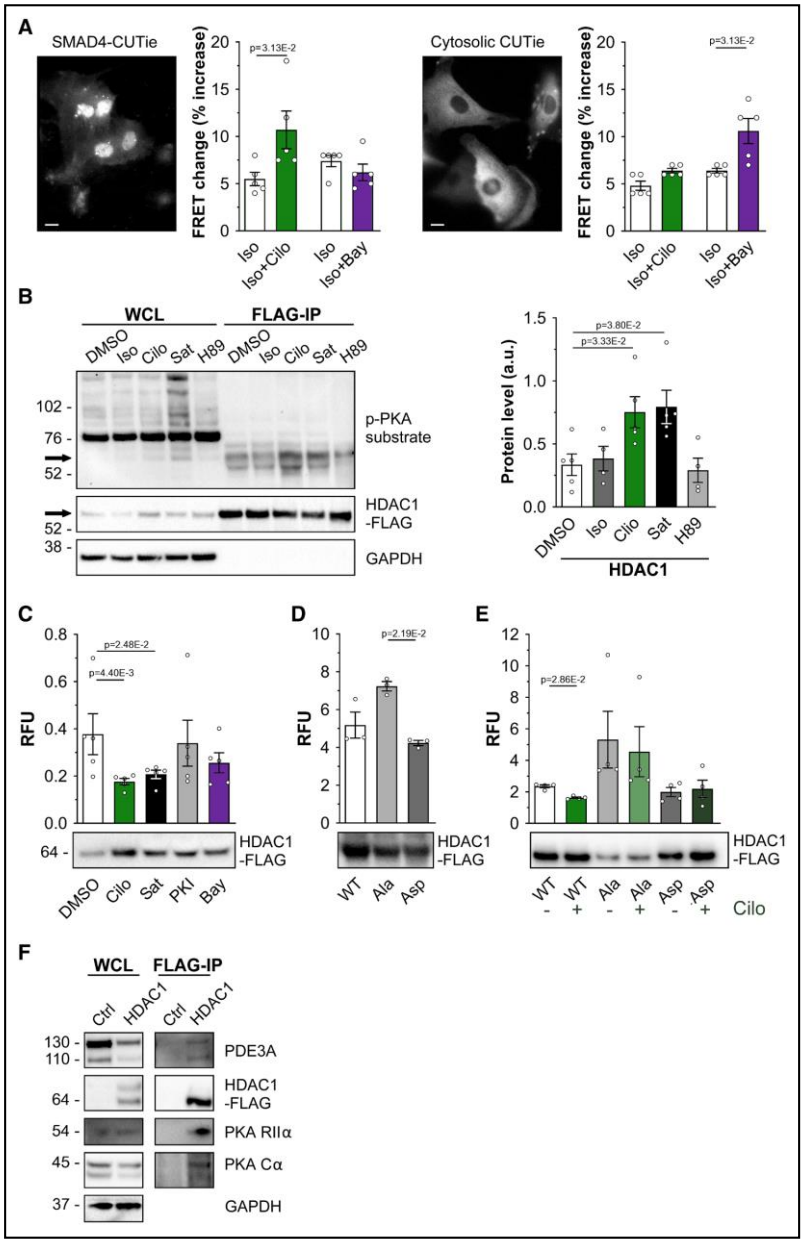

Figure 5. Inhibition of PDE3A (phosphodiesterase 3A) leads to HDAC-1 (histone deacetylase 1) phosphorylation and inhibition of HDAC-1 deacetylase activity.

A, Representative images showing the distribution of SMAD4 (SMAD family member 4)–cAMP universal tag for imaging experiments (CUTie) and CUTie reporters in neonatal rat ventricular myocytes (NRVMs) treated with 100 nmol/L leptomycin B (LMB) for 3 hours. Summaries of the Förster resonance energy transfer (FRET) change detected with the 2 sensors in NRVM on application of 0.5 nmol/L isoproterenol (ISO) followed by 10 µmol/L cilostamide (Cilo) or 100 nmol/L BAY 60-7550 (BAY) are shown on the **right** and are expressed as percent increase over baseline. n=5 independent NRVM preparations. Wilcoxon matched pairs signed-rank test. **B**, Representative Western blot showing PKA (protein kinase A)-dependent phosphorylation of HDAC-1 (**left**) and densitometric analysis of 5 independent experiments (**right**). HDAC-1-Flag was immunoprecipitated from lysates obtained from NRVM treated with 0.5 nmol/L ISO, 10 µmol/L PDE3 inhibitor Cilo, (*Continued*)

HDAC-1 were treated with isoproterenol (0.5 nmol/L), cilostamide (10 µmol/L), or a saturating stimulus (25 µmol/L forskolin and 100 µmol/L IBMX). Analysis of Flag-HDAC-1 pulldowns using a PKA phospho-substrate antibody confirmed a significant increase in HDAC-1 phosphorylation upon inhibition of PDE3, similar to the phosphorylation level achieved at saturating cAMP (Figure 5B). These findings were confirmed in ARVMs (Figure S11A) and in hiPSC-CMs (Figure S11B). The phosphorylation of HDAC-1 on inhibition of PDE3 was completely abolished by inhibition of PKA with PKA inhibitor (PKI) (Figure S11A and S11B). Consistently, overexpression of PDE3A isoforms in HEK293 cells drastically reduced PKA-dependent HDAC-1 phosphorylation (Figure S11C).

We next assessed the effect of PDE3 inhibition on HDAC-1 activity. As shown in Figure 5C, the deacetylase activity measured in HDAC-1-Flag pulldowns obtained from NRVM treated with cilostamide was significantly reduced compared with DMSO control—an effect that was not recapitulated by inhibition of PDE2A with BAY (Figure 5C). In line with these findings, an HDAC-1 phospho-mimic mutant, where the PKA phosphorylation sites are mutated to aspartate (HDAC-$1_{S406D, S436D}$), showed significantly decreased deacetylase activity compared with a phospho-null HDAC-1 mutant, where the same residues are mutated to alanine (HDAC-$1_{S406A, S436A}$; Figure 5D). Consistently, while inhibition of PDE3 significantly reduced WT (wild type) HDAC-1 activity, cilostamide treatment had no effect on the activity of the phospho-mimic or phospho-null HDAC-1 mutants (Figure 5E).

If the PDE3A2/SMAD4/HDAC-1 complex constitutes a nuclear nanodomain where HDAC-1 activity is regulated by a local cAMP pool, PKA is expected to be present within the same complex. Immunoprecipitation experiments using cell lysates from NRVM expressing Flag-HDAC-1 demonstrate that, in addition to PDE3A, both catalytic and regulatory subunits of PKA are present in the immunoprecipitate (Figure 5F). Notably, when we used for this experiment cell lysates from HEK293 cells, which do not express detectable levels of PDE3A endogenously,[10] the regulatory subunit of PKA, but no catalytic subunit, was detected in the HDAC-1 immunoprecipitate (Figure S12). By contrast, both regulatory and catalytic subunits of PKA were present in the immunoprecipitate obtained from HEK293 cells overexpressing PDE3A1 or PDE3A2 (Figure S12), confirming that PDE3A is required at the SMAD4/HDAC-1 nuclear complex to degrade locally cAMP and maintain PKA within the complex in its inactive holoenzyme conformation.

PDE3A Inhibition Regulates GATA4 Expression

To establish whether inhibition of PDE3A affects gene transcription, we treated NRVM with cilostamide and measured the expression level of the transcription factor GATA4, as this is known to be regulated by SMAD4[42,43] and HDAC-1.[44] We found that PDE3 inhibition resulted in upregulation of GATA4 expression, both at the mRNA (Figure 6A) and protein (Figure 6B) levels. Consistently, GATA4 expression was upregulated in heart tissue obtained both from mice where the *PDE3A* gene was ablated by homologous recombination[45] (Figure S13A) and from rats carrying a homozygous frameshift mutation (Δ20 bp) in the *PDE3A* gene that results in a functional deletion phenotype[10] (Figure 6C).

GATA4 is upregulated in response to hypertrophic stimuli, including pressure overload and β-adrenergic activation.[42] We, therefore, assessed whether inhibition of PDE3 may regulate cardiac myocyte hypertrophic growth in an in vitro model of cardiac hypertrophy. We found that treatment with cilostamide was sufficient to significantly increase cardiac myocyte cell size in NRVM (Figure S13B). The prohypertrophic effect of PDE3 inhibition was also confirmed in ARVM (Figure 6D and 6E) and hiPSC-CM (Figure S13C and S13D). Consistent with the observation that PDE3A isoforms control gene expression via interaction with SMAD4 and regulation of a local nuclear pool of cAMP, overexpression of catalytically inactive mutants of PDE3A1 and PDE3A2 (PDE3A1-DN and PDE3A2-DN), which exert a dominant negative effect by displacing the endogenous active counterpart from interacting partners,[46] resulted in significantly higher GATA4 levels compared with expression of the WT enzymes (Figure S13E). Accordingly, PDE3A2-DN was sufficient, per se, to induce hypertrophic growth when expressed in NRVM (Figure S14, as well as in ARVM (Figure 6F) and hiPSC-CM (Figure 6G).

Figure 5 Continued. a saturating cAMP stimulus (Sat, 100 µmol/L 3-isobutyl-1-methylxanthine [IBMX] and 25 µmol/L forskolin), or with 30 µmol/L PKA inhibitor H89. Phosphorylation level was detected with a phospho-PKA substrate antibody. For quantification, values were normalized to the amount of HDAC-Flag in the immunoprecipitates and are presented as mean±SEM. Kruskal-Wallis test with Dunn correction for multiple comparisons. **C**, Deacetylase activity of HDAC-1-Flag immunoprecipitated from NRVMS cells treated for 45 minutes with 10 µmol/L Cilo (Sat, 20 µmol/L cell-permeable PKA inhibitor [PKI]) or 1 µmol/L BAY. HDAC-1 activity is normalized to the relative amount of HDAC-1-Flag present in every sample (as shown in a representative Western blot in the **bottom**) and is presented as mean±SEM. n=5 biological replicates. Kruskal-Wallis test with Dunn correction for multiple comparisons. **D**, Deacetylase activity measured in HDAC-1-Flag pull downs obtained from Human Embryonic Kidney cells 293 (HEK293) expressing wild type (WT) HDAC-1-Flag and the mutants HDAC-$1_{S406A, S436A}$-Flag (Ala) or HDAC-$1_{S406D, S436D}$-Flag (Asp). Quantification as in **C**. n=3 independent experiments. Kruskal-Wallis test with Dunn correction for multiple comparisons. **E**, Deacetylase activity measured in HDAC-1-Flag pull downs obtained from NRVM expressing WT, Ala, or Asp mutants. Quantification as in **C**. n=4 independent experiments. Mann-Whitney *U* test. **F**, Western blot analysis showing PDE3A, PKA regulatory (RIIα) and catalytic (Cα) subunits in the FLAG pull down obtained from lysates of NRVM expressing HDAC-1-Flag. Representative of 3 independent experiments. RFU indicates relative fluorescence unit.

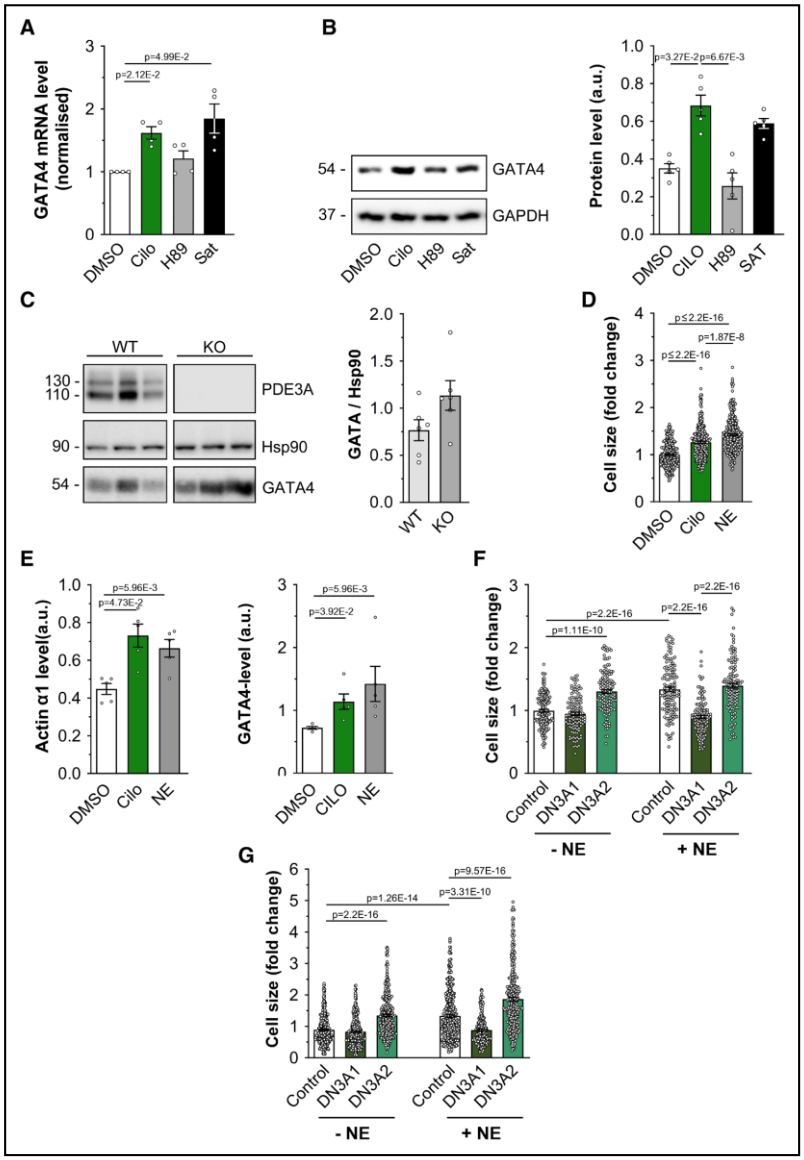

Figure 6. Inhibition of PDE3A (phosphodiesterase 3A) regulates GATA4 (GATA4 binding protein 4) expression.
A, Quantitative real-time polymerase chain reaction analysis of GATA4 mRNA transcripts in neonatal rat ventricular myocyte (NRVM) cells treated with 10 µM cilostamide (Cilo), saturating treatment (Sat, 100 µmol/L 3-isobutyl-1-methylxanthine [IBMX] and 25 µmol/L forskolin) or 30 µmol/L H89 for 2.5 hours. Bars show GATA4 mRNA values normalized to GAPDH and dimethyl sulfoxide (DMSO) treatment and are presented as mean±SEM. n=4 biological replicates. Kruskal-Wallis test with Dunn correction for multiple comparisons. **B**, Western blot analysis and quantification of GATA4 protein expression in NRVM cells treated with Cilo (10 µmol/L), H89 (30 µmol/L), or saturating treatment. GAPDH served as a loading control. Values are normalized to GAPDH and are presented as mean±SEM. n=5 biological replicates. Kruskal-Wallis test with Dunn correction for multiple comparisons. **C**, Western blot analysis and quantification of endogenous GATA4 expression in cardiac tissue lysates obtained from PDE3A knockout or wild-type control rats. Hsp90 served as a loading control and for normalization in the quantification. Values are mean±SEM. n=6 biological replicates. Mann-Whitney *U* test. **D**, Cell size measured in adult rat ventricular myocytes (ARVMs) either untreated or treated with Cilo (10 mmol/L) or NE (10 µmol/L) for 24 hours. Values are normalized to DMSO control and expressed as mean±SEM. n=5 independent experiments (at least 241 cells per condition). Normality of log-transformed data was tested with Anderson-Darling test. (*Continued*)

Unexpectedly, expression of PDE3A1-DN showed no effect on the size of otherwise untreated cardiac myocytes (Figure S14; Figure 6F and 6G) while it completely reversed the hypertrophy induced by norepinephrine—a well-established prohypertrophic stimulus (Figure S14; Figure 6F and 6G). These findings suggest that displacement of PDE3A1 from locations distinct from the SMAD4/HDAC-1 complex overrides the effect of any displacement of PDE3A from the nuclear SMAD4/HDAC-1 nanodomain and triggers instead a response that inhibits norepinephrine-induced hypertrophic growth.

PDE3 Inhibition Leads to Hypertrophy via Regulation of HDAC-1 Phosphorylation

Histone deacetylation by HDACs is generally associated with repression of gene expression.[47] Consistently, HDAC-1 overexpression in NRVM resulted in decreased GATA4 expression (Figure 7A). This effect was counteracted by inhibition of PDE3A in a PKA-dependent fashion (Figure 7B). Further confirming that PKA-dependent phosphorylation inhibits HDAC-1 activity with impact on gene transcription, NRVM expressing the phospho-mimic HDAC-1$_{S406D, S436D}$ mutant showed significantly higher GATA4 expression compared with cells expressing the phospho-null HDAC-1$_{S406A, S436A}$ mutant (Figure 7C). Notably, overexpression of the phospho-null HDAC-1$_{S406A, S436A}$ mutant completely blocked the effect of cilostamide or norepinephrine on hypertrophic growth, whereas overexpression of the phospho-mimic HDAC-1$_{S406D, S436D}$ mutant was sufficient per se to induce hypertrophy, to a similar degree as cilostamide or norepinephrine (Figure 7D), confirming that the effect of PDE3A inhibition on cardiac myocyte size relies on the PKA-dependent phosphorylation of HDAC-1.

DISCUSSION

Cardiac myocytes express >100 different GPCRs (G-protein–coupled receptors), many of which regulate cell function primarily via the generation of cAMP.[48] Specificity of response is achieved via subcellular compartmentalization where PDEs play a key role by differentially hydrolyzing cAMP and generating multiple nanodomains with different cAMP concentration. The functional relevance of cAMP compartmentalization is illustrated in the heart by the ability of cAMP to relay sympathetic signals with exacting precision and no interference from the myriad of other cAMP-modulated processes that are independent of, but run concurrently with, β-adrenergic regulation of cardiac myocyte contraction and relaxation.[49,50] Spillage of information among these parallel pathways is avoided through coordinated spatial and temporal regulation of the multiple coexisting cAMP nanodomains.

Only a limited number of cardiac cAMP nanodomains, which primarily involve some of the prototypical cardiac targets of β-adrenergic stimulation, have been characterized so far, leaving the global landscape of subcellular cAMP nanodomain largely undefined. Genetically encoded fluorescent reporters have recently provided unequivocal evidence that the size of subcellular cAMP nanodomains is below the resolution of optical microscopy.[4–6] Visualization of cAMP domains, therefore, relies on the ability to target the cAMP probe within the domain itself,[4,8,18] making identification and characterization of novel cAMP nanodomains difficult when previous knowledge of their subcellular location is not available.

To overcome this limitation, and with the view that individual PDEs can serve as signposts to denote nanodomains with distinct regulation of cAMP, we adopted a proteomics approach that integrates the analysis of the interactome of a specific PDE isoform with the analysis of the phosphoproteome associated with inhibition of that PDE to identify previously unknown cAMP nanodomains associated with sympathetic signaling. We focused on PDE3A-regulated nanodomains, anticipating that knowledge of where these domains are located may help identify pathways involved in the long-term adverse cardiac effects observed in patients with HF receiving PDE3 inhibitors. For comparison, we investigated the nanodomains associated with PDE2A2, the inhibition of which has been associated with cardioprotective effects.[46,51] Our analysis demonstrates that these PDEs operate largely in distinct subcellular locations and, therefore, define sites undergoing unique regulation of cAMP. In addition to providing information on the subcellular location, this strategy has the advantage of revealing molecular cues that can be useful to inform further mechanistic studies to establish the function associated with specific nanodomains. In addition, by integrating information on the identity of PDE binding partners with information on the identity of PDE phosphorylation targets, this approach reveals nonobvious interactions that could go unnoticed or be neglected. Extended to other

Figure 6 Continued. *P* values were determined by a hierarchical significance test using log-transformed data followed by Bonferroni correction. **E**, Quantification by Western blot analysis of hypertrophy markers protein expression level in samples as shown in **D**. n=5 independent experiments. Kruskal-Wallis test with Dunn's correction. **F**, Cell size measured in ARVM expressing mCherry (control) or the catalytically inactive mutant PDE3A1-DN-RFP or PDE3A2-DN-RFP (**left**) and treated as indicated for 24 hours. n=5 independent experiments (at least 53 cells per condition). Normality was established by the Anderson-Darling test. Hierarchical significance analysis with final Bonferroni correction for multiple comparisons. **G**, Cell size measured in human induced pluripotent stem cell-derived cardiomyocytes (hiPSC-CM) expressing mCherry (control) or the catalytically inactive mutant PDE3A1-DN-RFP or PDE3A2-DN-RFP (**left**) and treated as indicated for 48 hours. n=6 independent experiments (6 different differentiations of 3 independent hiPSC lines, at least 231 cells per condition). *P* values were determined by hierarchical significance test using log-transformed data followed by Bonferroni correction.

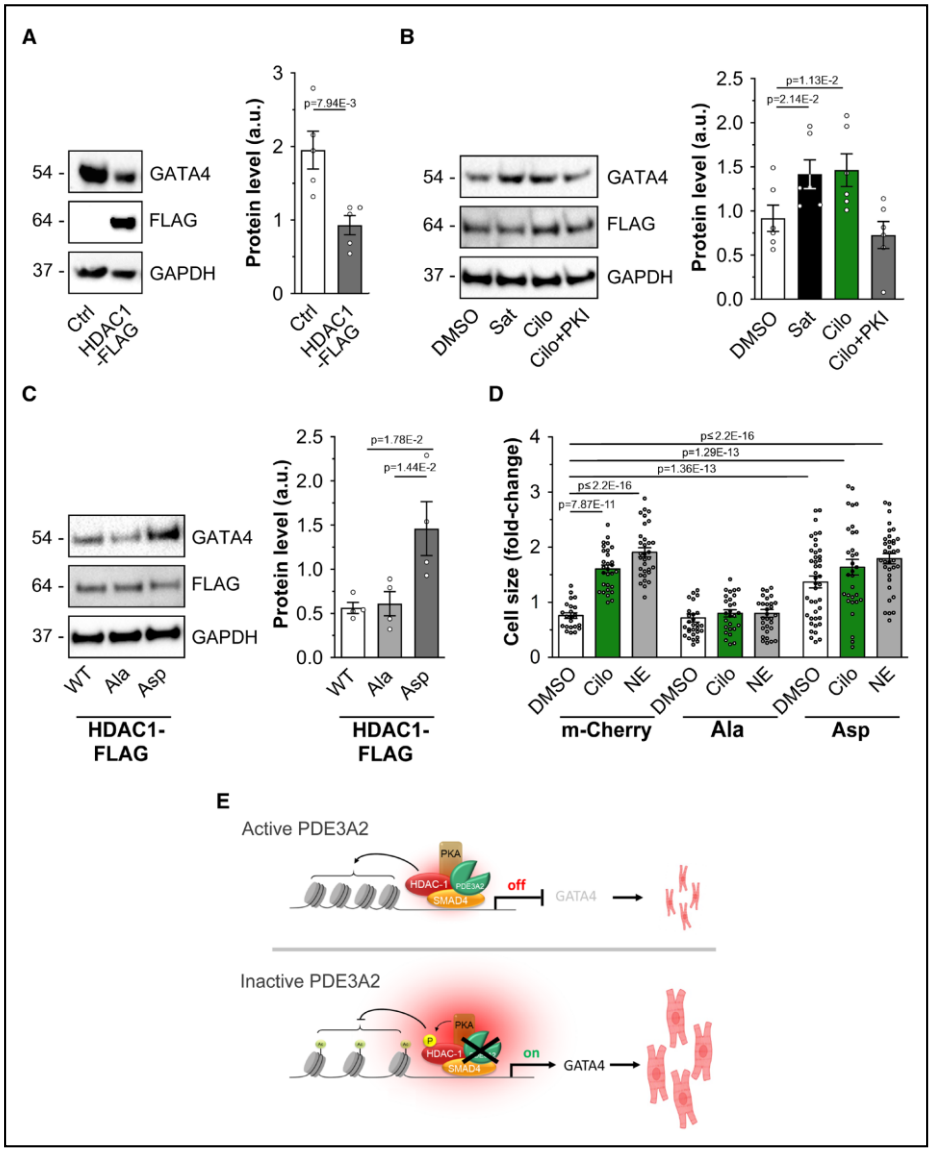

Figure 7. Inhibition of PDE3A (phosphodiesterase 3A) affects cardiac myocyte hypertrophic growth.
A, Western blot analysis and densitometric quantification of GATA4 (GATA binding protein 4) expression in cells overexpressing HDAC-1 (histone deacetylase 1)-Flag. Values are normalized to GAPDH and presented as mean±SEM. n=5 biological replicates. Mann-Whitney *U* test. **B**, Western blot analysis and quantification showing expression of GATA4 in neonatal rat ventricular myocyte (NRVM) cells overexpressing HDAC-1-Flag and treated with cilostamide (Cilo; 10 µmol/L), saturating cAMP (Sat, 100 µmol/L 3-isobutyl-1-methylxanthine [IBMX] and 25 µmol/L forskolin) of PKA inhibitor (PKI; 20 µmol/L). n=6 biological replicates. Values are normalized to GAPDH and to Flag signal and are presented as mean±SEM. Friedman test and Dunn correction for multiple comparisons. **C**, Western blot analysis and quantification showing expression of GATA4 in NRVM cells overexpressing HDAC-1-Flag (wild type [WT]), the phospho-null mutant HDAC-$1_{S406A-S436A}$-Flag (Ala), or the phospho-mimic mutant HDAC-$1_{S406D-S436D}$-Flag (Asp). GAPDH was used as a loading control. For quantification, values were normalized to GAPDH and Flag signal and are expressed as means±SEM. n=5 independent experiments. Kruskal-Wallis test with Dunn's correction for multiple comparisons. **D**, Cell size measured in NRVM expressing mCherry, HDAC-$1_{S406A-S436A}$-Flag (S>A), or HDAC-$1_{S406D-S436D}$-Flag (S>D) and treated with DMSO, Cilo (10 µmol/L), or NE (10 µmol/L) for 48 hours. Values are expressed as fold change relative to untransfected and dimethyl sulfoxide (DMSO) treated within the same transfection group and are presented as mean±SEM. n=6 independent experiments (*Continued*)

PDE isoforms, this strategy can define the full topography of cAMP nanodomains associated with β-adrenergic stimulation in cardiac myocytes. A similar approach can be applied to dissect the cAMP nanodomain landscape associated with other GPCRs and ligands and to establish how cAMP nanodomains are affected in pathological conditions. Given the ubiquitous role of cAMP signaling in all organs and systems, the same strategy is applicable to dissect local cAMP signaling in other cell types.

Our investigation yielded a set of individual proteins that are simultaneously present in the interactome and in the phosphoproteome associated specifically with either PDE3A or PDE2A, strongly indicating that these proteins pinpoint specific cAMP nanodomains; validation of these nanodomains is currently undergoing. To capture additional PDE3A-dependent cAMP nanodomains, we exploited GOCC annotation and found that the term nucleus was highly enriched in both PDE3A1 and PDE3A2 interactomes and in the cilostamide-associated phosphoproteome. Among the nucleus-annotated proteins, we selected the CtBP2, phospho-HDAC-1, and SMAD4 interaction for further analysis as these proteins form a complex that acts downstream of TGF-β (transcription growth factor beta).[52–55] Notably, TGF-β is associated with cardiac hypertrophy, fibrosis, and conduction abnormalities,[43,56] all features that characterize the long-term detrimental effect that PDE3 inhibitors have in patients with HF. Collectively, our results demonstrate the presence of a cAMP nanodomain localized to the nucleus of cardiac myocytes where PDE3A2 forms a complex with SMAD4 and HDAC-1. The local increase in cAMP elicited by PDE3 inhibition enhances PKA-dependent phosphorylation of HDAC-1 and inhibition of its deacetylase activity. This results in derepression of prohypertrophic gene transcription and cardiac myocyte hypertrophy (Figure 7C). Previous studies suggest that enhanced apoptosis mediated by ICER (inducible cAMP early repressor) contributes to the adverse effects of PDE3 inhibition.[57] Although ICER does not appear in the PDE3A interactomes identified in this study, HDAC-1 recruitment has been associated with ICER repressor activity.[58] It is, therefore, possible that a nuclear nanodomain that includes HDAC-1 controls both the prohypertrophic and proapoptotic effects of PDE3 inhibition and that both these effects participate in the progression of adverse cardiac remodeling. Our observation that the PDE3A2/SMAD4/HDAC-1 nanodomain also operates in human cardiac myocytes differentiated from 4 independent pluripotent stem cell lines indicates that this pathway may contribute to the negative long-term clinical outcome observed in patients with HF receiving PDE3 inhibitors. In support of the relevance of the nuclear PDE3A2/SMAD4/HDAC-1 nanodomain in vivo, a recent characterization of the PDE3A functional deletion rat model[10] shows that, upon chronic β-AR challenge, the same degree of cardiac remodeling is observed in knockout and in WT rats, despite the knockout animals displaying significantly lower blood pressure (Figure S15),[59] indicating that, in vivo, loss of PDE3A sensitizes the animals to cardiac stress.

The findings presented here provide an explanation for the apparently conflicting data on the role of PDE3A in heart disease, where both elevation[60] and reduction[57] of PDE3A expression and activity have been associated with HF and both ablation[60] and overexpression[57] of PDE3A isoforms have been reported to provide cardioprotective effects. Most studies so far have not investigated the role of specific PDE3A isoforms in cardiac disease, and it will be interesting to explore in the future whether the changes in the level of PDE3A expression associated with HF involve individual isoforms. Cardiac overexpression of PDE3A1 has been reported to associate with cardiac remodeling but also to confer cardioprotection to ischemia-reperfusion.[61] Our results indicate that these opposing effects could be mediated by PDE3A1 regulating cAMP at multiple nanodomains. Our findings also indicate that overexpression may force interactions that, although possible, do not occur when the protein is expressed at an endogenous level. PDE3A1 and PDE3A2 are expressed from the same gene from alternative start sites, and their amino acid sequence is identical except for a unique N-terminal domain in PDE3A1.[62] We find that, when overexpressed, PDE3A1 can interact with SMAD4/HDAC-1, suggesting that this interaction involves the conserved C-terminal sequence shared by PDE3A1 and PDE3A2. Consistently, overexpression of PDE3A1-DN, which only differs from the WT counterpart by 2 amino acid substitutions in the catalytic site, can displace endogenous PDE3A2 from the SMAD4/HDAC-1 complex and enhance GATA4 expression (Figure S13E). However, when expressed at endogenous levels, PDE3A1 is not associated with SMAD4/HDAC-1. Our findings show that endogenous PDE3A1 controls cAMP at sites distinct from the SMAD4/HDAC-1 nuclear complex and that ≥1 of these sites are associated with antihypertrophic effects. Displacement of PDE3A1 from those locations has a dominant effect over displacement of PDE3A2 from the SMAD4/HDAC-1 domain, as demonstrated by the complete

Figure 7 Continued. (6 different differentiations from 3 independent human induced pluripotent stem cell lines, at least 27 cells per condition). Anderson-Darling log normality test and hierarchical analysis of log-transformed data followed by Bonferroni correction. **E**, Schematic illustration of the PDE3A/SMAD4 (SMAD family member 4)/HDAC-1 nuclear ND. **Top**, With active PDE3A2 at the SMAD4/HDAC-1 nuclear complex cAMP levels are locally low and PKA (protein kinase A) is inactive. HDAC-1 deacetylates histones, repressing expression of prohypertrophic genes. **Bottom**, Inhibition of PDE3A or displacement of PDE3A2 results in a local increase in cAMP, activation of local PKA, and phosphorylation of HDAC-1, leading to inhibition of its deacetylase activity. As a result, transcription of prohypertrophic genes is enhanced, leading to cardiac myocyte hypertrophy. Some elements used in **E** have been generated using BioRender.com.

reversal of hypertrophy we observe on overexpression of PDE3A1-DN. By contrast, overexpression of PDE3A2-DN does not displace endogenous PDE3A1 from the locations that protect from hypertrophy. This suggests that anchoring of PDE3A1 at those extranuclear sites involves its unique N-terminal domain. Further studies will be necessary to identify the location associated with the protective effect of PDE3A1 displacement, and the PDE3A1-selective nanodomains identified in this study by our integrated proteomics analysis provides a list of candidates for these investigations. The identification of these sites may open the possibility to selectively modulate cAMP at those sites, with potential therapeutic applications.

Recent studies have challenged the classic paradigm that PKA-dependent regulation of gene expression relies on cytosolic activation of PKA and subsequent diffusion of active catalytic subunits to the nucleus by providing evidence of a nuclear subset of PKA holoenzyme[63,64] that responds to a nuclear pool of cAMP,[65] although proof that this nuclear cAMP/PKA domain regulates gene transcription has been lacking. Our work significantly expands our understanding of PKA signaling and regulation by providing direct evidence that a nuclear cAMP/PKA domain under the control of PDE3A2 controls expression of prohypertrophic genes. Notably, our data show that the PDE3A activity at the SMAD4/HDAC-1 nanodomain is sufficient to prevent phosphorylation of HDAC-1 in response to subnanomolar concentrations of isoproterenol (Figure 5B; Figure S11B). This indicates that PDE3A2 at this site provides a local shielding mechanism that protects cardiac myocytes from hypertrophic growth when β-adrenergic stimulation executes the physiological control of cardiac contraction and relaxation.

ARTICLE INFORMATION

Received May 30, 2022; revision received February 28, 2023; accepted March 1, 2023.

Affiliations

Department of Physiology, Anatomy and Genetics (G.S., K.S., D.K., A.Z., M.F., Y.-C.C., N.C.S., A.K., J.H., K.C.P., M.Z.) and Department of Biochemistry (S.H., S.M.), University of Oxford, United Kingdom. Now with Neuroscience Institute, National Research Council of Italy (CNR), Padova (N.C.S.). Biomolecular Mass Spectrometry and Proteomics, Utrecht Institute for Pharmaceutical Sciences and Bijvoet Center for Biomolecular Research, Utrecht University, the Netherlands (D.K., A.S., A.J.R.H.). Centre for Vaccine Development, Institute of Molecular Biosciences, Mahidol University, Thailand (D.K.). Max-Delbrück-Center for Molecular Medicine in the Helmholtz Association and German Centre for Cardiovascular Research, Partner Site Berlin (M.E., A.S., E.K.). Department of Anatomy and Embryology, Leiden University Medical Center, the Netherlands (V.M., M.B.). Department of Biology, University of Padua, Italy (M.B.). Veneto Institute of Molecular Medicine, Padua, Italy (M.B.). Cancer Research UK Beatson Institute, Glasgow, United Kingdom (S.Z.). Institute of Cancer Sciences, University of Glasgow, United Kingdom (S.Z.). Oxford NIHR Biomedical Research Centre (M.Z.).

Acknowledgments

PDE3A (phosphodiesterase 3A) knockout mouse heart tissue was a kind gift from Dr Joel Moss (National Heart, Lung, and Blood Institute, Bethesda) and Dr Alex KleinJan (Erasmus MC, Rotterdam). The M180 and M398 human induced pluripotent stem cell lines were a kind gift from Dr Christian Pinset (Center for the Study of Stem Cells/Institute for Stem cell Therapy and Exploration of Monogenic diseases, Corbeil Essonnes).

Author Contributions

G. Subramaniam, K. Schleicher, D. Kovanich, and M. Zaccolo designed the experiments. G. Subramaniam, K. Schleicher, D. Kovanich, A. Zerio, M. Folkmanaite, N.C. Surdo, M. Ercu, A. Koschinski, V. Meraviglia, Y.-C. Chao, A. Sholokh, and K. Chan Park performed the experiments and analyzed data. A. Koschinski, A. Sholokh, A.J.R. Heck, E. Klussmann, M. Bellin, S. Zanivan, S. Hester, S. Mohammed, J. Hu, and M. Zaccolo analyzed data; G. Subramaniam, K. Schleicher, and M. Zaccolo wrote the manuscript. M. Zaccolo conceived the research question and oversaw the entirety of research.

Sources of Funding

This study was supported by grants from the British Heart Foundation (BHF; PG/15/5/31110 and RG/17/6/32944) and the BHF Centre of Research Excellence, Oxford (RE/13/1/30181, RE/18/3/34214, and RE/18/3/34214) and the Oxford NIHR Biomedical Research Centre to M. Zaccolo; the Horizon 2020 project Epic-XS (823839) to A.J.R. Heck; the Deutsche Forschungsgemeinschaft (program project grant, 394046635–SFB 1365) and the German Israeli Foundation (I-1452-203/13-2018) to E. Klussmann; the Netherlands Organisation for Health Research and Development ZonMW (MKMD project No. 114022504) and the European Research Council (ERC-CoG 101001746 Mini-HEART) to M. Bellin; and the Stand Up to Cancer campaign for Cancer Research UK grant A29800 to S. Zanivan.

Disclosures

None.

REFERENCES

1. Maurice DH, Ke H, Ahmad F, Wang Y, Chung J, Manganiello VC. Advances in targeting cyclic nucleotide phosphodiesterases. *Nat Rev Drug Discov*. 2014;13:290–314. doi: 10.1038/nrd4228
2. Kokkonen K, Kass DA. Nanodomain regulation of cardiac cyclic nucleotide signaling by phosphodiesterases. *Annu Rev Pharmacol Toxicol*. 2017;57:455–479. doi: 10.1146/annurev-pharmtox-010716-104756
3. Zaccolo M, Zerio A, Lobo MJ. Subcellular organization of the cAMP signaling pathway. *Pharmacol Rev*. 2021;73:278–309. doi: 10.1124/pharmrev.120.000086
4. Surdo NC, Berrera M, Koschinski A, Brescia M, Machado MR, Carr C, Wright P, Gorelik J, Morotti S, Grandi E, et al. FRET biosensor uncovers cAMP nanodomains at beta-adrenergic targets that dictate precise tuning of cardiac contractility. *Nat Commun*. 2017;8:15031. doi: 10.1038/ncomms15031
5. Bock A, Annibale P, Konrad C, Hannawacker A, Anton SE, Maiellaro I, Zabel U, Sivaramakrishnan S, Falcke M, Lohse MJ. Optical mapping of cAMP signaling at the nanometer scale. *Cell*. 2020;182:1519–1530.e17. doi: 10.1016/j.cell.2020.07.035
6. Zhang JZ, Lu TW, Stolerman LM, Tenner B, Yang JR, Zhang JF, Falcke M, Rangamani P, Taylor SS, Mehta S, et al. Phase separation of a PKA regulatory subunit controls cAMP compartmentation and oncogenic signaling. *Cell*. 2020;182:1531–1544.e15. doi: 10.1016/j.cell.2020.07.043
7. Anton SE, Kayser C, Maiellaro I, Nemec K, Moller J, Koschinski A, Zaccolo M, Annibale P, Falcke M, Lohse MJ, et al. Receptor-associated independent camp nanodomains mediate spatiotemporal specificity of GPCR signaling. *Cell*. 2022;185:1130–1142.e11. doi: 10.1016/j.cell.2022.02.011
8. Sprenger JU, Perera RK, Steinbrecher JH, Lehnart SE, Maier LS, Hasenfuss G, Nikolaev VO. In vivo model with targeted camp biosensor reveals changes in receptor-microdomain communication in cardiac disease. *Nat Commun*. 2015;6:6965. doi: 10.1038/ncomms7965
9. Bers DM, Xiang YK, Zaccolo M. Whole-cell cAMP and PKA activity are epiphenomena, nanodomain signaling matters. *Physiology (Bethesda)*. 2019;34:240–249. doi: 10.1152/physiol.00002.2019
10. Ercu M, Marko L, Schachterle C, Tsvetkov D, Cui Y, Maghsodi S, Bartolomaeus TUP, Maass PG, Zühlke K, Gregersen N, et al. Phosphodiesterase 3a and arterial hypertension. *Circulation*. 2020;142:133–149. doi: 10.1161/CIRCULATIONAHA.119.043061
11. Fukuta H, Goto T, Wakami K, Kamiya T, Ohte N. Effect of beta-blockers on heart failure severity in patients with heart failure with preserved ejection fraction: a meta-analysis of randomized controlled trials. *Heart Fail Rev*. 2021;26:165–171. doi: 10.1007/s10741-020-10013-5
12. Amsallem EK, Haddour G, Boissel JP, Nony P. Phosphodiesterase iii inhibitors for heart failure. *Cochrane Database Syst Rev*. 2005;2005:CD002230. doi: 10.1002/14651858.CD002230.pub2

13. Omar MH, Scott JD. AKAP signaling islands: venues for precision pharmacology. *Trends Pharmacol Sci*. 2020;41:933–946. doi: 10.1016/j.tips.2020.09.007
14. Baillie GS, Tejeda GS, Kelly MP. Therapeutic targeting of 3',5'-cyclic nucleotide phosphodiesterases: inhibition and beyond. *Nat Rev Drug Discov*. 2019;18:770–796. doi: 10.1038/s41573-019-0033-4
15. Dema A, Perets E, Schulz MS, Deak VA, Klussmann E. Pharmacological targeting of AKAP-directed compartmentalized cAMP signaling. *Cell Signal*. 2015;27:2474–2487. doi: 10.1016/j.cellsig.2015.09.008
16. Wechsler J, Choi YH, Krall J, Ahmad F, Manganiello VC, Movsesian MA. Isoforms of cyclic nucleotide phosphodiesterase pde3a in cardiac myocytes. *J Biol Chem*. 2002;277:38072–38078. doi: 10.1074/jbc.M203647200
17. Lomas O, Brescia M, Carnicer R, Monterisi S, Surdo NC, Zaccolo M. Adenoviral transduction of FRET-based biosensors for camp in primary adult mouse cardiomyocytes. *Methods Mol Biol*. 2015;1294:103–115. doi: 10.1007/978-1-4939-2537-7_8
18. Zaccolo M, Pozzan T. Discrete microdomains with high concentration of cAMP in stimulated rat neonatal cardiac myocytes. *Science*. 2002;295:1711–1715. doi: 10.1126/science.1069982
19. Meraviglia V, Arendzen CH, Tok M, Freund C, Maione AS, Sommariva E, Bellin M. Generation of human induced pluripotent stem cell line LUMCi027-a and its isogenic gene-corrected line from a patient affected by arrhythmogenic cardiomyopathy and carrying the c.2013delc pkp2 mutation. *Stem Cell Res*. 2020;46:101835. doi: 10.1016/j.scr.2020.101835
20. Giacomelli E, Meraviglia V, Campostrini G, Cochrane A, Cao X, van Helden RWJ, Krotenberg Garcia A, Mircea M, Kostidis S, Davis RP, et al. Human-iPSC-derived cardiac stromal cells enhance maturation in 3D cardiac microtissues and reveal non-cardiomyocyte contributions to heart disease. *Cell Stem Cell*. 2020;26:862–879.e11. doi: 10.1016/j.stem.2020.05.004
21. Massourides E, Polentes J, Mangeot PE, Mournetas V, Nectoux J, Deburgrave N, Nusbaum P, Leturcq F, Popplewell L, Dickson G, et al. Dp412e: a novel human embryonic dystrophin isoform induced by BMP4 in early differentiated cells. *Skelet Muscle*. 2015;5:40. doi: 10.1186/s13395-015-0062-6
22. Campostrini G, Meraviglia V, Giacomelli E, van Helden RWJ, Yiangou L, Davis RP, Bellin M, Orlova VV, Mummery CL. Generation, functional analysis and applications of isogenic three-dimensional self-aggregating cardiac microtissues from human pluripotent stem cells. *Nat Protoc*. 2021;16:2213–2256. doi: 10.1038/s41596-021-00497-2
23. Cox J, Mann M. Maxquant enables high peptide identification rates, individualized p.P.B.-range mass accuracies and proteome-wide protein quantification. *Nat Biotechnol*. 2008;26:1367–1372. doi: 10.1038/nbt.1511
24. Tyanova S, Temu T, Sinitcyn P, Carlson A, Hein MY, Geiger T, Mann M, Cox J. The perseus computational platform for comprehensive analysis of (prote)omics data. *Nat Methods*. 2016;13:731–740. doi: 10.1038/nmeth.3901
25. Hulsen T, de Vlieg J, Alkema W. Biovenn - a web application for the comparison and visualization of biological lists using area-proportional venn diagrams. *BMC Genomics*. 2008;9:488. doi: 10.1186/1471-2164-9-488
26. Bindea G, Mlecnik B, Hackl H, Charoentong P, Tosolini M, Kirilovsky A, Fridman W-H, Pagès F, Trajanoski Z, Galon J. Cluego: a cytoscape plug-in to decipher functionally grouped gene ontology and pathway annotation networks. *Bioinformatics*. 2009;25:1091–1093. doi: 10.1093/bioinformatics/btp101
27. Szklarczyk D, Gable AL, Lyon D, Junge A, Wyder S, Huerta-Cepas J, Simonovic M, Doncheva NT, Morris JH, Bork P, et al. String v11: protein-protein association networks with increased coverage, supporting functional discovery in genome-wide experimental datasets. *Nucleic Acids Res*. 2019;47:D607–D613. doi: 10.1093/nar/gky1131
28. Schneider CA, Rasband WS, Eliceiri KW. NIH image to imagej: 25 years of image analysis. *Nat Methods*. 2012;9:671–675. doi: 10.1038/nmeth.2089
29. Livak KJ, Schmittgen TD. Analysis of relative gene expression data using real-time quantitative PCR and the 2(-delta delta c(t)) method. *Methods*. 2001;25:402–408. doi: 10.1006/meth.2001.1262
30. Sikkel MB, Francis DP, Howard J, Gordon F, Rowlands C, Peters NS, Lyon AR, Harding SE, MacLeod KT. Hierarchical statistical techniques are necessary to draw reliable conclusions from analysis of isolated cardiomyocyte studies. *Cardiovasc Res*. 2017;113:1743–1752. doi: 10.1093/cvr/cvx151
31. Klarenbeek J, Goedhart J, van Batenburg A, Groenewald D, Jalink K. Fourth-generation EPAC-based FRET sensors for cAMP feature exceptional brightness, photostability and dynamic range: characterization of dedicated sensors for FLIM, for ratiometry and with high affinity. *PLoS One*. 2015;10:e0122513. doi: 10.1371/journal.pone.0122513
32. Golkowski M, Shimizu-Albergine M, Suh HW, Beavo JA, Ong SE. Studying mechanisms of cAMP and cyclic nucleotide phosphodiesterase signaling in Leydig cell function with phosphoproteomics. *Cell Signal*. 2016;28:764–778. doi: 10.1016/j.cellsig.2015.11.014
33. Humphrey SJ, Yang G, Yang P, Fazakerley DJ, Stockli J, Yang JY, James DE. Dynamic adipocyte phosphoproteome reveals that AKT directly regulates MTORC2. *Cell Metab*. 2013;17:1009–1020. doi: 10.1016/j.cmet.2013.04.010
34. Monterisi S, Lobo MJ, Livie C, Castle JC, Weinberger M, Baillie G, Surdo NC, Musheshe N, Stangherlin A, Gottlieb E, et al. Pde2a2 regulates mitochondria morphology and apoptotic cell death via local modulation of cAMP/PKA signaling. *Elife*. 2017;6:e21374. doi: 10.7554/eLife.21374
35. Beltejar MG, Lau HT, Golkowski MG, Ong SE, Beavo JA. Analyses of PDE-regulated phosphoproteomes reveal unique and specific cAMP-signaling modules in t cells. *Proc Natl Acad Sci USA*. 2017;114:E6240–E6249. doi: 10.1073/pnas.1703939114
36. Ahmad F, Shen W, Vandeput F, Szabo-Fresnais N, Krall J, Degerman E, Goetz F, Klussmann E, Movsesian M, Manganiello V. Regulation of sarcoplasmic reticulum ca2+ atpase 2 (serca2) activity by phosphodiesterase 3a (pde3a) in human myocardium: phosphorylation-dependent interaction of pde3a1 with serca2. *J Biol Chem*. 2015;290:6763–6776. doi: 10.1074/jbc.M115.638585
37. Beca S, Ahmad F, Shen W, Liu J, Makary S, Polidovitch N, Sun J, Hockman S, Chung YW, Movsesian M, et al. Phosphodiesterase type 3a regulates basal myocardial contractility through interacting with sarcoplasmic reticulum calcium atpase type 2a signaling complexes in mouse heart. *Circ Res*. 2013;112:289–297. doi: 10.1161/CIRCRESAHA.111.300003
38. Richards MA, Simon JN, Ma R, Loonat AA, Crabtree MJ, Paterson DJ, Fahlman RP, Casadei B, Fliegel L, Swietach P. Nitric oxide modulates cardiomyocyte ph control through a biphasic effect on sodium/hydrogen exchanger-1. *Cardiovasc Res*. 2020;116:1958–1971. doi: 10.1093/cvr/cvz311
39. Mohamed TMA, Oceandy D, Zi M, Prehar S, Alatwi N, Wang Y, Shaheen MA, Abou-Leisa R, Schelcher C, Hegab Z, et al. Plasma membrane calcium pump (pmca4)-neuronal nitric-oxide synthase complex regulates cardiac contractility through modulation of a compartmentalized cyclic nucleotide microdomain. *J Biol Chem*. 2011;286:41520–41529. doi: 10.1074/jbc.M111.290411
40. Pierreux CE, Nicolas FJ, Hill CS. Transforming growth factor beta-independent shuttling of smad4 between the cytoplasm and nucleus. *Mol Cell Biol*. 2000;20:9041–9054. doi: 10.1128/MCB.20.23.9041-9054.2000
41. Cai R, Kwon P, Yan-Neale Y, Sambuccetti L, Fischer D, Cohen D. Mammalian histone deacetylase 1 protein is posttranslationally modified by phosphorylation. *Biochem Biophys Res Commun*. 2001;283:445–453. doi: 10.1006/bbrc.2001.4786
42. Oka T, Maillet M, Watt AJ, Schwartz RJ, Aronow BJ, Duncan SA, Molkentin JD. Cardiac-specific deletion of GATA4 reveals its requirement for hypertrophy, compensation, and myocyte viability. *Circ Res*. 2006;98:837–845. doi: 10.1161/01.RES.0000215985.18538.c4
43. Wang J, Xu N, Feng X, Hou N, Zhang J, Cheng X, Chen Y, Zhang Y, Yang X. Targeted disruption of smad4 in cardiomyocytes results in cardiac hypertrophy and heart failure. *Circ Res*. 2005;97:821–828. doi: 10.1161/01.RES.0000185833.42544.06
44. Moore JB, Zhao J, Keith MC, Amraotkar AR, Wysoczynski M, Hong KU, Bolli R. The epigenetic regulator HDAC1 modulates transcription of a core cardiogenic program in human cardiac mesenchymal stromal cells through a p53-dependent mechanism. *Stem Cells*. 2016;34:2916–2929. doi: 10.1002/stem.2471
45. Masciarelli S, Horner K, Liu C, Park SH, Hinckley M, Hockman S, Nedachi T, Jin C, Conti M, Manganiello V. Cyclic nucleotide phosphodiesterase 3a-deficient mice as a model of female infertility. *J Clin Invest*. 2004;114:196–205. doi: 10.1172/JCI21804
46. Zoccarato A, Surdo NC, Aronsen JM, Fields LA, Mancuso L, Dodoni G, Stangherlin A, Livie C, Jiang H, Sin YY, et al. Cardiac hypertrophy is inhibited by a local pool of camp regulated by phosphodiesterase 2. *Circ Res*. 2015;117:707–719. doi: 10.1161/CIRCRESAHA.114.305892
47. Taunton J, Hassig CA, Schreiber SL. A mammalian histone deacetylase related to the yeast transcriptional regulator rpd3p. *Science*. 1996;272:408–411. doi: 10.1126/science.272.5260.408
48. Moore-Morris T, Varrault A, Mangoni ME, Le Digarcher A, Negre V, Dantec C, Journot L, Nargeot J, Couette B. Identification of potential pharmacological targets by analysis of the comprehensive g protein-coupled receptor repertoire in the four cardiac chambers. *Mol Pharmacol*. 2009;75:1108–1116. doi: 10.1124/mol.108.054155
49. Di Benedetto G, Zoccarato A, Lissandron V, Terrin A, Li X, Houslay MD, Baillie GS, Zaccolo M. Protein kinase a type I and type II define distinct

intracellular signaling compartments. *Circ Res*. 2008;103:836–844. doi: 10.1161/CIRCRESAHA.108.174813
50. Hayes JS, Brunton LL, Brown JH, Reese JB, Mayer SE. Hormonally specific expression of cardiac protein kinase activity. *Proc Natl Acad Sci USA*. 1979;76:1570–1574. doi: 10.1073/pnas.76.4.1570
51. Baliga RS, Preedy MEJ, Dukinfield MS, Chu SM, Aubdool AA, Bubb KJ, Moyes AJ, Tones MA, Hobbs AJ. Phosphodiesterase 2 inhibition preferentially promotes no/guanylyl cyclase/cgmp signaling to reverse the development of heart failure. *Proc Natl Acad Sci USA*. 2018;115:E7428–E7437. doi: 10.1073/pnas.1800996115
52. Zhang Y, Feng XH, Derynck R. Smad3 and smad4 cooperate with c-jun/c-fos to mediate tgf-beta-induced transcription. *Nature*. 1998;394:909–913. doi: 10.1038/29814
53. Thambyrajah R, Fadlullah MZH, Proffitt M, Patel R, Cowley SM, Kouskoff V, Lacaud G. HDAC1 and HDAC2 modulate tgf-beta signaling during endothelial-to-hematopoietic transition. *Stem Cell Rep*. 2018;10:1369–1383. doi: 10.1016/j.stemcr.2018.03.011
54. Kim DW, Lassar AB. Smad-dependent recruitment of a histone deacetylase/sin3a complex modulates the bone morphogenetic protein-dependent transcriptional repressor activity of nkx3.2. *Mol Cell Biol*. 2003;23:8704–8717. doi: 10.1128/MCB.23.23.8704-8717.2003
55. Zhou P, Wan X, Zou Y, Chen Z, Zhong A. Transforming growth factor beta (tgf-beta) is activated by the ctbp2-p300-ap1 transcriptional complex in chronic renal failure. *Int J Biol Sci*. 2020;16:204–215. doi: 10.7150/ijbs.38841
56. Umbarkar P, Singh AP, Gupte M, Verma VK, Galindo CL, Guo Y, Zhang Q, McNamara JW, Force T, Lal H. Cardiomyocyte smad4-dependent TGF-beta signaling is essential to maintain adult heart homeostasis. *JACC Basic Transl Sci*. 2019;4:41–53. doi: 10.1016/j.jacbts.2018.10.003
57. Ding B, Abe JI, Wei H, Huang Q, Walsh RA, Molina CA, Zhao A, Sadoshima J, Blaxall BC, Berk BC, et al. Functional role of phosphodiesterase 3 in cardiomyocyte apoptosis: implication in heart failure. *Circulation*. 2005;111:2469–2476. doi: 10.1161/01.CIR.0000165128.39715.87
58. Tenbrock K, Juang YT, Leukert N, Roth J, Tsokos GC. The transcriptional repressor camp response element modulator alpha interacts with histone deacetylase 1 to repress promoter activity. *J Immunol*. 2006;177:6159–6164. doi: 10.4049/jimmunol.177.9.6159
59. Ercu M, Mucke MB, Pallien T, Marko L, Sholokh A, Schachterle C, Aydin A, Kidd A, Walter S, Esmati Y, et al. Mutant phosphodiesterase 3a protects from hypertension-induced cardiac damage. *Circulation*. 2022;146:1758–1778. doi: 10.1161/CIRCULATIONAHA.122.060210
60. Polidovitch N, Yang S, Sun H, Lakin R, Ahmad F, Gao X, Turnbull PC, Chiarello C, Perry CGR, Manganiello V, et al. Phosphodiesterase type 3a (pde3a), but not type 3b (pde3b), contributes to the adverse cardiac remodeling induced by pressure overload. *J Mol Cell Cardiol*. 2019;132:60–70. doi: 10.1016/j.yjmcc.2019.04.028
61. Oikawa M, Wu M, Lim S, Knight WE, Miller CL, Cai Y, Lu Y, Blaxall BC, Takeishi Y, Abe J-ichi, et al. Cyclic nucleotide phosphodiesterase 3a1 protects the heart against ischemia-reperfusion injury. *J Mol Cell Cardiol*. 2013;64:11–19. doi: 10.1016/j.yjmcc.2013.08.003
62. Vandeput F, Szabo-Fresnais N, Ahmad F, Kho C, Lee A, Krall J, Dunlop A, Hazel MW, Wohlschlegel JA, Hajjar RJ, et al. Selective regulation of cyclic nucleotide phosphodiesterase pde3a isoforms. *Proc Natl Acad Sci USA*. 2013;110:19778–19783. doi: 10.1073/pnas.1305427110
63. Sample V, DiPilato LM, Yang JH, Ni Q, Saucerman JJ, Zhang J. Regulation of nuclear pka revealed by spatiotemporal manipulation of cyclic AMP. *Nat Chem Biol*. 2012;8:375–382. doi: 10.1038/nchembio.799
64. Jean-Alphonse FG, Wehbi VL, Chen J, Noda M, Taboas JM, Xiao K, Vilardaga JP. Beta2-adrenergic receptor control of endosomal PTH receptor signaling via gbetagamma. *Nat Chem Biol*. 2017;13:259–261. doi: 10.1038/nchembio.2267
65. Clister T, Greenwald EC, Baillie GS, Zhang J. Akap95 organizes a nuclear microdomain to control local cAMP for regulating nuclear PKA. *Cell Chem Biol*. 2019;26:885–891.e4. doi: 10.1016/j.chembiol.2019.03.003

Curriculum Vitae

My curriculum vitae does not appear in the electronic version of my paper for reasons of data protection.

Publications

Articles

1. **Sholokh, A.,** Walter, S., Markó, L., McMurray, B., Yumi Sunaga-Franze, D., Xu, M., Zühlke, K., Russwurm, M., Bartolomaeus T.U.P., Langanki, R., Qadri, F., Heuser, A., Patzak, A., Forslund S. K., Bähring, S., Borodina, T., Persson, P. B., Maass, P. G., Bader, M., Klussmann, E. (2023). Mutant phosphodiesterase 3A protects the kidney from hypertension-induced damage. *Kidney Int*. doi:10.1016/j.kint.2023.04.026
2. Ercu, M., Mucke, M. B., Pallien, T., Marko, L., **Sholokh, A.,** Schachterle, C., Aydin, A., Kidd, A., Walter, S., Esmati, Y., McMurray, B., Lato, D. F., Yumi Sunaga-Franze, D., Dierks, P.H., Flores, B. I. M., Walker-Gray, R., Gong, M., Merticariu, C., Zühlke, K., Russwurm, M., Liu, T., Bartolomaeus T.U.P., Pautz, S., Schelenz, S., Taube, M., Napieczynska, H., Heuser, A., Eichhorst, J., Lehmann, M., Miller, D.C., Diecke, S., Qadri, F., Popova, E., Langanki, R., Movsesian, M. A., Herberg, F. W., Forslund, S. K., Müller, D. N., Borodina, T., Maass, P. G., Bähring, S., Hübner, N., Bader, M., Klussmann, E. (2022). Mutant Phosphodiesterase 3A Protects From Hypertension-Induced Cardiac Damage. *Circulation, 146*(23), 1758-1778. doi:10.1161/CIRCULATIONAHA.122.060210
3. Subramaniam, G., Schleicher, K., Kovanich, D., Zerio, A., Folkmanaite, M., Chao, Y. C., Surdo N. C., Koschinski, A., Hu, J., Scholten, A., Heck A. J. R., Ercu, M., **Sholokh, A.,** Park, K. C., Klussmann, E., Meraviglia, V., Bellin, M., Zanivan, S., Hester, S., Mohammed, S., Zaccolo, M. (2023). Integrated Proteomics Unveils Nuclear PDE3A2 as a Regulator of Cardiac Myocyte Hypertrophy. *Circ Res, 132*(7), 828-848. doi:10.1161/CIRCRESAHA.122.321448
4. **Sholokh, A.,** & Klussmann, E. (2021). Local cyclic adenosine monophosphate signalling cascades-Roles and targets in chronic kidney disease. *Acta Physiol (Oxf), 232*(1), e13641. doi:10.1111/apha.13641

Oral presentations

1. **Sholokh, A**. Mutant Phosphodiesterase 3A (PDE3A) protects from hypertension-induced kidney damage. *Student Seminar in Systems Medicine, MDC*. Online event. November, 24, 2022.
2. **Sholokh, A.,** Liu, T., Walter, S., Ercu, M., McMurray, B., Yumi Sunaga-Franze, D., Qadri, F., Zühlke, K., Langanki, R., Markó, L., Jüttner, R., Russwurm, M., Xu, M., Patzak, A., Persson, P.B., Borodina, T., Forslund S. K., Gotthardt M., Maass, P. G., Bader, M., Klussmann, E. Mutant Phosphodiesterase 3A protects from hypertension-induced end-organ damage. *Young DZHK Retreat*. Potsdam, Germany. September, 13-15, 2023.
3. **Sholokh, A.,** Walter, S., McMurray, B., Yumi Sunaga-Franze, D., Markó, L., Xu, M., Borodina, T., Forslund S. K., Maass, P. G., Bader, M., Klussmann, E. Hypertension-causing mutations of phosphodiesterase 3A possess cardio- and renoprotective effects. *7th International Meeting on Anchored cAMP signalling Pathways.* London, UK. September, 27-29, 2023.

Poster presentations

1. **Sholokh, A.,** Borodina, T., Sunaga-Franze, D. Y., Zühlke, K., Bähring, S., Bader, M., Klussmann, E. Nephroprotective effects of PDE3A gene mutations. *American Society of Nephrology (ASN) Kidney Week 2021*. Online meeting. November, 4-7, 2021.
2. **Sholokh, A.,** McMurray, B., Lato, D. F., Yumi Sunaga-Franze, D., Qadri, F., Zühlke, K., Markó, L., Xu, M., Patzak, A., Persson, P.B., Maass, P. G., Borodina, T., Bähring, S., Bader, M., Klussmann, E. Mutations of PDE3A gene are renoprotective. *European Kidney Summer School (EUKISS).* Berlin, Germany. April, 27-30, 2022.
3. **Sholokh, A.,** McMurray, B., Yumi Sunaga-Franze, D., Qadri, F., Zühlke, K., Markó, L., Xu, M., Patzak, A., Persson, P.B., Maass, P. G., Borodina, T., Bähring, S., Bader, M., Klussmann, E. PDE3A mutations protect from hypertension-induced kidney damage. *Cyclic Nucleotide Phosphodiesterases Gordon Research Conference.* Les Diablerets, VD, Switzerland. June, 19-24, 2022.

4. **Sholokh, A.,** McMurray, B., Lato, D. F., Yumi Sunaga-Franze, D., Qadri, F., Zühlke, K., Markó, L., Xu, M., Patzak, A., Persson, P.B., Maass, P. G., Borodina, T., Bähring, S., Bader, M., Klussmann, E. Elucidation of the renoprotective effects of hypertension-causing PDE3A mutations. *Europhysiology 2022.* Copenhagen, Denmark. September, 16-19, 2022.
5. **Sholokh, A.,** McMurray, B., Lato, D. F., Yumi Sunaga-Franze, D., Qadri, F., Zühlke, K., Markó, L., Xu, M., Patzak, A., Persson, P.B., Borodina, T., Maass, P. G., Bähring, S., Bader, M., Klussmann, E. A role of amphiregulin in PDE3A-mediated renoprotection. *American Society of Nephrology (ASN) Kidney Week 2022*. Orlando, FL, USA (Online participation). November, 3-6, 2022.
6. **Sholokh, A.,** Liu, T., Walter, S., Ercu, M., McMurray, B., Yumi Sunaga-Franze, D., Qadri, F., Zühlke, K., Langanki, R., Markó, L., Jüttner, R., Russwurm, M., Xu, M., Patzak, A., Persson, P.B., Borodina, T., Forslund S. K., Gotthardt M., Maass, P. G., Bader, M., Klussmann, E. Phosphodiesterase 3A mutations protect from hypertension-induced end-organ damage. *37th Annual Meeting of the International Society for Heart Research - European Section (ISHR-ES)*. Porto, Portugal. July, 10-13, 2023.
7. **Sholokh, A.,** Walter, S., Markó, L., McMurray, B., Yumi Sunaga-Franze, D., Xu, M., Zühlke, K., Langanki, R., Qadri, F., Heuser, A., Patzak, A., Forslund S. K., Borodina, T., Persson, P.B., Maass, P. G., Bader, M., Klussmann, E. Phosphodiesterase 3A mutations protect from hypertension-induced end-organ damage. *MDC/FMP PhD Retreat.* Joachimsthal, Germany. August 28-30, 2023.
8. **Sholokh, A.,** Walter, S., McMurray, B., Yumi Sunaga-Franze, D., Markó, L., Xu, M., Borodina, T., Forslund S. K., Maass, P. G., Bader, M., Klussmann, E. Hypertension-causing mutations of phosphodiesterase 3A possess cardio- and renoprotective effects. *7th International Meeting on Anchored cAMP signalling Pathways.* London, UK. September, 27-29, 2023.

Acknowledgments

First and foremost, I would like to thank my supervisor PD Dr. Enno Klussmann for giving me the opportunity to join his group at the Max Delbrück Center for Molecular Medicine in the Helmholtz Association as a PhD student. Thank you for taking time to discuss the details of my work, encouraging me to participate in many international conferences, and helping to publish the results of our research in high-ranking journals. I also appreciate the time you took to help me with reading and correcting this thesis.

I would like to thank for the opportunity to be a part of the Collaborative Research Center Nephroprotection, participate in multiple events within this graduate school, and be surrounded by talanted like-minded people. A special thank you to its spokesman Prof. Dr. Pontus B Persson for bringing us together and creating an environment for fruitful cooperation in the frame of the consortium.

I am also grateful to all my collaboration partners for their valuable contributions to the project. Dr. Philipp Maass and Brandon McMurray (SickKids Research Institute, Toronto), Dr. Tatiana Borodina and Dr. Daniele Yumi Sunaga-Franze (Genomic Technology platform, MDC), Dr. Stephan Walter (MVZ Nierenzentrum Limburg), Dr. Lajos Marko (AG For-slund, MDC), Dr. Fatimunnisa Qadri, Prof. Dr. Michael Bader (AG Bader, MDC), Minze Xu, Prof. Dr. Med. Andreas Patzak and Prof. Dr. Med. Pontus B. Persson (Charité-Universitätsmedizin Berlin), PD Dr. Med. Michael Russwurm (Ruhr-Universität Bochum), it would not be possible to achieve these results without your input.

I am also thankful to Prof. Dr. Michael Bader and Dr. Sylvia Bähring for agreeing to be my second and third supervisors, participating in my committee meetings, and bringing valuable input to the project.

I am especially grateful to all current and past members of the Klussmann lab: Thank you for sharing your experience in both scientific and personal aspects, supporting me during my time in the lab, and having plenty of nice conversations, sometimes even in German. I am happy that some of you have become close friends with me. Thank you, Maria, Sandrine, Tamara, Ryan, Kerstin, Andrea, Tiannan, Christin, Dave, Michelle.

Last but not least, I would like to thank my friend who I made in Berlin during my PhD time, old friends from Ukraine, my family, and especially my mother. Thank you for your understanding, constant support, and unlimited patience, for sharing all my achievements and failures, and for believing in me more than I did. I am happy we managed to

have many nice days, despite everything that was happening around us during these years.